



HAL
open science

Late Variscan (315 Ma) subduction or deceptive zircon REE patterns and U-Pb dates from migmatite-hosted eclogites? (Montagne Noire, France)

Pavel Pitra, Marc Poujol, Jean van den Driessche, Eloise Bretagne, Caroline Lotout, Nathan Cogné

► To cite this version:

Pavel Pitra, Marc Poujol, Jean van den Driessche, Eloise Bretagne, Caroline Lotout, et al.. Late Variscan (315 Ma) subduction or deceptive zircon REE patterns and U-Pb dates from migmatite-hosted eclogites? (Montagne Noire, France). *Journal of Metamorphic Geology*, 2022, 40 (1), pp.39-65. 10.1111/jmg.12609 . insu-03188533

HAL Id: insu-03188533

<https://insu.hal.science/insu-03188533v1>

Submitted on 14 Jun 2021

HAL is a multi-disciplinary open access archive for the deposit and dissemination of scientific research documents, whether they are published or not. The documents may come from teaching and research institutions in France or abroad, or from public or private research centers.

L'archive ouverte pluridisciplinaire **HAL**, est destinée au dépôt et à la diffusion de documents scientifiques de niveau recherche, publiés ou non, émanant des établissements d'enseignement et de recherche français ou étrangers, des laboratoires publics ou privés.

Late Variscan (315 Ma) subduction or deceptive zircon REE patterns and U-Pb dates from migmatite-hosted eclogites? (Montagne Noire, France)

Pavel Pitra^{1,2}, Marc Poujol¹, Jean Van Den Driessche¹, Eloïse Bretagne¹, Caroline Lotout^{3,4}, and Nathan Cogné¹

¹Univ Rennes, CNRS, Géosciences Rennes - UMR 6118, F-35000 Rennes, France

²Česká geologická služba, Klárov 3, CZ-118 21 Praha 1, Česká republika

³Centre de Recherches Pétrographiques et Géochimiques (CRPG), CNRS - Université de Lorraine, Vandoeuvre-lès-Nancy, F-54500, France

⁴Department of Earth Sciences, Memorial University of Newfoundland, St John's NL A1B 3X5, Canada

Corresponding author: pavel.pitra@univ-rennes1.fr

Running title: Deceptive zircon from migmatite-hosted eclogite

Abstract

Eclogites hosted in sillimanite-bearing migmatites in the Montagne Noire dome (French Massif Central) have an oceanic protolith and recorded a prograde P – T path from ~19.5 kbar, 700°C to the pressure peak at ~21 kbar, 750°C (pseudosection modelling), suggesting metamorphism in a subduction setting. Subsequent exhumation to low-pressure high-temperature (LP–HT) conditions (~6 kbar, 730°C) is constrained by the equilibration conditions of the embedding migmatite. In samples of a fresh and a retrogressed eclogite, all zircon crystals but one display similar REE patterns (no Eu anomaly, flat HREE), usually ascribed to crystallisation under eclogite-facies conditions. Yet, the U–Pb apparent ages of zircon crystals from both eclogites spread from c. 360 Ma to a dominant data cluster at c. 315 Ma. The c. 315–310 Ma zircon U–Pb dates obtained from the embedding migmatite are interpreted as the age of crystallisation of the partial melt during the LP–HT metamorphic stage. First-order geological evidence, in particular the sedimentary record, excludes the existence of a subduction zone in the region at this period. Unless calling upon a major reappraisal of the tectonics of the European Variscan orogen, this suggests an ambiguous relation between REE patterns and U–Pb dates in the zircon population. Various scenarios that could account for the observations are discussed. Combining our data with the results of a previously published Sm–Nd dating of garnet, and regional considerations, we consider that 360 Ma is the best approximation of the minimum age of the eclogite-facies event. We hypothesise that the eclogites formed farther north and were transferred to their present location by lower-crustal flow. It is inferred that during the subsequent exhumation, eclogite-facies zircon grains recrystallised and underwent partial to total resetting of their U–Pb system, whereas the REE system remained mostly unmodified. These results caution against the use of REE patterns as the only criterion to associate a specific zircon age with HP metamorphism in eclogites occurring in migmatitic domes.

Keywords: eclogite; migmatite; LA-ICP-MS; zircon and monazite U–Th–Pb geochronology; uncoupled U–Pb and REE behaviour; Variscan French Massif Central

1 INTRODUCTION

Eclogites at the Earth surface mostly testify to past subduction zones and collision orogenesis. Understanding their formation and exhumation is therefore a major challenge when reconstructing geodynamics through time. This involves retrieving accurate pressure (P) and temperature (T) data, including the attained peak pressure, but also the absolute ages of the various segments of the metamorphic evolution (or P – T path). U-Pb dating of zircon is a powerful tool to retrace the timing of burial and exhumation of these rocks in a subduction wedge (e.g. Rubatto, 2002; Rubatto & Hermann, 2007). The main difficulty is to associate a given zircon domain or age with a particular portion of the P – T path (e.g. Rubatto, 2017; Kohn & Kelly, 2018). Zircon can crystallise along the prograde part of the P – T path (e.g. Beckman et al., 2014; Lotout, Pitra, Pujol, Anczkiewicz, & Van Den Driessche, 2018), or at the pressure peak (e.g. Katayama, Maruyama, Parkinson, Terada, & Sano, 2001), but also possibly during decompression, at the temperature peak, or during cooling (Kohn, Corrie, & Markley, 2015; Kohn & Kelly, 2018). Among other approaches, the rare-earth-element (REE) content of zircon is widely used to distinguish zircon that crystallised under eclogite-facies conditions. Due to the abundance of garnet (that fractionates heavy REE – HREE) and lack of plagioclase (that fractionates Eu^{2+}), typical for eclogite-facies assemblages of metabasic rocks, eclogitic zircon typically displays a weak or no negative Eu anomaly, and a flat chondrite-normalised HREE pattern (Rubatto, 2002; Whitehouse & Platt, 2003). However, the use of this criterion is not straightforward (see discussion in Kohn, 2016; Rubatto, 2017). Furthermore, decoupling of the U-Pb and REE systems in zircon has been documented under high-temperature conditions (e.g. Kusiak et al., 2013; Whitehouse, Ravindra Kumar, & Rimša, 2014; Štípská, Powell, Hacker, Holder, & Kylander-Clark, 2016; Kunz, Regis, & Engi, 2018). Schmädicke, Will, Ling, Li, and Li (2018) have documented that only rare zircon from fresh eclogites from the Erzgebirge (Variscan Bohemian Massif) recorded peak-pressure conditions, whereas most data reflected post-peak reequilibration (despite the well-preserved eclogite-facies mineral assemblage, and ‘eclogitic’ REE spectra in zircon). Consequently, this approach can result in conflicting interpretation of the age of the HP metamorphism, and hence of the inferred geodynamics.

As an example, based on the study of an eclogite embedded in migmatitic rocks from the Montagne Noire (southern French Massif Central, European Variscan belt) two conflicting interpretations were proposed. Faure et al. (2014) and Whitney, Roger, Teyssier, Rey, and Respaut (2015) have obtained very similar dates of c. 360 Ma and c. 315 Ma. Faure et al. (2014) consider that the 360 Ma date represents the age of the HP metamorphism, as recognised in other parts of the European Variscan belt (e.g. Bosse et al., 2000; Kroner & Romer, 2013; Lotout, Pujol, Pitra, Anczkiewicz, & Van Den Driessche, 2020; Paquette, Ballèvre, Peucat, & Cornen, 2017), whereas they attribute the 315 Ma date to the low-pressure high-temperature (LP–HT) event characteristic of the late evolution of the belt between 320–290 Ma (e.g. Gardien, Lardeaux, Ledru, Allemand, & Guillot, 1997; Kalt, Corfu, & Wijbrans, 2000; Pujol et al., 2017; Roger et al., 2015). In contrast, Whitney et al. (2015) claim that the 315 Ma date is the age of “the youngest Variscan eclogite”, the 360 Ma date being the age of a “pre-eclogite facies metamorphism”. The interpretation of Faure et al. (2014) is based on Sm-Nd dating of eclogitic garnet and regional, mainly tectonic, considerations, whereas Whitney et al. (2015) argue that the REE patterns of the zircon grains dated at 315 Ma (absence of Eu anomaly and flat HREE) are characteristic of the eclogite facies. Although conflicting, both interpretations seem founded, calling for a better understanding of the behaviour of zircon in eclogites. We approach this issue by re-investigating the same fresh eclogite previously dated in these two studies, together with a retrogressed eclogite, and the enclosing migmatite, following a petrological approach based on thermodynamic modelling of phase equilibria, and a geochronological and geochemical investigation of zircon and its relations with other metamorphic minerals. While both

previous interpretations relate the HP metamorphism to crustal thickening, our data point to a subduction context, not previously recognized in this part of the Variscan belt. From the discrepancy between the sedimentary and magmatic record on the one hand, and the metamorphic and geochronological data on the other hand, we aim to exemplify the problems related to attributing zircon ages to specific stages of a given metamorphic evolution, to discuss the strategies of identifying the most plausible scenarios and to highlight the first-order importance of regional geological constraints.

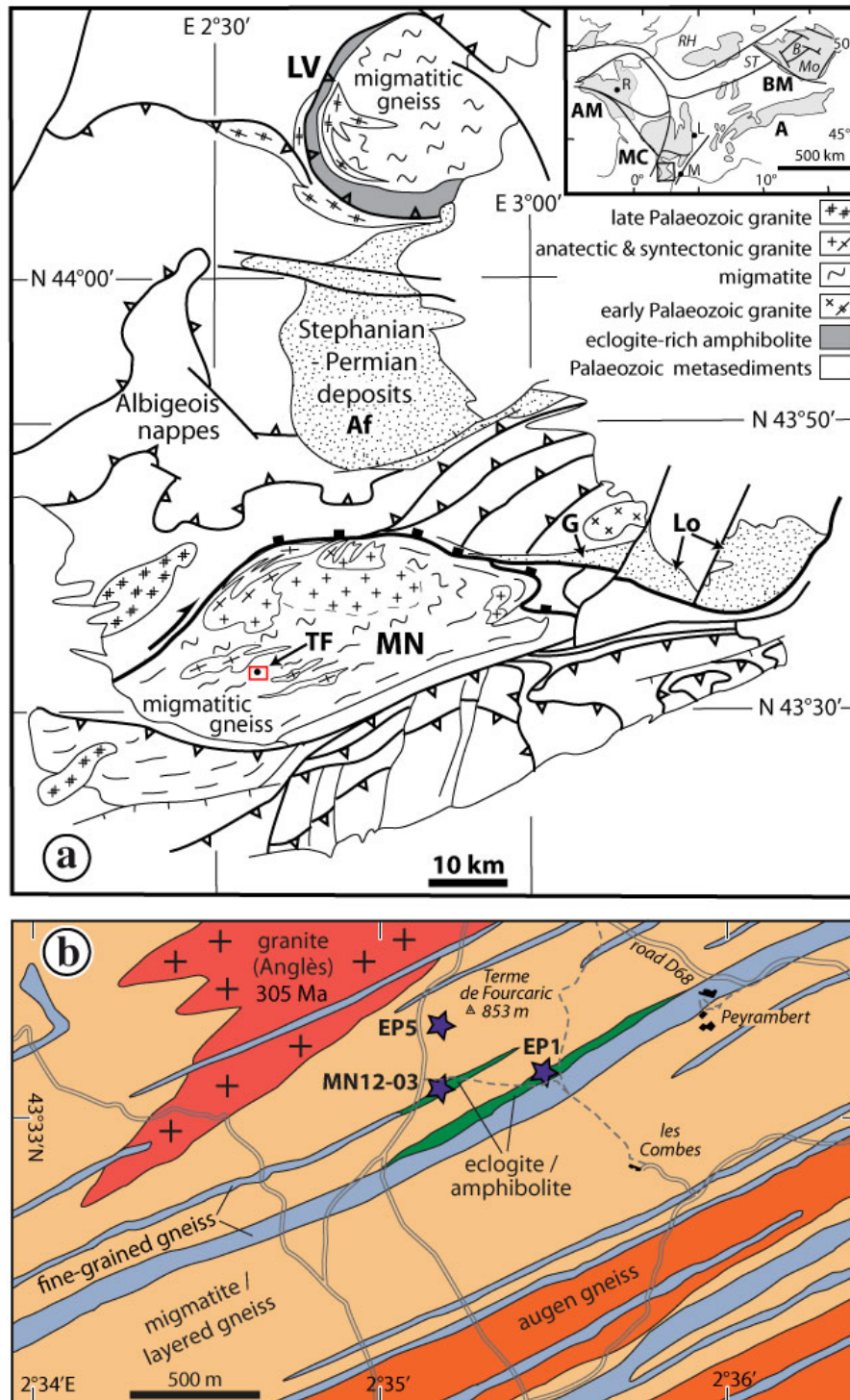


Figure 1. (a) Structural map of the southern French Massif Central showing the relationships between the Montagne Noire gneiss dome (MN), the Lévézou complex (LV), the Stephanian-Permian basins, and the Variscan thrusts and nappes (modified after Brun & Van Den Driessche, 1994). Af: Saint-Affrique basin, G: Graissessac basin, Lo: Lodève basin, TF: location of the Terme de Fourcaric area. Insert shows the location of the study area within the European Variscan belt (modified from Pitra, Ballèvre, & Ruffet, 2010). A - Alps, AM - Armorican Massif, BM - Bohemian Massif, MC - Massif Central. B - Teplá-Barrandian, Mo - Moldanubian, ST - Saxothuringian, RH - Rhenohercynian. L: Lyon; M: Montpellier; R: Rennes. (b) Geological map of the studied area (modified after Demange, Guérangé-Lozes, & Guérangé, 1996) with location of the sampled localities (blue stars). EP1 – ‘fresh’ eclogite (N 43°33'5.21", E 2°35'27.88"), EP5 – sillimanite-bearing migmatite (N 43°33'20.04", E 2°35'1.95"); MN12-03 – ‘retrogressed’ eclogite (N 43°33'5.20", E 2°35'5.90"). Sample EP4 comes from the same location as EP1. Given the poor outcrop conditions all samples were collected from large (0.5–1 m) boulders.

2 GEOLOGICAL SETTING

The Montagne Noire, located in the southern part of the Variscan French Massif Central (Figure 1), is a gneiss-migmatite dome where rare eclogites occur as boudins in sillimanite-bearing migmatites (Demange, 1985). It is composed of a high-grade gneissic core surrounded by mostly low-grade metasediments. The gneissic core is composed of migmatites and augen orthogneisses, with some fine-grained gneissic intercalations that have been interpreted as either metasediments or mylonitic zones (Bogdanoff, Donnot, & Ellenberger, 1984). Some of these intercalations contain HP–HT mafic and ultramafic metamorphic rocks, suggesting the presence of possible major early tectonic contacts (Van Den Driessche & Brun, 1992). The migmatites, commonly sillimanite- and/or cordierite-bearing, resulted mostly from the partial melting of sediments, but also felsic augen orthogneisses during a low-pressure high-temperature (LP–HT) metamorphic event. Weakly deformed to undeformed anatectic granites intrude both the orthogneisses and the migmatites. This LP–HT event and associated plutonism occurred between c. 320 and 290 Ma (Poilvet, Poujol, Pitra, Van Den Driessche, & Paquette, 2011; Poujol et al., 2017; Roger et al., 2015; 2020; Trap, Roger, Cenko-Tok, & Paquette, 2017). The gneissic core is surrounded by weakly metamorphosed or unmetamorphosed lower to middle Palaeozoic sediments that are intensely deformed by southward verging folds and thrust faults. Late Carboniferous to Early Permian detrital sediments unconformably overlie these tectonic units to the South. In contrast, to the North, the E-W-trending north-dipping normal fault zone (Espinouse detachment) marks the tectonic contact between these sediments and the dome units, and controls the development of the Lodève-Graissessac and Saint-Affrique basins (Figure 1; Van Den Driessche & Brun, 1992; Burg, Van Den Driessche, & Brun, 1994). The latter separates the Montagne Noire from the eclogite-rich Lévézou massif (e.g. Nicollet, 1978; Lotout et al., 2020; Figure 1).

As previously mentioned, the age of the eclogite-facies metamorphism is disputed. Faure et al. (2014) propose an age of c. 360 Ma based on Sm-Nd dating of garnet and regional considerations, whereas Whitney et al. (2015) argue that the eclogites formed at c. 315 Ma, using the ‘eclogitic’ REE patterns of the dated (U-Pb) zircon crystals as the main argument. For the purpose of this study, several eclogites and one migmatite were sampled at the Terme de Fourcaric (Figure 1b), the locality where both Faure et al. (2014) and Whitney et al. (2015) collected their samples.

3 METHODOLOGY

We implemented a petrological approach based on thermodynamic modelling of phase equilibria, and a geochronological and geochemical investigation of zircon grains from the different samples, and their relation with other metamorphic minerals.

3.1 Mineral compositions

Mineral compositions were measured using a Cameca SX-100 electron microprobe (Microsonde Ouest, IFREMER, Plouzané, France) operating in a wavelength-dispersive mode. Operating conditions were 15 kV acceleration voltage, 20 nA beam current, 10 s counting time on the peak and a focused beam diameter of 1 µm. For a complete description of the analytical procedure and the list of the standards used, see Pitra, Boulvais, Antonoff, and Diot (2008).

Compositional variables (mole/atomic proportions) and other symbols used are: $X_{Mg} = Mg/(Fe^{2+}+Mg)$ (garnet, clinopyroxene, amphibole), Grs = grossular = $100 \times Ca/(Ca+Mn+Fe^{2+}+Mg)$, Prp = pyrope = $100 \times Mg/(Ca+Mn+Fe^{2+}+Mg)$, Alm = almandine = $100 \times Fe^{2+}/(Ca+Mn+Fe^{2+}+Mg)$, Sps = spessartine = $100 \times Mn/(Ca+Mn+Fe^{2+}+Mg)$ (garnet), Jd = jadeite = $100 \times Na/(Na+Ca)$ (clinopyroxene), An = anorthite = $100 \times Ca/(Ca+Na+K)$ (plagioclase), weight per cent (wt%), volume per cent (vol.%), mole per cent (mol.%), pfu =

per formula unit. The symbol ‘→’ is used to describe the compositional change from core to rim.

3.2 Whole-rock chemical composition

Large samples (5 to 10 kg) were cleaned from any weathered material, then crushed in a jaw crusher and in an agate mortar, following a standard protocol at Géosciences Rennes (Université Rennes 1), in order to obtain a fine powder. Major and trace elements have been analysed by Inductively Coupled Plasma Optical Emission Spectrometry (ICP-OES) and Inductively Coupled Plasma Mass Spectrometry (ICP-MS), respectively, at the Service d'Analyse des Roches et Minéraux (SARM, CRPG-CNRS, Nancy, France), following the procedure described in Carignan, Hild, Mevelle, Morel, & Yeghicheyan (2001). FeO (vs. Fe₂O₃) was analysed by wet titration in the eclogites. The results are reported in Table S5.

3.3 Thermodynamic modelling

Pressure-temperature pseudosections (isochemical phase diagrams) and isopleths for some key chemical variables have been calculated in the model systems NCFMASHTO and MnNCKFMASHTO (MnO–Na₂O–CaO–K₂O–FeO–MgO–Al₂O₃–SiO₂–H₂O–TiO₂–Fe₂O₃) for the eclogites and the migmatite, respectively, using both Theriak/Domino (de Capitani & Petrakakis, 2010) and THERMOCALC (Powell & Holland, 1988; Powell, Holland, & Worley, 1998), and, in both cases, the internally consistent thermodynamic data set 5.5 (Holland & Powell 1998; updated Nov. 2003). Both programmes yield identical results (cf. Manzotti et al., 2018), but some field boundaries are easier to calculate precisely with THERMOCALC. Mixing models for solid solutions were taken from Diener and Powell (2012) – amphibole (am), clinopyroxene (cpx), White, Powell, and Holland (2007) – garnet (g), biotite (bi), granitic melt (liq), Coggon and Holland (2002) – muscovite (mu), Holland, Baker, and Powell (1998) – chlorite (chl), Holland and Powell (2003) – plagioclase (pl), Holland and Powell (1998) – talc (ta), epidote (ep), White, Powell, and Clarke (2002) – magnetite (mt), and White, Powell, Holland, & Worley (2000) – haematite (hem), ilmenite (ilm). Albite (ab), lawsonite (law), quartz (q), rutile (ru) and titanite (sphene, sph) are considered as pure end members. The conversion of the mixing models for Theriak/Domino was obtained from Doug Tinkham (<http://dtinkham.net/peq.html>). Pure aqueous fluid (H₂O) is considered in excess for the eclogites because of the dehydration character of most of the subsolidus reactions that lead invariably to H₂O saturation along the prograde evolution. For the migmatite, the amount of H₂O is set so that the system is just H₂O-saturated immediately below the solidus. The measured amount of FeO (vs. Fe₂O₃) was used in the eclogites. In the migmatite (EP5), the proportion of Fe³⁺ (out of total Fe) was set to an arbitrary low value (3%). The bulk rock compositions used to calculate the *P–T* diagrams were corrected for the presence of apatite, not considered in the calculations.

3.4 U-Th-Pb geochronology and trace-element analysis

A mineral separation procedure has been applied to concentrate zircon crystals using the facilities available at Géosciences Rennes (for details see Ballouard et al., 2015). Zircon crystals were then handpicked under a binocular microscope and embedded in epoxy mounts, which were polished down to expose the centre of the grains. Zircon and monazite were also localised in thin sections using the back-scattered electrons (BSE) mode on a Scanning Electron Microscope (CMEBA platform, Université Rennes 1). Zircon grains were imaged by cathodoluminescence (CL) using a Reliotron CL system equipped with a digital colour camera (GeOHeLiS platform, Université Rennes 1) or using a cathodoluminescence detector attached to a Scanning Electron Microscope (Magma et Volcans laboratory, Université Clermont-Ferrand, France). Monazite crystals in thin section were imaged using BSE (CMEBA platform, Université Rennes 1).

U-Th-Pb geochronology of zircon and monazite was conducted by in-situ laser ablation inductively coupled plasma mass spectrometry (LA-ICP-MS) at Géosciences Rennes (GeOHeLiS platform) using a ESI NWR193UC Excimer laser coupled to an Agilent quadrupole 7700x ICP-MS equipped with a dual pumping system to enhance sensitivity. Ablation spot diameters of 25–30 μm (zircon) and 10 μm (monazite) with a repetition rate of 3 Hz and a fluence of 8 J/cm^2 (zircon) and 6.7 J/cm^2 (monazite) were used. The instrumental conditions are reported in Table S1. Further information can be found in Ballouard et al. (2015). Data reduction was carried out with the Iolite (Paton, Hellstrom, Paul, Woodhead, & Hergt, 2011) data-reduction scheme U-Pb Geochronology (Paton et al., 2010). For the individual analyses (reported in Tables S6, S8, S10 and S11), the reproducibility of the quality control reference materials has been propagated by quadratic addition as recommended by Horstwood et al. (2016) following the equation proposed in Horstwood, Foster, Parrish, Noble, and Nowell (2003). In the Rennes laboratory, the long-term variance for the validation material is 1.9 %, but it was not propagated to the errors displayed for the dates reported in Figures 7, 8, 9 and S5. However, when these dates are discussed in the text, the error taking into account the long-term variance is also reported in italics between brackets. Concordia diagrams and age calculations were generated using IsoplotR (Vermeesch, 2018). All errors given in the tables and in the figures are listed at two sigma. When Concordia ages have been calculated using Ludwig's algorithm (Ludwig, 1998), the reported MSWD values are for concordance and equivalence.

Trace-element analyses of zircon were performed in-situ on crystals mounted in epoxy pucks and in-context on crystals recognised in thin sections by LA-ICP-MS in the Magma et Volcans laboratory (Université Clermont-Ferrand, France) using a Resonetics/M-50E 193 nm Excimer laser coupled to an Agilent 7500cs quadrupole ICP-MS. Ablation spot diameter was 27 μm , repetition rate of 3 Hz and fluence of 4 J/cm^2 . REE were measured for each dated zircon zone, when possible. Titanium concentration in zircon has been measured together with the REE using ^{49}Ti . Trace-element analyses of omphacite and amphibole in sample EP1 were conducted in-context in thin section by LA-ICP-MS also in the Magma et Volcans laboratory. Ablation spot diameter was 47 μm , repetition rate of 5 Hz and fluence of 6 J/cm^2 . Trace-element analyses of other rock-forming minerals (garnet, amphibole, plagioclase) were conducted in-context in thin sections by LA-ICP-MS at Géosciences Rennes (GeOHeLiS platform) using a ESI NWR193UC Excimer laser coupled to an Agilent quadrupole 7700x ICP-MS. Ablation spot diameters of 50 μm (garnet) and 25 μm (amphibole, pyroxene, plagioclase) with a repetition rate of 5 Hz and a fluence of 6 J/cm^2 were used. The instrument operating conditions are reported in Tables S2 and S3.

Although U-Pb geochronology and trace-element analyses were performed on non-identical spots, care was taken, whenever possible, to place the analytical spots in identical zircon domains, based on CL zoning, to infer correspondence between U-Pb dates and the trace-element content.

4 PETROLOGY

Sample EP1 is a relatively fresh eclogite comprising garnet (~40 vol.%), omphacite (~25 vol.%), pargasitic amphibole (~5 vol.%), rutile, and rare kyanite and quartz, interpreted as characteristic of the 'primary' eclogite-facies assemblage (Figures 2 and S1). Clinopyroxene defines a faint foliation. The primary minerals are surrounded by a very fine-grained (1–3 μm) symplectite, the mode of which varies even at the scale of a thin section (~10–30 vol.%). The symplectitic intergrowths are generally composed of plagioclase and amphibole, but locally contain various proportions of diopside, orthopyroxene and spinel. Garnet (1–5 mm) is subhedral and includes rutile, amphibole and rare quartz. It shows a core-to-rim increase of pyrope (32→52 mol.%; $X_{\text{Mg}} = 0.43\rightarrow 0.60$) and decrease in spessartine (2→0 mol.%) and grossular (23→13 mol.%) (Figure 2; Table S4). A reversal of this trend is

observed in the outermost rim ($\sim 100 \mu\text{m}$), where garnet reaches the composition of $\text{Alm}_{39}\text{Prp}_{47}\text{Grs}_{14}\text{Sps}_1$ ($X_{\text{Mg}} = 0.55$). Unzoned anhedral omphacite (up to 8 mm) contains 35–41 mol.% jadeite ($X_{\text{Mg}} = 0.86\text{--}0.90$). Pargasitic amphibole ($\text{Si} = 5.82\text{--}6.65$ pfu, $\text{Na}(\text{A}) = 0.52\text{--}0.82$ pfu, $X_{\text{Mg}} = 0.79\text{--}0.92$) occurs in two textural settings: (i) relatively large crystals (up to 3 mm) commonly associated with garnet and, (ii) fine-grained symplectitic intergrowth with plagioclase, typically surrounding omphacite relics. There is no systematic chemical difference between the two occurrences. The composition of plagioclase in the symplectites is strongly variable ($\text{An}_{08}\text{--An}_{61}$) with no clear relation to the exact textural position. Kyanite was only found in the heavy-mineral separate. In thin sections, kyanite is replaced by an extremely fine-grained ($< 1 \mu\text{m}$) spinel-plagioclase symplectite, commonly included in garnet (Figure S1c,h; cf. e.g. Liati & Seidel, 1996). Mg-rich ilmenite (geikielite up to 35 mol.%) commonly surrounds or replaces rutile. Zircon (up to $320 \mu\text{m}$, but mostly $< 50 \mu\text{m}$) is commonly found as inclusions in garnet rims, but occurs also in omphacite, and in the symplectites. Zircon in symplectites is always significantly larger than the size of the symplectitic lamellae (Figure S2).

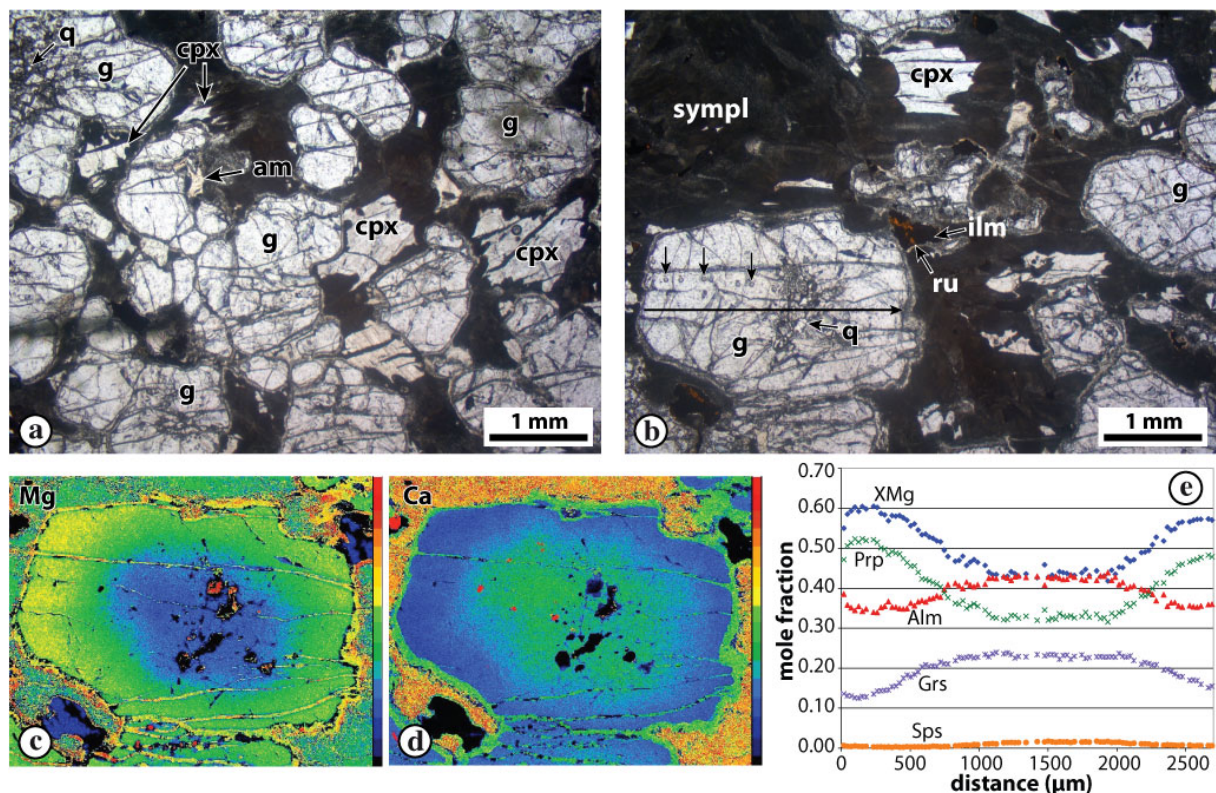


Figure 2. Eclogite EP1 – photomicrographs (plane polarized light; a, b), X-ray maps for Mg (c) and Ca (d) and a chemical profile of garnet (e; located in b – long arrow). Unlabelled arrows in (b) indicate the location of some of the LA-ICP-MS analytical spots.

Sample EP4 is a retrogressed eclogite, collected in the same location as EP1. It was not studied in detail either from a petrological or a geochronological point of view, but the available whole-rock chemical composition is used in section 5. The sample comprises anhedral garnet and amphibole in a symplectite-dominated matrix. Anhedral garnet (up to 5 mm in diameter) has an inclusion-free rim and a core rich in inclusions of rutile, ilmenite and locally epidote. It is surrounded by a shell (up to 1 mm thick) of relatively coarse-grained symplectite of plagioclase, orthopyroxene and amphibole. Fine-grained symplectite of plagioclase, amphibole and locally diopside represents the major part of the matrix. No relics of omphacite were found. Accessories comprise rutile, ilmenite, titanite, apatite and zircon.

Sample MN12-03 is a strongly retrogressed eclogite that contains garnet (~30 vol.%), hornblende (~20 vol.%), biotite (~10 vol.%), and a relatively coarse-grained plagioclase-amphibole symplectite (Figure 3). Accessory minerals include quartz, rutile, ilmenite, titanite, apatite, zircon and, interestingly, monazite. Anhedral rounded garnet (up to 4 mm) includes rutile, quartz and pargasitic amphibole (Si = 6.10–6.20 pfu, Na(A) = 0.61–0.63 pfu, X_{Mg} = 0.78). It has a large unzoned core (pyrope 36–38 mol.%, grossular 12 mol.%, spessartine 4 mol.%, X_{Mg} = 0.45–0.47; Figure 3b; Table S4) and a chemically zoned rim (~150 μ m) marked by a rimward increase of spessartine (up to 8 mol.%) and a decrease in pyrope (36→20 mol.%; X_{Mg} = 0.45→0.26), interpreted in terms of diffusion zoning due to partial resorption of the garnet rim. Matrix amphibole is magnesiohornblende. Relatively large crystals (up to 1 mm) are less silica-rich and more sodic and magnesian (Si = 6.74–6.94 pfu, Na(A) = 0.33–0.40 pfu, X_{Mg} = 0.72–0.74), than amphibole in symplectites (Si = 7.25–7.41 pfu, Na(A) = 0.07–0.08 pfu, X_{Mg} = 0.68–0.72). The latter is locally intergrown with lamellae of cummingtonite (X_{Mg} = 0.60). Plagioclase composition ranges An₃₄–An₈₂, and the cores of the crystals are systematically less anorthitic than the rims. Biotite is commonly partly rimming garnet and is relatively rich in titanium (Ti = 0.18–0.23 pfu, Al = 1.33–1.39 pfu, X_{Mg} = 0.61–0.64). Zircon is present both as inclusions in garnet and in the matrix symplectites. Monazite occurs mostly in amphibole-dominated symplectites, and locally in plagioclase-rich rims around garnet. It was never found included in garnet.

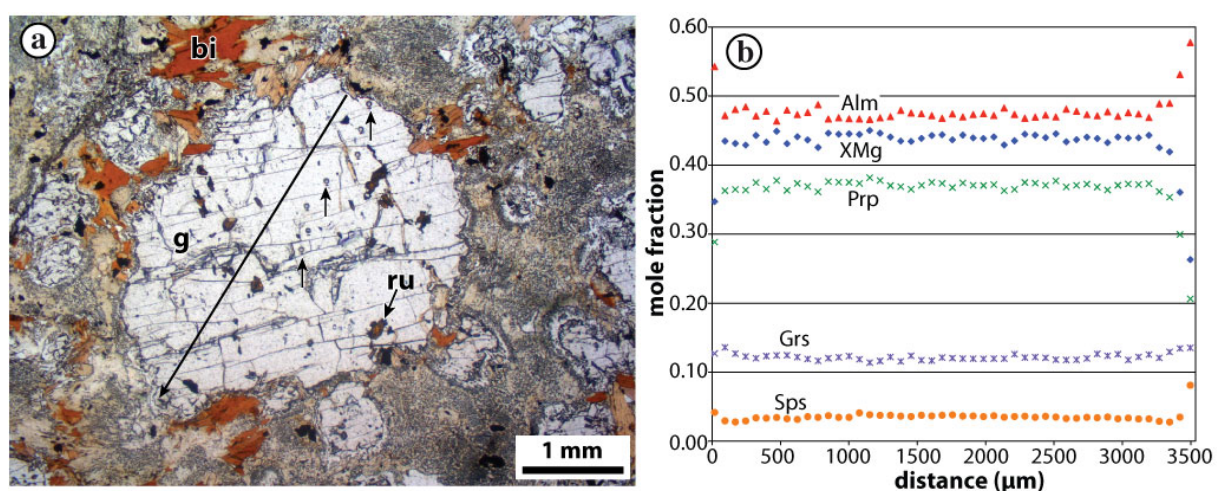


Figure 3. Retrogressed eclogite MN12-03 – photomicrograph (plane polarized light; a) and a chemical profile of garnet (located by the long arrow in a). Unlabelled arrows in (a) indicate the location of some of the LA-ICP-MS analytical spots.

Sample EP5 is a biotite + garnet + sillimanite-bearing felsic migmatite (Figure 4). It has a planar foliation marked by the orientation of biotite (X_{Mg} = 0.30–0.33, Ti = 0.14–0.23 pfu; Table S4), parallel to the alternation of relatively biotite-rich layers and coarser-grained layers rich in quartz, plagioclase and K-feldspar (Ab₁₄–Ab₁₆). The anorthite content in plagioclase decreases rimwards (An₁₉→An₁₂). Fibrolitic sillimanite occurs in cm-sized nodules with quartz. Minor anhedral muscovite is locally present. Subhedral garnet (up to 1 mm) has an unzoned core (pyrope 9 mol.%, grossular 2 mol.%, spessartine 10 mol.%, X_{Mg} = 0.11) and a large zoned rim (Figure 4) characterised by a progressive rimward increase in spessartine (up to 21 mol.%) and decrease in pyrope (5 mol.%) and X_{Mg} (0.07). Accessory minerals include ilmenite, apatite and zircon.

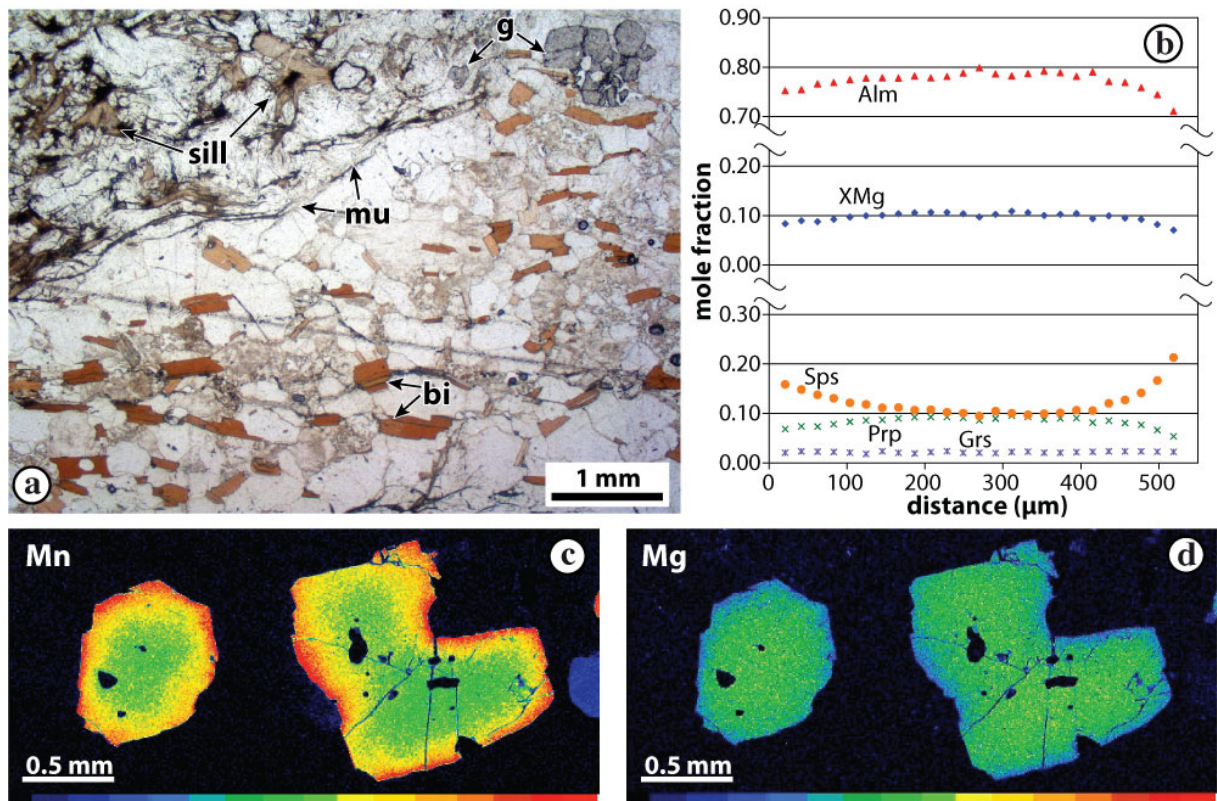


Figure 4. Migmatite EP5 – a) photomicrograph (plane polarized light); b) chemical profile and X-ray maps for Mn (c) and Mg (d) of garnet.

In summary, we interpret that the eclogite EP1 equilibrated with an assemblage comprising garnet, omphacite, pargasitic amphibole, kyanite and rutile, characteristic of the eclogite facies. Quartz, preserved as inclusions in garnet and locally in the matrix, was also present during most of the metamorphic evolution. The local and heterogeneous symplectitic development of secondary assemblages comprising amphibole, plagioclase, diopsidic clinopyroxene, orthopyroxene, spinel and ilmenite testifies to decompression at relatively high temperatures. The wide range of plagioclase composition points to the preservation of chemical potential gradients and hence incomplete equilibration. Garnet zoning, with the rimward decrease of spessartine and increase of pyrope, is characteristic of a prograde growth zoning (e.g. Tracy, 1982) and can be used to quantify the prograde P - T evolution. Eclogite MN12-03 is strongly retrogressed and displays a mostly coarsely symplectitic secondary assemblage dominated by magnesiohornblende and plagioclase. Biotite is interpreted to be part of this assemblage, and possibly related to interaction of the eclogite with externally derived fluids. This is compatible with the unusual presence of monazite and the coarser-grained character of the symplectites. Abundant garnet is interpreted as the only clear relic of the eclogite facies, but lacks growth zoning, which can be attributed to re-equilibration at some later stage of the metamorphic evolution. Migmatite EP5 is interpreted to have developed the assemblage quartz, plagioclase, K-feldspar, biotite, sillimanite, garnet, ilmenite during the cooling and crystallisation of partial melt. Qualitatively, this points to conditions of high temperature and relatively low pressure. Garnet zoning, which suggests diffusional re-equilibration associated with partial resorption of garnet, as well as the local presence of muscovite are compatible with late-stage evolution dominated by cooling.

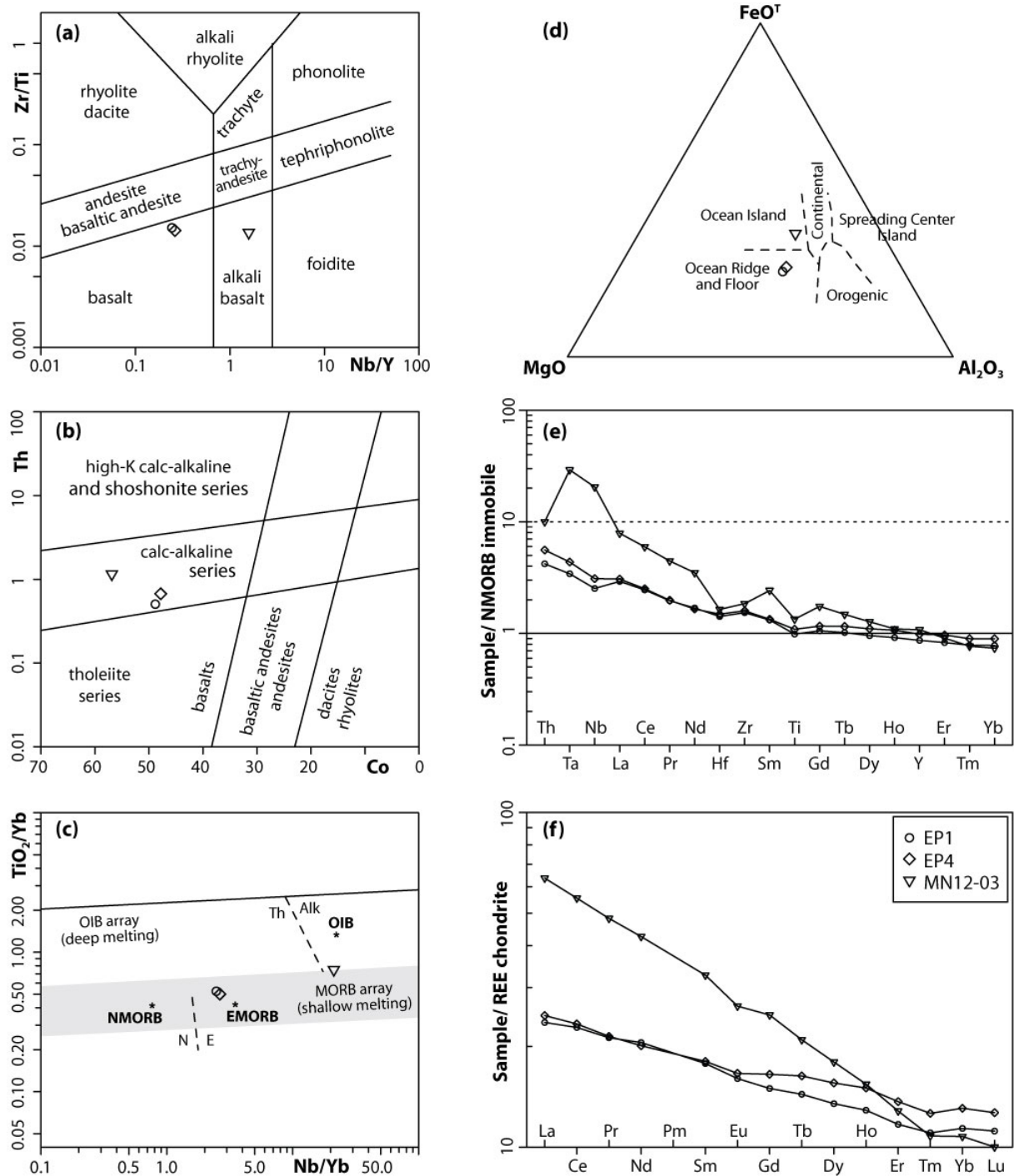


Figure 5. Geochemical classification diagrams – (a) Nb/Y-Zr/Ti plot (Pearce, 1996), (b) Co-Th plot (Hastie et al., 2007), (c) Nb/Yb-TiO₂/Yb (Pearce, 2008) plot and (d) Al₂O₃-FeO-MgO plot (Pearce et al., 1977), and spider plots – (e) for immobile elements normalised to NMORB (Sun & McDonough, 1989 in Pearce, 2014) and (f) for REEs normalised to chondrite (Boynton, 1984).

5 WHOLE-ROCK GEOCHEMISTRY

Three eclogite samples have been analysed for major and trace elements (Table S5). They have the composition of basalt (EP1 and EP4) and alkali basalt (MN12-03), using the robust, immobile elements-based Nb/Y vs. Zr/Ti diagram (Pearce, 1996), appropriate for metamorphosed and/or hydrothermally altered rocks (e.g. Janoušek et al., 2014; Pearce, 2014) (Figure 5a). They are calc-alkaline in character (Figure 5b). Based on both major and reputedly immobile trace elements, all samples reveal an oceanic origin, of E-MORB (EP1 and EP4) or OIB (MN12-03) type (Figure 5c,d; Pearce, Gorman, & Birkett, 1977; Pearce,

2008). The samples are slightly to moderately enriched in incompatible elements, which also points to the E-MORB (EP1 and EP4) or OIB (MN12-03) type (Figure 5e; Pearce, 2008, 2014). The total REE contents are rather low ($\Sigma\text{REE} = 60.7\text{--}124.2$ ppm). The chondrite-normalised (Boynnton, 1984) REE patterns (Figure 5d) show a moderate enrichment in LREE and negligible Eu anomalies ($\text{Eu}/\text{Eu}^* = 0.93\text{--}0.98$). The retrogressed eclogite sample MN12-03 is significantly more enriched in LREE ($\text{La}_N/\text{Lu}_N = 6.56$) than the other two eclogites ($\text{La}_N/\text{Lu}_N = 2.01\text{--}2.18$). This may be related to the unusual presence of monazite and tentatively attributed to possible interaction of the eclogite with fluids derived from the adjacent melt-bearing felsic gneiss.

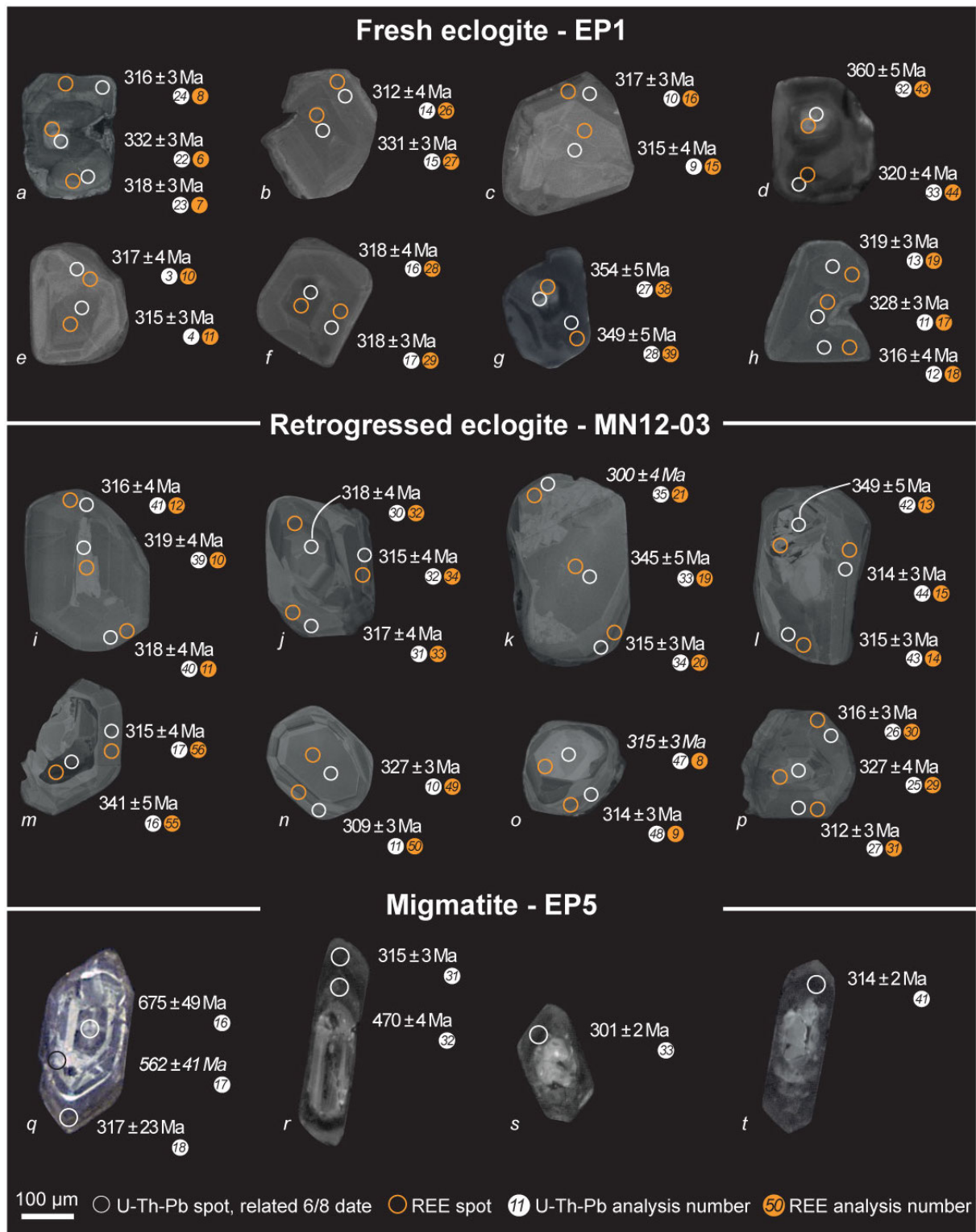


Figure 6. Representative cathodoluminescence images of zircon grains from the fresh eclogite EP1 (a-h) the retrogressed eclogite MN12-03 (i-p) and the migmatite EP5 (q-t). The locations of laser spots (white and orange circles for U-Pb and REE analyses, respectively) are indicated along with the spot number (Tables S6 and S7). The corresponding $^{206}\text{Pb}/^{238}\text{U}$ dates are quoted with $\pm 2\sigma$ uncertainty. All displayed analyses are concordant at $>95\%$ (except those in italic).

6 U-Th-Pb ZIRCON AND MONAZITE DATING

6.1 Fresh eclogite EP1

Zircon grains were analysed as separated minerals mounted in epoxy pucks (46 analyses on 20 crystals). Additionally, analyses were performed on zircon *in-context* directly in thin section of the fresh eclogite. Although zircon is common in this sample (included in garnet, omphacite and in symplectite, see above), most crystals found in the thin section were too small, and only 10 analyses have been done on 8 crystals (Figure S2). Zircon grains are colourless and translucent with a sub-rounded to irregular shape. The size of the dated crystals ranges between 30 and 320 μm . Cathodoluminescence (CL) imaging revealed distinct inner and outer domains (Figure 6a-h). The textures of both inner and outer domains are similar. The most common texture is fir-tree zoning as well as sector zoning, observable in both domains. Some crystals show irregular concentric zoning or diffuse oscillatory zoning (Figure 6a-c,e,f,h), whereas others lack any clear zoning or only display diffuse darker patches. In several crystals, the interface between the inner and outer domains crosscuts the internal zoning, which could suggest recrystallisation or partial resorption prior to the growth of the outer part (Figure 6c,g,h).

Among the fifty-six analyses performed on the 28 zircon crystals from the fresh eclogite EP1, fifty-two analyses plot in a concordant position with $^{206}\text{Pb}/^{238}\text{U}$ apparent ages that spread between 366 ± 5 and 306 ± 5 Ma (Figure 7a; Table S6). A coherent group of 33 concordant analyses yields a weighted average $^{206}\text{Pb}/^{238}\text{U}$ date of 315.5 ± 1.3 (± 6.1) Ma (MSWD = 0.84; Figure 9b).

With respect to zoned crystals, several different situations were encountered. A core dated at c. 360 Ma surrounded by a c. 320 Ma rim was found in a grain from the epoxy puck (Figure 8d). A small zircon crystal located in a fine-grained symplectitic intergrowth replacing omphacite was dated *in-context* in the thin section at 366 ± 5 Ma (Figure S2a). Other zircon grains have c. 330 Ma cores and c. 315 Ma rims (Figure 6a,b,h) or are homogeneous in terms of age at c. 350 Ma (Figure 6g). However, most zircon crystals yield dates of c. 315 Ma, in both the inner and the outer domains (Figure 6c,e,f).

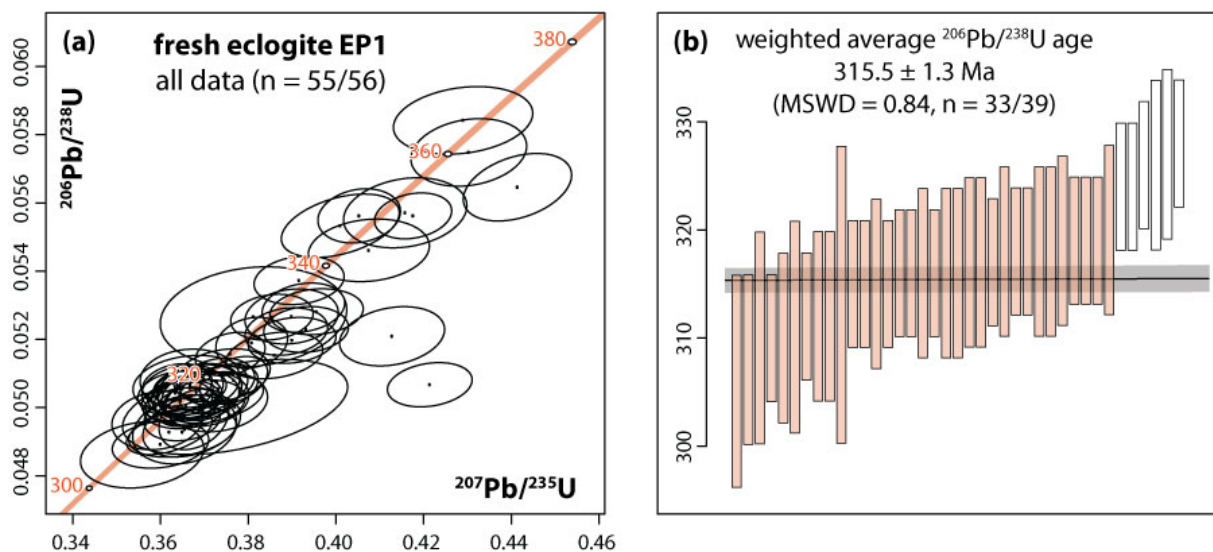


Figure 7. (a) Wetherill Concordia diagram for all the zircon younger than 380 Ma in the fresh eclogite sample EP1. (b) Weighted average $^{206}\text{Pb}/^{238}\text{U}$ age calculated with all the data younger than 330 Ma (6 outliers).

The measured U and Th contents are 68–1418 ppm and 1–126 ppm, respectively, and Th/U ratios span a range of 0.01–0.06, with one outlier at 0.16. There is no correlation between either the position of the analytical spots (inner vs. outer domain) or the U-Pb dates, and the Th/U ratios (Figure S3a, Table S6).

6.2 Retrogressed eclogite MN12-03

Zircon grains are subrounded to elongated, colourless and translucent, ranging from 100 to 400 μm . As in the fresh eclogite EP1, CL imaging revealed inner and outer domains and variously complex textures (Figure 6i-p), dominated by fir-tree zoning and sector zoning, observable in both domains. The interface between the inner and outer domains of many crystals crosscuts the internal zoning (Figure 6i,j,l-o). Some crystals show irregular concentric zoning or diffuse oscillatory zoning (Figure 6k).

Forty-eight analyses were performed on 20 zircon crystals. Thirty-nine analyses plot in a concordant position and yield $^{206}\text{Pb}/^{238}\text{U}$ dates spreading between 349 ± 5 and 302 ± 4 Ma (Figure 8a; Table S8). A coherent group of 41 analyses yields a weighted average $^{206}\text{Pb}/^{238}\text{U}$ date of 314.2 ± 1.1 (± 6.1) Ma (MSWD = 1.07; Figure 8b). Some crystals displaying significantly older cores (c. 340–350 Ma) have rims dated around 315 Ma (Figure 6k-m). Others appear homogeneous in terms of age at c. 315 Ma (Figure 6i,j,o). Rare grains with 315 Ma cores are surrounded by rims as young as 302 Ma (Figure 6p). The measured U and Th contents range 104–573 ppm and 1–21 ppm, respectively, and Th/U ratios 0.01–0.05. As for the fresh eclogite, there is no correlation between either the position of the analytical spots (inner vs. outer domain) or the U-Pb dates, and the Th/U ratios, although the five oldest dates correspond to inner domains (Figure S3b, Table S8).

Monazite found in the retrogressed eclogite (MN12-03) forms subhedral to anhedral crystals that are either unzoned or display a relatively simple zoning, as revealed by backscattered electron (BSE) imaging (Figure S4). Twenty-nine analyses were done on 19 monazite grains *in-context* directly in thin section and yield a concordia date of 311.4 ± 1.2 (± 6.0) Ma (MSWD = 1.2, $n = 23$) (Figure S5, Table S10). The younger apparent ages are discussed below.

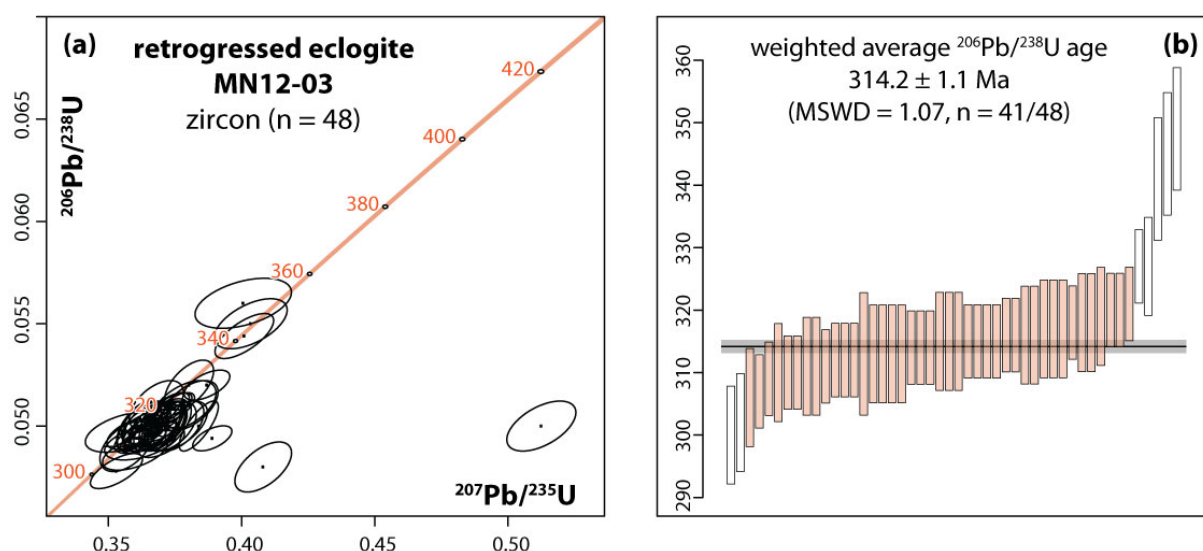


Figure 8. (a) Wetherill Concordia diagram for all the zircon data obtained in the retrogressed eclogite sample MN12-03. (b) Weighted average $^{206}\text{Pb}/^{238}\text{U}$ age calculated with all the data (7 outliers).

6.3 Migmatite EP5

No monazite was found in the migmatite (sample EP5) directly adjacent to the eclogite boudins. Zircon grains are translucent and colourless, ranging in size from 210 to 460 μm . Most crystals are elongated, and some are sub-rounded (Figure 6q-t). CL imaging revealed various inner and outer domains, commonly displaying concentric zones characterised by significantly different apparent ages (Figure 6q). Forty-eight analyses were performed on twenty-two different grains. Plotted in a Wetherill Concordia diagram (Figure 9a), the analyses are in a concordant to discordant position, with apparent ages ranging from c. 2610 down to c. 217 Ma (Table S11). The measured U and Th contents range 48–8717 ppm (most measures < 3500 ppm) and 1–260 ppm (most measures < 80 ppm), respectively, and Th/U ratios 0.001–0.94. All analytical spots with $^{206}\text{Pb}/^{238}\text{U}$ dates younger than 400 Ma ($n = 28$) have Th/U ratios < 0.02, and there is no correlation between the U-Pb dates and the Th/U ratios.

The youngest group of thirteen concordant dates (concordance = $100 \pm 2\%$) was acquired on the outermost overgrowths observed on zircon crystals (Figure 6q,r,t; green ellipses on Figure 9b). It yields a concordia date of 310.4 ± 5.0 (± 7.7) Ma (MSWD = 0.85, $n = 13$). Although 98 % concordant, two analyses (26 and 27) appear to yield apparent ages that are c. 10–15 Myr younger than the 11 remaining ones. If they are discarded from the calculation, the eleven remaining analyses yield a concordia date of 316.2 ± 5.8 (± 8.3) Ma (MSWD = 0.34, $n = 11$, not shown). Although the 310.4 ± 5.0 Ma and 316.2 ± 5.8 Ma dates are indistinguishable within error, we note that c. 316 Ma is strikingly similar to the 315 Ma dates commonly found in the eclogites.

Because the analyses were performed on the outer rim of the zircon grains and, although slightly different in absolute values, these two dates are indistinguishable within error, we conclude that the last event recorded by the zircon grains in the migmatite is c. 315–310 Ma old. In this scenario, the few analyses yielding younger $^{206}\text{Pb}/^{238}\text{U}$ dates (Figure 9b) are attributed to Pb loss.

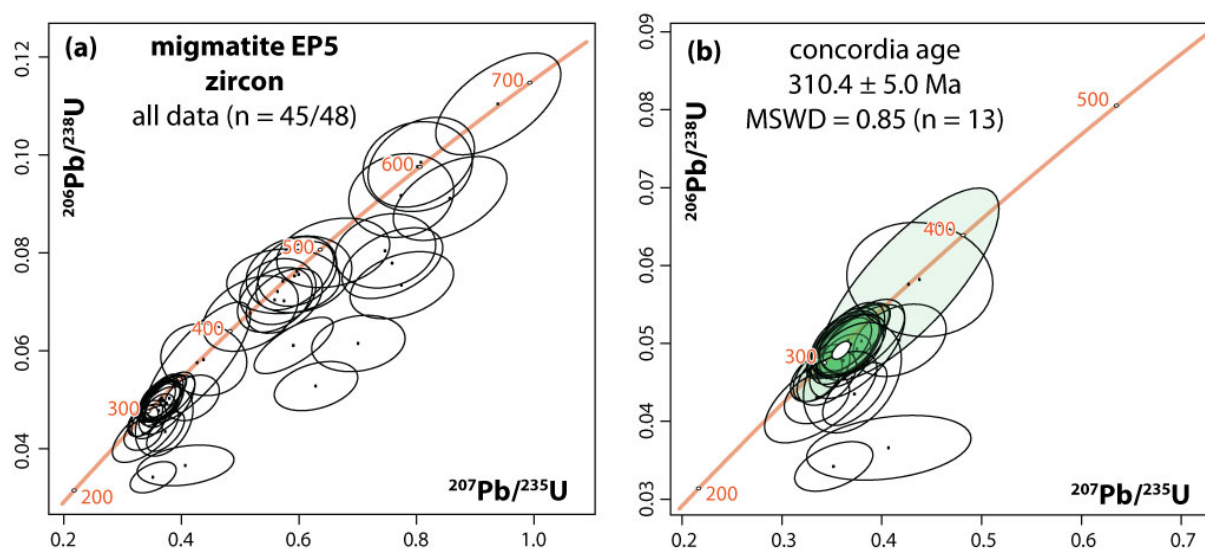


Figure 9. (a) and (b) Wetherill Concordia diagrams for the migmatite sample EP5: (a) for all the zircon younger than 700 Ma ($n = 45/48$), and (b) Concordia age calculated with the youngest analyses that are 98 % concordant or better.

6.4 Summary of zircon data

Zircon from the eclogite samples displays various domains and textures. Locally, the interface between the domains crosscuts the internal zoning. Yet, the zircon grains and their domains are similar, with relatively weak zoning, which would be in line with growth in similar conditions for all the zircon crystals. The internal patterns in the zircon crystals are similar to zircon that crystallised at high metamorphic temperatures and pressures (Corfu, Hanchar, Hoskin, & Kinny, 2003). Consistently, all but one Th/U ratios are lower than 0.1, also suggesting a metamorphic origin (Rubatto, 2002; 2017). The analysed zircon grains yield a range of concordant apparent ages that spread from 366 ± 5 to 306 ± 5 Ma (349 ± 5 to 302 ± 4 Ma in the retrogressed eclogite), with dominant data clusters that give an age of c. 315 Ma in both the fresh (315.5 ± 1.3 Ma) and the retrogressed (314.2 ± 1.1 Ma) eclogite samples.

Zircon crystals from the migmatite show abundant inherited cores. Analyses from the rims yield a major cluster (n=13) between c. 315 and 310 Ma. In agreement with petrological data (section 4) and phase equilibrium modelling (section 8.1, below) it is inferred that these dates correspond to the crystallisation of partial melt during isobaric cooling at low pressure (~6 kbar). Indeed, zircon in migmatites typically dissolves as rocks cross melting reactions, and grows during cooling (e.g. Kelsey et al., 2008; Kelsey & Powell, 2011; Kohn et al., 2015; Yakymchuk & Brown, 2014). This is not incompatible with the low Th/U ratios (Yakymchuk, Kirkland, & Clark, 2018), and is also in agreement with existing data on the age of migmatitisation in the Montagne Noire region (e.g. Poujol et al., 2017; Trap et al., 2017).

7 REE SPECTRA

With the exception of one analysis, all zircon spectra in the fresh eclogite EP1 show similar patterns (Figure 10a), marked by the absence of a negative Eu anomaly ($\text{Eu}_N/\text{Eu}^* = 0.84\text{--}1.15$) and a flat HREE trend. Gd_N/Lu_N ranges 0.62–1.39 (n = 45) with five outliers (0.41, 1.59–2.19; Figure S6). In more detail, the spectra cover a range of normalised HREE concentrations (~10–80) and the individual patterns are not exactly the same, as some have a slightly negative and others slightly positive HREE slope. There is no correlation, however, with the corresponding dates or the positions of the analytical spots (inner vs. outer zone; Figures 10a and S6a). One zircon core that could not be dated because of a fracture in the crystal has a negative Eu anomaly ($\text{Eu}_N/\text{Eu}^* = 0.15$) and an HREE-enriched spectrum ($\text{Gd}_N/\text{Lu}_N = 0.07$) (Figures 10a and 11a, Table S7 #51).

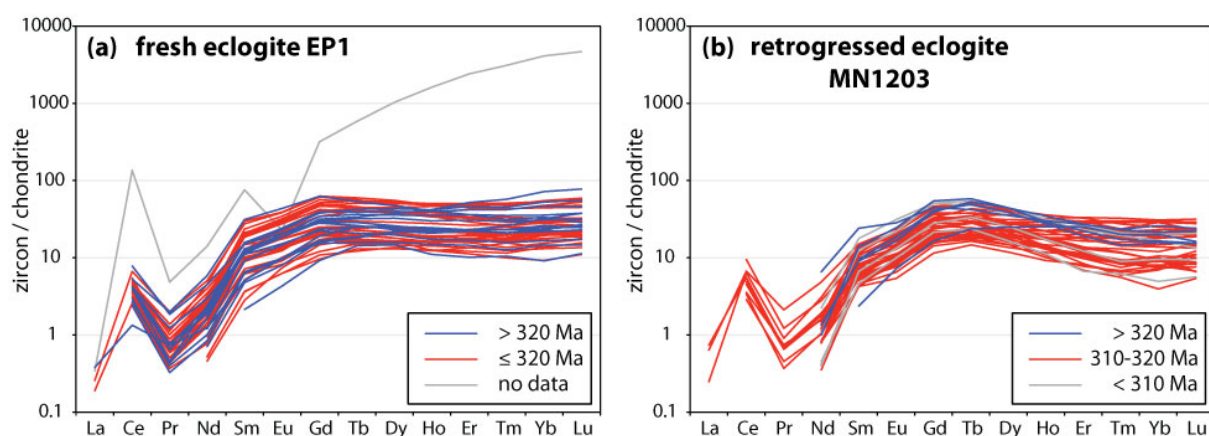


Figure 10. Chondrite-normalized REE spectra, colour-coded by the corresponding $^{206}\text{Pb}/^{238}\text{U}$ date, for all zircon analyses from the fresh eclogite EP1 (a) and the retrogressed eclogite MN12-03 (b). All spectra are similar with flat HREE and no negative Eu anomaly, except for one core analysis. Many spectra in the retrogressed eclogite MN12-03 have a slight bell shape with highest values at Gd and Tb and a weak negative slope towards heavier HREE (cf. Figure S6). Chondrite values of McDonough and Sun (1995).

Similarly, in the retrogressed sample MN12-03, zircon REE spectra show neither a negative Eu anomaly ($\text{Eu}_N/\text{Eu}^* = 0.77\text{--}1.05$; with one outlier at 1.16) nor enrichment in HREE (Gd_N/Lu_N ranges 0.86–3.81; Figures 10b, S6b). This span of Gd_N/Lu_N values corresponds to a range of spectra between those with a flat HREE pattern and those displaying a “humped” pattern with a maximum at Gd and Tb, and negatively sloping HREE. However, there is no correlation between the shapes of the REE patterns and the corresponding dates or the positions of the analytical spots, although the inner zircon zones tend to show more negatively sloping HREE patterns (Figure S6b).

Garnet in the fresh eclogite EP1 shows a strong rimward decrease in HREE (Dy 19.0→3.3 ppm, Yb 13.3→0.4 ppm) and a weak irregular variation of Sm (0.7–1.9 ppm; Figure S7, Table S12). Garnet in the retrogressed eclogite MN12-03 has significantly lower REE abundances and the trend is less pronounced. Garnet in both samples is enriched in HREE with respect to LREE and lacks a negative Eu anomaly. The slope of the chondrite-normalised HREE is flat in the core and negatively sloping in the rim (Figure S7f). Amphibole and clinopyroxene show a bell-shaped pattern with a maximum at Nd and Sm, and depleted HREE (Figure S8, Table S13). Primary amphibole in sample EP1 has no negative Eu anomaly (Figure S8a), whereas amphibole from symplectites in the retrogressed eclogite MN12-03 has a marked negative Eu anomaly (Figure S8c). Plagioclase from MN12-03 has a characteristic positive peak in Eu (Figure S8d).

To test the chemical equilibrium between zircon and garnet, partition coefficients between the two phases ($D_{\text{REEZircon/garnet}}$) have been calculated and represented in array plots (as proposed by Taylor et al., 2017) as well as in classic REE plots (Figure S9). The shape, slope and absolute values of the REE plots depend strongly on the garnet composition (core, rim) used. When the zircon medium-to-heavy-REE values are normalized to those of the garnet cores (Figure S9a,c), the partitioning pattern displays a concave-up shape that progressively flattens towards the heavier REE. This pattern is comparable to the experimental results of Taylor et al. (2015), conducted at relatively low pressures (7 kbar). When the same zircon data are compared to the values of the garnet rim (Figure S9e), they yield a pattern with a positive slope from Gd to Lu with a marked preference of zircon for the HREE ($D_{\text{Lu}} = 6.6\text{--}34.3$). This pattern is comparable with the experimental results of Rubatto and Hermann (2007) conducted at high pressures (20 kbar). However, regardless of the garnet composition used, zircon data form a cloud of points on the array plots (rather than a linear trend), whatever the corresponding U-Pb date of the analyses (Figure S9b,d). Although this lack of correlation could question the crystallisation of zircon in equilibrium with garnet, the relatively low temperatures reached by the rocks and the strong chemical zoning of garnet make the use of the array plot unfortunately inappropriate (Harley & Taylor, personal communication during the review process).

Figure 11 sums up the observations. There is no correlation between the REE patterns and apparent U-Pb ages in zircon from the eclogites. A significant interval of U-Pb zircon dates spreading from 366 Ma to 306 Ma corresponds to one trend in REE spectra for the fresh eclogite (EP1). The same REE pattern is associated with dates ranging from 349 to 302 Ma in the retrogressed eclogite (MN12-03). Unfortunately, the zone characterised by the HREE-enriched spectrum with a negative Eu anomaly (Figure 11a) could not be dated because of the presence of a crack in the grain.

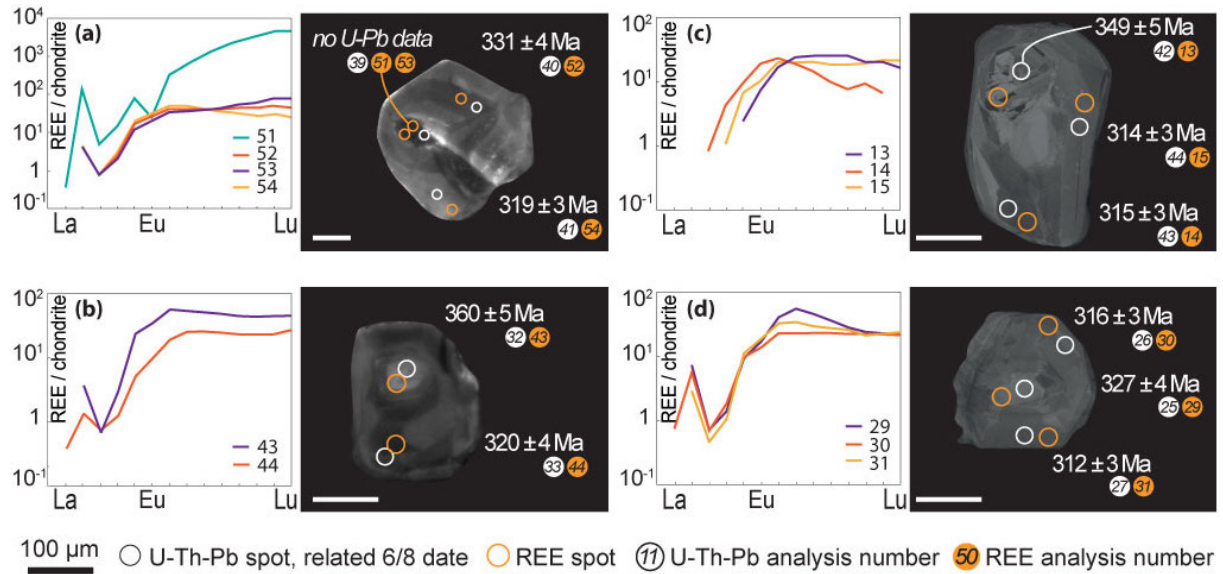


Figure 11. Absence of correlation between U-Pb dates and REE patterns in zoned zircons from eclogites (EP1: a-b; MN12-03: c-d). Zircon zones yield various dates, but similar REE patterns with flat HREE and no negative Eu anomaly, typical for eclogite-facies equilibration.

8 *P-T* ESTIMATIONS

8.1 Pseudosections

In the *P-T* pseudosection (Figure 12), the dominant assemblage of sample EP1 (garnet, omphacite, amphibole, kyanite, rutile, quartz) is stable at $P > 17$ kbar and $T > 670^\circ\text{C}$. Using garnet chemical zoning and calculated compositional isopleths, it is inferred that the composition of the garnet core ($X_{\text{Mg}} = 0.44$, $\text{Grs} = 23$) corresponds to equilibration conditions of ~ 19.5 kbar, 700°C . Garnet crystallised along a prograde *P-T* path that reached peak pressure conditions at ~ 21 kbar and 750°C ($X_{\text{Mg}} = 0.58\text{--}0.60$; $\text{Grs} = 12\text{--}15$) in the field g-cpx-am-q-ru-ky (Figure 6). The conditions correspond to the eclogite facies and are close to the quartz- and amphibole-out lines, in agreement with the low proportion of both minerals in the dominant assemblage. Removing the contribution of the zoned garnet core from the effective bulk composition does not significantly modify the results (Figure 12b), but provides an even better fit with the observed garnet rim composition. Subsequent development of plagioclase-bearing symplectite and the replacement of rutile by ilmenite testify to decompression during exhumation. The presence of spinel and orthopyroxene in the symplectites and the unusually high Mg content of ilmenite suggest high temperatures (e.g. Chu, Ague, Axler, & Tian, 2016). In the pseudosection calculated for the bulk composition without the garnet cores at low pressures (Figure S10), the symplectitic matrix assemblage plagioclase, amphibole, diopsidic clinopyroxene, ilmenite \pm rutile is stable at $P < 7.5$ kbar and $T > 750^\circ\text{C}$. However, orthopyroxene and spinel are not modelled in this diagram. Indeed, given the local and domainal development of the symplectitic assemblages, phase diagrams calculated for the whole-rock composition can indicate the general qualitative trends, but are not appropriate for constraining the *P-T* conditions quantitatively.

None of the various pseudosections for the retrogressed eclogite MN12-03 (calculated for the analysed whole-rock composition, thin section-scale bulk composition, including or not the garnet core; not presented) yielded useful results. At best, the calcic amphibole, cummingtonite, plagioclase, biotite, quartz, ilmenite assemblage is stable at pressures lower than ~ 8 kbar, without yielding constraints on the temperature conditions. The observed core-to-rim increase of anorthite is compatible with an evolution dominated by decompression.

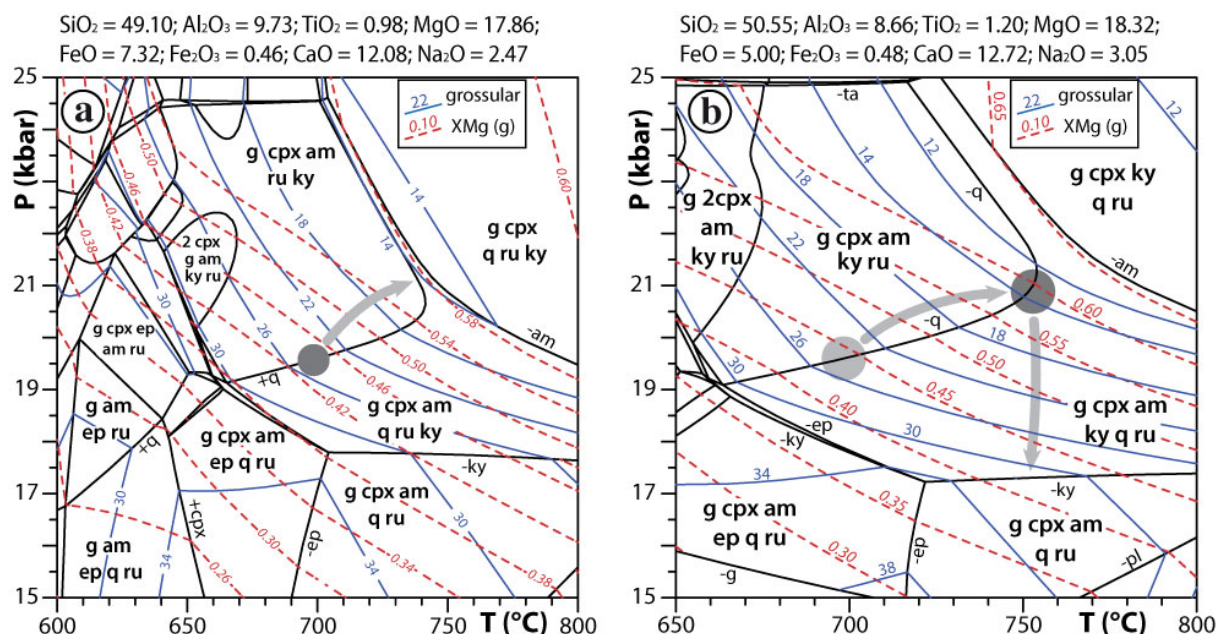


Figure 12. P - T pseudosections and garnet compositional isopleths for the fresh eclogite EP1, calculated for (a) the analysed bulk composition (indicated in mol.%) and (b) a composition that results from the removal of the garnet cores from the analysed composition (a). H_2O is in excess. Only main fields are labelled. $X_{Mg}(g)$ = molar $Mg/(Mg+Fe^{2+})$, grossular = molar $Ca/(Ca+Mg+Fe^{2+})$. Arrows indicate the inferred P - T path based on the composition of the garnet core (grey dot in a) and rim (dark grey dot in b) and the garnet growth zoning. Decompression is qualitative only and is inferred from the development of plagioclase-bearing symplectites at the expense of garnet and clinopyroxene, the replacement of rutile by ilmenite (Figure S2) and the P - T conditions of the surrounding migmatite (Figure 13).

In the P - T pseudosection calculated for the composition of the migmatite EP5 (Figure 13), the assemblage quartz, plagioclase, K-feldspar, biotite, sillimanite, garnet, ilmenite + melt is stable at 650–750°C, 3–9 kbar. Using the calculated compositional isopleths, the composition of the garnet and plagioclase core (Grs = 2, Sps = 10; An19) suggests equilibration at ~6 kbar, 730°C. The partial resorption of garnet, accompanied by the increase of spessartine, the decrease of the anorthite proportion in plagioclase (down to An12), and the local crystallisation of muscovite are compatible with an isobaric cooling to ~690°C.

8.2 Ti-in-zircon thermometry

Titanium concentration in zircon has been measured in the zircon crystals together with the REE by LA-ICP-MS. Zircon from the eclogite EP1 has Ti contents ranging between 4.3 and 16.0 ppm, with two outliers at 57.4 and 2716.3 ppm. Using the calibration of Watson, Wark, and Thomas (2006), this corresponds to a range of 672–784°C, in good agreement with temperature estimates from the phase diagrams. Similarly, zircon from the retrogressed eclogite MN12-03 has Ti concentrations between 4.2 and 16.4 ppm. The calibration of Watson et al. (2006), yields a temperature range of 669–786°C. In each of the samples, there is no correlation between the calculated temperatures and the position of the analyses (core or rim), or the corresponding U-Pb date (Figure S11).

SiO₂ = 83.12; Al₂O₃ = 8.855; TiO₂ = 0.11; MgO = 0.45; MnO = 0.06;
 FeO = 1.35; Fe₂O₃ = 0.02; CaO = 0.19; Na₂O = 2.08; K₂O = 3.765; H₂O = 5.00

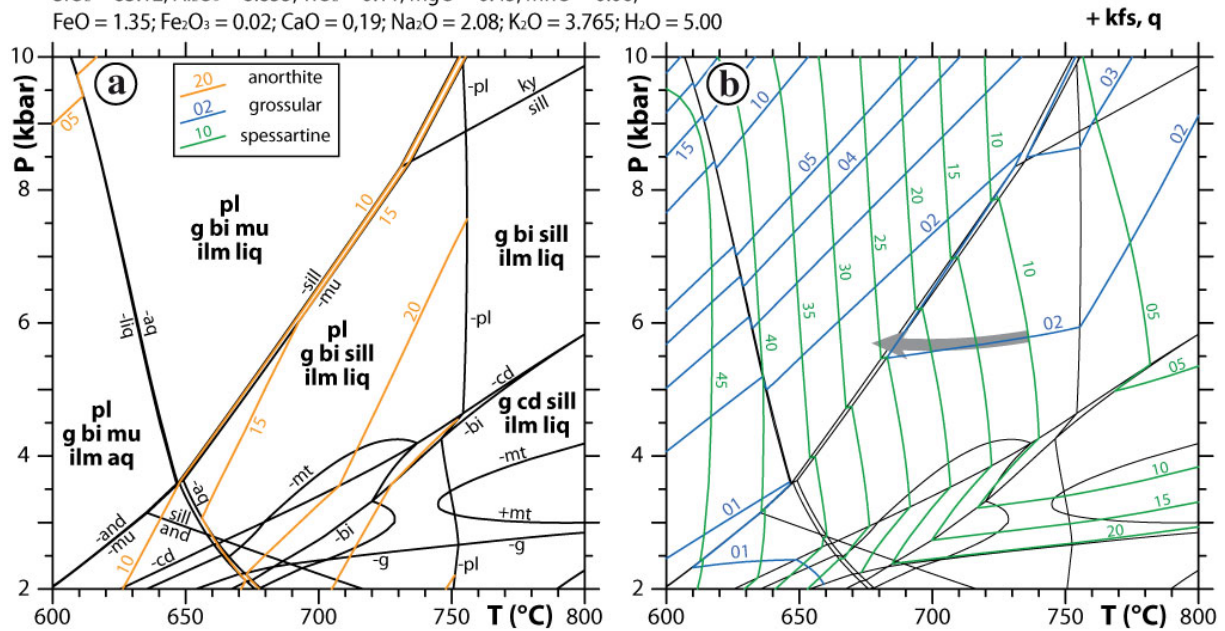


Figure 13. *P–T* pseudosections, and garnet and plagioclase compositional isopleths, calculated for the analysed bulk composition (indicated in mol.%) of the migmatite EP5. The amount of H₂O is estimated so that the rock is just saturated in aqueous fluid (aq) immediately below the solidus.

9 GEOLOGICAL CONSTRAINTS

The studied eclogites have oceanic protoliths and recorded a part of a prograde *P–T* path from ~19.5 kbar, 700°C to the pressure peak at ~21 kbar, 750°C. Subsequent exhumation to ~6 kbar, 730°C is constrained by the equilibration conditions of the embedding migmatite (and compatible with the qualitative inferences from the symplectites of the eclogite). Zircon overgrowths from the surrounding sillimanite-bearing migmatite yield a U-Pb age of c. 315–310 Ma interpreted as the age of the crystallisation of the partial melt during cooling at low pressures (~6 kbar).

In both the fresh and the retrogressed eclogitic samples, and independently from the nature of the analysed zircon domain, all the zircon REE spectra but one are characterised by the absence of Eu anomaly and flat HREE patterns, a trend usually interpreted as typical for eclogite-facies conditions (e.g. Rubatto, 2002; Whitehouse & Platt, 2003; Rubatto, 2017). Yet, the apparent U-Pb ages of zircon crystals from both eclogites spread from c. 360 Ma to a dominant data cluster in both samples at c. 315 Ma. At face value, this suggests the existence of an oceanic subduction leading to a prolonged eclogite-facies metamorphism from c. 360 Ma to the eclogite-facies pressure peak at c. 315 Ma, followed by fast exhumation (Figure 14a). However, there is no evidence either in the regional sedimentary or magmatic record for an oceanic subduction in the Montagne Noire area during this period.

Although high-grade metamorphic rocks including migmatites outcrop within its core, the Montagne Noire massif belongs to the southern external zones of the European Variscan belt, which are mainly composed of low- to non-metamorphic Palaeozoic sediments (e.g. Arthaud, Burg, & Matte, 1976; Burg & Matte, 1978; Franke, Doublier, Klama, Potel, & Wemmer, 2011, Padel et al., 2017). More precisely, from 360 Ma to 340 Ma, the Montagne Noire area was a shallow-marine carbonate platform that progressively deepened and merged into a foreland basin (e.g. Engel, Feist, & Franke, 1981). The basin fill ranges from deep clastic terrigenous sediments to paralic shales from 340 Ma to 320 Ma, respectively, showing progressive overfilling. Palaeozoic olistholiths embedded in a Late-Viséan to Serpukhovian

flysch of the basin attest to active tectonics during this period, resulting in the thrust-and-fold pattern of the Palaeozoic sedimentary units south of the Montagne Noire (Arthaud, 1970; Burg & Matte, 1978; Engel et al., 1981; Vachard, Izart, & Cózar, 2017). Finally, clastic continental Gzhelian and Lower-Permian deposits unconformably overlay these tectono-sedimentary units (e.g. Becq-Giraudon & Van Den Driessche, 1994; Châteauneuf, 1989). The only gap of ~5 Myr (from 320 to 315 Ma) in the sedimentation record can hardly account for the lack of evidence for a protracted subduction until 315 Ma.

Similarly, Variscan magmatism that develops in the Montagne Noire massif and adjacent areas is dominated by peraluminous granitoids associated with low-pressure migmatites that result from the partial melting of a sialic crust between 320 and 290 Ma (e.g. Poilvet et al., 2011; Poujol et al., 2017; Roger et al., 2015; Trap et al., 2017) and does not show any significant contamination from mantle sources as would be expected in the context of a long-lived oceanic subduction. Thus, there is definitely no geological evidence for an active oceanic subduction between 360 and 315 Ma in the Montagne Noire area. Finally, the existence of an active oceanic subduction at 315 Ma in the Variscan orogen challenges the generally accepted plate-tectonic reconstructions at the scale of the European Variscan belt (e.g. Ballèvre et al., 2014; Franke, Cocks, & Torsvik, 2017; Kroner & Romer, 2013; Lardeaux, 2014; Matte, 2001; Stampfli, Hochard, Vêrard, Wilhem, & von Raumer, 2013). On the other hand, abundant eclogites with peak-pressure ages of c. 360 Ma are known from the Lévêzou massif (Lotout et al., 2020), situated immediately to the north of the Montagne Noire massif (Figure 1).

10 DISCUSSION

Facing the conflict between the simplest explanation of our data and the regional geological constraints, alternative models are discussed below.

10.1 Eclogite P – T conditions

P – T conditions inferred for the fresh eclogite EP1 in this study are in the same temperature range (~750°C) but indicate significantly higher pressures for the eclogite-facies peak (21 vs. 14 kbar) than the estimations of Whitney et al. (2015). This difference cannot be accounted for by the absolute uncertainties related to the estimation of P – T conditions from calculated phase diagrams, which are of the order of ± 1 kbar and $\pm 50^\circ\text{C}$, comparable to those of conventional thermobarometry (Palin, Weller, Waters, & Dyck, 2016). The absolute uncertainties are difficult to estimate precisely, and have numerous sources, including uncertainties on the thermodynamic data of mineral end-members, a – x relations, and, importantly, the uncertainty related to the estimation of the effective bulk-rock composition (e.g. Powell & Holland, 2008). However, the relative uncertainties are significantly reduced when different metamorphic stages are compared for the same rock within the same chemical model system (cf. Worley & Powell, 2000). The strength of the phase-diagram approach is that, despite the absolute uncertainties, the relative position of the mineral-assemblage fields as well as the trends of the various isopleths are relatively robust. And so are the inferences on the P – T evolution, provided the petrography is carefully done (e.g. Powell & Holland, 2008). P – T pseudosections and associated compositional isopleths calculated for sample EP1 show a very good agreement with the observed mineral assemblages and the measured garnet compositions. They are also relatively insensitive to moderate variations of the bulk composition (cp. Figures 12a and b). This suggests that the inferred P – T conditions are robust and can be treated with a relatively high degree of confidence. The inferred peak pressure (~21 kbar) is incompatible with crustal thickening and implies the origin of the eclogites in a subduction zone.

The temperature estimates, both from the pseudosections (~700–750°C) and the Ti-in-zircon thermometry (~670–780°C), are compatible with the results of the Zr-in-rutile thermometer of Tomkins, Powell, and Ellis (2007) obtained by Whitney et al. (2015; ~670–780°C). On the other hand, the markedly lower pressure inferred by Whitney et al. (2015; 2020) can be related to the use of an inappropriate chemical system (not including Fe³⁺ and H₂O) and/or outdated mixing models (especially for clinopyroxene). In particular, considering an H₂O-absent system results in overestimating the stability of anhydrous assemblages towards low temperatures and pressures, and a generally unrealistic topology (e.g. orthopyroxene stable at 16 kbar 600°C in Figure 6b of Whitney et al., 2015). Importantly, the reasoning behind the pseudosections being calculated under anhydrous conditions, or with extremely low H₂O contents, is conceptually incorrect. Most metamorphic rocks undergo progressive dehydration during the prograde evolution, because of the dehydration character of most metamorphic reactions. Grain boundaries are consequently constantly filled with aqueous fluid, in equilibrium with the anhydrous minerals. Excess fluid leaves the system for mechanical reasons only. At high temperatures rocks are then by definition dehydrated (i.e. mostly composed of anhydrous minerals), but the absence of hydrous minerals does not mean that the system was H₂O-undersaturated. In the present case, H₂O saturation is also supported by the presence of amphibole as part of the prograde and peak mineral assemblage, and the consistency between observed and modelled mineral assemblages and mineral chemical compositions and zoning.

The unsuccessful calculations for the retrogressed eclogite MN12-03 could be attributed to the largely retrogressed, yet symplectic (i.e. not entirely equilibrated even at the thin section-scale) character of the sample, possibly at least partly modified by fluid-rock interaction (cf. section 5). This is supported by the presence of biotite and monazite and the rather unusual LREE enrichment, and leads to difficult estimation of the appropriate effective bulk rock composition for the calculation of isochemical phase diagrams.

The migmatites have recorded isobaric cooling from ~730°C to ~690°C at ~6 kbar. Since the eclogites are enclosed in the migmatites, these P–T conditions are inferred to represent also those that the eclogites reached following the decompression. However, the available data do not allow to determine whether the decompression was roughly isothermal or accompanied by cooling or heating.

10.2 Ages and REE patterns

Zircon data from the eclogite samples show a spread of U-Pb dates from c. 360 Ma to a dominant data cluster in both samples at c. 315 Ma. Yet, they are all characterised by a unique type of REE spectra (no Eu anomaly and flat HREE trend; Figure 11), characteristic of crystallisation under high-pressure, eclogite-facies conditions. Petrological data only support the existence of one eclogite-facies event rather than a successive burial-exhumation “yo-yo subduction” pattern as proposed for example by Rubatto et al. (2011) for the Western Alps. This would then signify that the studied samples have recorded a prolonged oceanic subduction and associated eclogite-facies metamorphism during more than 45 Myr, peaking at c. 315 Ma. However, this scenario, that is admittedly the simplest explanation of the geochronological, geochemical and petrological data, is not supported by regional geological constraints, and challenges the generally accepted plate-tectonic reconstructions at the scale of the European Variscan belt (see above).

In such a situation, it may be worthwhile to explore other possible explanations and, in particular, scrutinise the inferences from the U-Pb and REE data of zircon. As a matter of fact, it has been reported that the U-Pb system can evolve independently of the REE during the metamorphic evolution subsequent to zircon crystallisation (e.g. Peters, Ayers, Gao, & Liu, 2013; Štípská et al., 2016). In a recent study, Schmädicke et al. (2018) reported a case of fresh eclogites, where most zircon with ‘eclogitic’ REE spectra recorded a post-peak

reequilibrium age, rather than the age of the eclogite-facies metamorphism. In the case of the present study, four end-member scenarios can be considered to account for the results (Figure 14). They result from the combination of two factors: the mode of zircon formation (prolonged zircon crystallisation vs. partial recrystallisation), and the P - T conditions (zircon recording the prograde segment of the P - T path vs. the decompression).

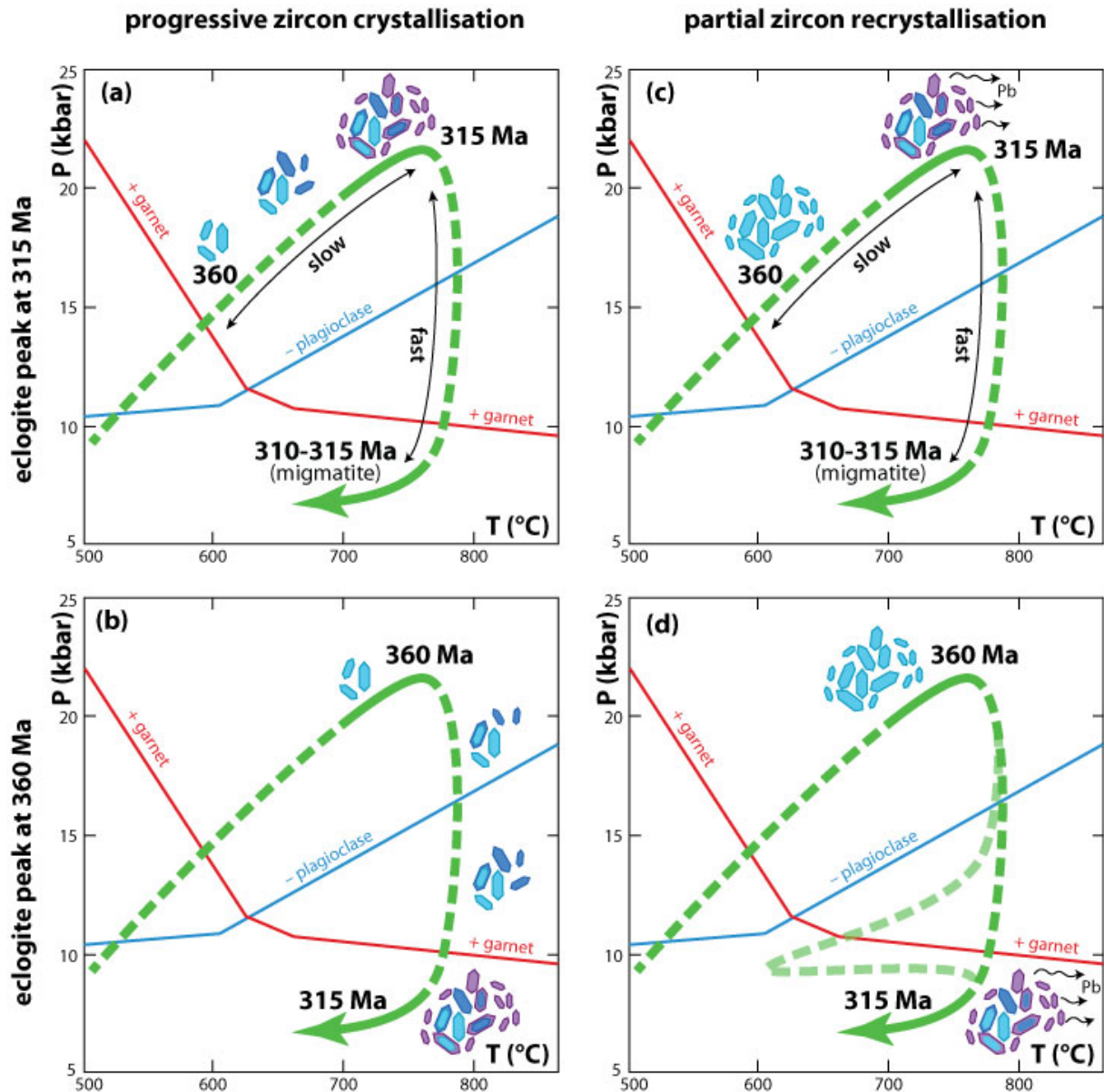


Figure 14. P - T - t sketches of the possible scenarios for zircon crystallisation in the Montagne Noire eclogites. Blue-violet crystals represent zircon; different colours correspond to different apparent ages (light blue – c. 360 Ma, violet – c. 315 Ma, dark blue – intermediate) of zircon formed at different P - T conditions (a and b) or affected to various degrees by recrystallisation-related Pb loss (c and d). Green arrow corresponds to the inferred P - T path. Lighter-coloured P - T path in (d) that involves cooling during decompression is intended to only convey the idea that the evolution could have been more complex than a simple isothermal decompression. See text for details.

10.2.1 Prolonged zircon growth

Given the spread of zircon U-Pb dates in the eclogite samples, zircon would have crystallised in several pulses or continuously between c. 360 and 315 Ma at different stages of the metamorphic evolution, corresponding to different P - T conditions. This could correspond to a

crystallisation along the prograde P – T path reaching the eclogite-facies pressure peak at c. 315 Ma (Figure 14a). Alternatively, zircon could crystallise progressively during decompression between the eclogite-facies pressure peak (reached at c. 360 Ma) and the low-pressure conditions characterising the surrounding migmatites, reached by c. 315 Ma (Figure 14b; cf. Kohn et al., 2015). In both cases, zircon crystals grown at different times would be expected to develop different trace-element patterns due to the progressively changing temperature and/or pressure, and/or sequestration of the HREE in the contemporaneously crystallising garnet, and/or the evolving mineral assemblage.

In the most straightforward scenario, both the REE spectra and the U-Pb data give accurate information, and record a continuous growth of zircon at P – T conditions progressively evolving in the eclogite-facies domain (Figure 14a). The persistence of HP conditions such as determined before would imply an active oceanic subduction from c. 360 to c. 315 Ma in the Montagne Noire area. This is incompatible with first-order geological constraints, discussed above. Nevertheless, if this hypothesis were correct, zircon crystals grown at different times would be expected to develop different trace-element patterns due to the progressively increasing temperature and sequestration of the HREE in the contemporaneously crystallising garnet. Indeed, garnet shows prograde growth zoning in both major and trace elements (Figures 2, S7). In particular, HREE are concentrated in the core and progressively depleted rimwards; the degree of depletion increases with the atomic number, resulting in progressively decreasing $(Yb/Gd)_N$ ratios (and increasing $(Gd/Lu)_N$ ratios) and the slope of the HREE spectra that evolves from flat to negatively sloping (Figure S7, Table S). Consequently, younger zircon should be more depleted in HREE and a correlation should be observed between the apparent age of the different zircon domains and the $(Gd/Lu)_N$ ratios. Yet, our data do not support such a correlation (Figure S6). Similarly, there is no correlation between the apparent age and the Ti-in-zircon temperature (Figure S11). Finally, this scenario calls upon continued volumetric zircon growth, which seems unlikely. After the dissolution of baddeleyite, ilmenite and epidote, possible sources of zirconium (Beckman et al., 2014; Bingen, Austrheim, & Whitehouse, 2001; Frei, Liebscher, Franz, & Dulski, 2004), the mineral composition of the rock does not change significantly in the eclogite facies (Figure 12) and no clear sources of Zr can therefore be identified (cf. Kohn et al., 2015). Consequently, trace-element data do not support the scenario of a prolonged (> 45 Myr) progressive zircon crystallisation under eclogite-facies conditions, in particular in equilibrium with garnet.

In the second scenario (Figure 14b), zircon still crystallised in several pulses or continuously between c. 360 and 315 Ma, according to the U-Pb data, but during decompression. Zirconium could be provided by the partial resorption of rutile, for example (e.g. Kohn et al., 2015). The apparent age of c. 315 Ma would correspond to zircon crystallisation at LP–HT rather than at eclogite-facies conditions. The ‘eclogitic’ REE patterns, similar in all zircon domains, would have been imposed by other factors, and are not representative of the P – T conditions that prevailed during zircon crystallisation.

However, if this scenario is correct, why would the zircon crystals be carrying a REE signature typical for eclogite-facies conditions (flat HREE pattern and lack a negative Eu anomaly) if they did not crystallise in the eclogite facies? The flat HREE pattern is easily explained by the metastable persistence of garnet in low-pressure conditions (cf. Kohn, 2016). Since garnet concentrates the HREE (Figure S7), no significant enrichment in HREE is possible in any newly formed zircon as long as the bulk of the rock’s HREE content remains sequestered in garnet. However, the absence of negative Eu anomaly, classically interpreted by the absence of plagioclase in the stable mineral assemblage (e.g. Hoskin, Kinny, Wyborn, & Chappell, 2000; Hoskin & Schaltegger, 2003; Murali, Parthasarathy, Mahadevan, & Das, 1983; Rubatto, 2002; Snyder, Taylor, & Crozaz, 1993) is more difficult to explain, in particular in the retrogressed eclogite, where amphibole in the coarse plagioclase-bearing

symplectites does develop a negative Eu anomaly (Figure S8). Furthermore, in mostly fresh eclogite EP1, zircon grains included in symplectites are significantly larger than the size of the symplectitic lamellae. Since in general zircon tends to be smaller than the main rock-forming minerals, this suggests that zircon crystals were initially included in the eclogite-facies minerals (now partly replaced by symplectites) rather than growing during the development of the symplectites. Consequently, none of the two scenarios where zircon would have crystallised between c. 360 and c. 315 Ma at different stages of the metamorphic evolution, be it along the prograde, eclogite-facies part of the P – T path, or during decompression, including the LP–HT stage, is supported by the observations.

10.2.2 Zircon recrystallisation

In this scenario, all the zircon grains would have crystallised in the eclogite facies, in agreement with their REE signatures. This is compatible with the observation that the zircon grains and their domains are similar, with relatively weak zoning, which would be in line with growth in very similar conditions for all the zircon crystals. The oldest dates found at c. 360 Ma would then correspond to the minimum age of this HP event. At c. 315 Ma, the zircon U-Pb systems were partly to totally reset. This could have happened either at the eclogite-facies peak (Figure 14c) or at low pressures (Figure 14d). If the U-Pb systems were reset totally, the grains would yield an age of 315 Ma, which is the case for most of the grains from the eclogite samples (Figures 7 and 8). If this scenario is correct, the position of the remaining data (i.e. between 360 and 315 Ma) would be linked to an incomplete reset of their U-Pb system. Indeed, given the relatively small difference in terms of absolute age between the two metamorphic events (360 Ma for the HP–HT and 315 Ma for the LP–HT), the uncertainty (several percent) on the individual analyses and the shape of the concordia curve for this time interval (Figures 7 and 8), a 315 Ma Pb loss affecting a 360 Ma old zircon grain, with different degrees of resetting, would produce data that are concordant within error although the individual apparent ages are meaningless (see Figure S12 for a mathematical simulation of this phenomenon).

Pb loss in zircon can be related to Pb diffusion or to zircon recrystallisation. Pb diffusion may not affect the internal crystal structure or the REE signature (e.g. Cherniak, Hanchar, & Watson, 1997; Cherniak & Watson, 2003; Kunz et al., 2018; Kusiak et al., 2013; Štípská et al., 2016; Whitehouse et al., 2014). However, the inferred temperature of the HP peak or the LP event ($\sim 750^\circ\text{C}$) is significantly lower than the one generally admitted for an efficient Pb diffusion in zircon ($\sim 900^\circ\text{C}$; e.g. Cherniak & Watson, 2001; Lee, Williams, & Ellis, 1997). Although the temperatures reached during the decompression of the eclogites are unknown, significantly higher temperatures seem unlikely, given the lack of recrystallisation and the preservation of garnet growth zoning, in particular in the fresh eclogite. Pb loss in zircon can also be related to recrystallisation (e.g. Cherniak & Watson, 2001; Hoskin & Black, 2000). This could be supported by the local crosscutting relationships between inner and outer part in several grains. Although other typical features (recrystallisation fronts, chaotic CL zoning) have not been clearly observed, recrystallisation is not always efficient enough to completely obliterate the affected grains and pre-existing textural features may be preserved (Hoskin & Black, 2000). In that case, these grains will keep a memory of their trace elements and isotopic composition, yielding mixed U-Pb apparent ages, such as the crystals presenting apparent ages between 360 and 315 Ma in this study. Consequently, the scenario compatible with most observations invokes one episode of zircon crystallisation, at c. 360 Ma, under eclogite-facies conditions, and a subsequent partial or total recrystallisation of most zircon crystals at c. 315 Ma. Yet, using sample-scale observations only, it is not possible to tell whether the recrystallisation occurred also under eclogite-facies conditions (Figure 14c) or at low pressures (Figure 14d). Geological constraints discussed above suggest that a subduction-related eclogite-facies event at c. 315 Ma is unlikely not only in the Montagne Noire but also

at the scale of the entire Variscan orogen. On the other hand, the age of c. 315 Ma is close to the age of the LP–HT metamorphism inferred from the embedding migmatite (see above). Widespread partial melting (documented at the scale of the entire Montagne Noire massif in the period between c. 320 and 290 Ma) and the associated fluid and melt percolation could enhance zircon recrystallisation at that moment. Such a percolation-enhanced recrystallisation could have affected all crystals present in the rock. If limited to the outer few μm of each crystal, though, it would have a greater effect proportionally on smaller crystals (like zircon) than on larger ones. To sum up, although other options cannot be firmly excluded, the scenario of zircon crystallisation at c. 360 Ma under eclogite-facies conditions, and its recrystallisation under LP–HT conditions at c. 315 Ma (Figure 14d) offers the best compromise between sample-scale, regional and orogen-scale constraints.

10.3 Significance of eclogite dates younger than 315 Ma

As argued above, the dominant c. 315 Ma dates are interpreted to result from partial to total resetting of the U–Pb system of zircon crystallised earlier under eclogite-facies conditions. The resetting is attributed to the LP–HT metamorphism, involving partial melting, as recorded in the migmatite enclosing the eclogite. In this scenario, the dates younger than c. 315–310 Ma can be attributed to further resetting due to either another melting event, or the long-lasting character of the same event. Indeed, Poujol et al. (2017) proposed that a second melting event affected the Montagne Noire at c. 295 Ma. Alternatively, Trap et al. (2017) argued for a protracted partial melting that would “have started at ca. 315 Ma and lasted 15–10 Myr”. It could also be directly related to the emplacement of granitic intrusions at 300–305 Ma (e.g. Poilvet et al., 2011; Roger et al., 2015) and in particular the Anglès granite (Trap et al., 2017), immediately adjacent to the sampling locality (Figure 1b).

The coarse-grained character of the symplectites in the retrogressed eclogite MN12-03, as well as the abundance of biotite and monazite, unusual in this type of rock, suggest that external fluids may have interacted with this eclogite at a late stage of the metamorphic evolution. The crystallisation of the surrounding migmatites could have been a possible source for these fluids. Monazite is known to (re)crystallise easily in the presence of fluids (e.g. Kelly, Harley, & Möller, 2012; Parrish, 1990; Spear & Pyle, 2002; Tartèse, Ruffet, Poujol, Boulvais, & Ireland, 2011). Consequently, we infer that the crystallisation of monazite either post-dated the c. 315 Ma recrystallisation of zircon in the retrogressed eclogite, or that monazite continued to recrystallise longer than zircon. This is compatible with the prolonged character of the Late-Carboniferous LP–HT event in the Montagne Noire that would have led to further local resetting of the U–Pb system in both the zircon and the monazite and would explain the occurrence of scarce dates younger than the main clusters (Figures 7, 8 and S5).

10.4 Age of the HP metamorphism

The data presented above suggest that the c. 315 Ma date is related to the LP–HT event, whereas the age of the eclogite-facies metamorphism would be around 360 Ma. The oldest concordant zircon date of 366 ± 5 Ma, recorded in the fresh eclogite, is identical within error to the Sm–Nd garnet age found in an eclogite from the same locality and interpreted as the age of the eclogite-facies metamorphism (357.5 ± 8.6 Ma, Faure et al., 2014). Whitney et al. (2015) rejected this age as that of the eclogite-facies metamorphism, arguing that the garnet rims (commonly containing most of the Sm and Nd) were not adequately represented in the dated aliquots. They consequently re-interpreted this date as corresponding to the age of a pre-eclogitic (likely amphibolite-facies) event. Our data show, however, that the garnet cores crystallised in the eclogite facies. Moreover, garnet only shows negligible zoning with respect to Sm and Nd, implying that dating the garnet is still representative of the age of the pressure peak. Consequently, in the absence of better data (such as Lu–Hf dating of garnet from the fresh eclogite), we consider that 360 Ma is the best available approximation of the minimum age of the high-pressure event in the studied eclogites.

The corollary of this is that despite its general robustness, zircon may, under certain circumstances, undergo significant recrystallisation that leads to decoupling the U-Pb and the REE record and consequently possibly deceptive inferences about the age of HP metamorphism. Such recrystallisation, probably fluid-driven, may preferentially affect the accessory phases of small size, such as zircon, whereas the main rock-forming minerals, subject to relatively inefficient intracrystalline diffusion, are not significantly affected. Accordingly, garnet appears to retain the original growth zoning, both in REE and in major elements in the fresh eclogite, and preserves the potential of yielding reliable P - T and age (Sm-Nd, Lu-Hf) information. Mostly recrystallised zircon preserves the REE signature of its original formation under eclogite-facies conditions, but the U-Pb system mostly reflects the low-pressure metamorphic stage.

10.5 Origin of the Montagne Noire eclogites

The last point is that as much as the geological constraints discussed above do not support eclogite-facies metamorphism in the Montagne Noire at 315 Ma, nor do they support it at 360 Ma. Consequently, the eclogites must have formed elsewhere. Eclogites related to oceanic subduction zones have been identified since long in the French Massif Central (e.g. Burg & Matte, 1978; Matte, 1986; Pin, 1990). With respect to the Montagne Noire, the closest area, where such rocks are found, is the Lévézou massif, at present located ~50 km to the north. It is noteworthy that the Montagne Noire eclogites bear striking similarities with those of the Lévézou massif. The Lévézou eclogites have similar geochemical characteristics (oceanic protolith), and reached similar P - T conditions (18–23 kbar, 680–800°C; Lotout et al., 2020) at a similar time (c. 360 Ma, Lu-Hf on garnet; Lotout et al., 2020). Furthermore, both massifs are separated by the Stephanian-Permian Saint-Affrique basin, and were consequently very close to one another before the late-Variscan collapse of the orogen and the associated Late Carboniferous-Permian extension (Burg et al., 1994). This suggests that the eclogites of the Montagne Noire originated in the same subduction zone as the eclogites of the Lévézou massif, at 360 Ma (Lotout et al., 2020). This subduction zone developed in the French Massif Central some 200 km north from the present location of the Lévézou massif (Burg & Matte, 1978; Matte, 1986).

The Lévézou eclogites were rapidly exhumed from nearly 70 km to 30 km at c. 350 Ma (Lotout et al., 2020). This exhumation was favoured by the thinning of the upper plate during slab rollback. The later collisional stage is responsible for crustal-scale southward thrusting resulting in the complex folded nappe of the Lévézou massif as a whole (e.g. Burg & Matte, 1978; Burg, Delor, Leyreloup, & Romney, 1989; Duguet & Faure, 2004; Matte, 1986).

The Montagne Noire eclogites may represent some part of the Lévézou eclogites that were only partly exhumed and translated further south by ductile flow during compressive tectonics, then to their present location in the Montagne Noire massif. Post-thickening extension, which started at c. 320 Ma and lasted until c. 290 Ma (Poujol et al., 2017) and was associated with widespread partial melting, is responsible for further exhumation of high-grade rocks of the Montagne Noire gneiss dome (Pfeifer, Soreghan, Pochat, Van Den Driessche & Thomson, 2016), including the eclogites, stacked at mid-crustal depths before the beginning of this event. The P - T path followed by the eclogites during such a tectonic evolution is unknown, but could have been more complex than a simple isothermal decompression (Figure 14d).

Whatever the exact P - T path, all zircon crystals in the eclogites would have crystallised in the eclogite facies, in agreement with their REE signatures. The oldest dates found at c. 360 Ma would correspond to the minimum age of this HP event. The younger dates, in particular at c. 315 Ma, which is intriguingly close to the age of the LP-HT metamorphism inferred from the embedding migmatite, would result from the partial to total resetting of the zircon U-

Pb systems. If so, dating zircon with ‘eclogitic’ REE patterns, would not unequivocally provide the age of a HP event.

11 CONCLUDING REMARKS

Unless appealing to an elusive major reappraisal of the geodynamics of the European Variscan belt, invoking an unsuspected north-dipping subduction zone far to the south of the Montagne Noire, geological constraints do not presently support the existence of a persistent subduction process up to 315 Ma, of which the Montagne Noire eclogites would be the relics. Alternatively, the universal pertinence of the usually accepted unequivocal relation between REE patterns in zircon and the age of the different major stages of the metamorphic evolution can be questioned, particularly in the case of migmatites-hosted eclogites. To date we do not have a definitive answer to this issue, as both hypotheses require a major questioning in their respective domains of investigation.

ACKNOWLEDGMENTS

E. Bretagne acknowledges Géosciences Rennes (CNRS UMR 6118) for her salary and the GeOHeLiS platform for the CL and LA-ICP-MS facilities. This research was supported by a CNRS-INSU grant (SYSTER program) and CGS internal grant 310400, accorded to P. Pitra. Xavier Le Coz, Nathan Hallot and Yann Lepagnot are thanked for making the thin sections, rock crushing and mineral separation, respectively. We are very grateful to Valérie Bosse for her help during the acquisition of the zircon REE spectra and CL images in Clermont-Ferrand. V. Janoušek is thanked for help with understanding the whole-rock chemical composition of the eclogites. We are sincerely grateful to Andrew Kylander-Clark, Richard Taylor, an anonymous reviewer and the editor Simon Harley for their detailed constructive comments, and to Nigel Kelly for a helpful review of an earlier version of this manuscript.

CONFLICT OF INTEREST

No conflict of interests to declare.

REFERENCES

- Arthaud, F. (1970). *Etude tectonique et microtectonique comparée de deux domaines hercyniens : les nappes de la Montagne Noire (France) et l'anticlinorium de l'Iglesiente (Sardaigne)*. Université Montpellier - Publication USTELA, série géologie structurale, 1, 175 p.
- Arthaud, F., Burg, J. P., & Matte, P. (1976). L'évolution structurale du massif de Mouthoumet (Sud de la France). *Bulletin de la Société Géologique de France*, (7) XVIII(4), 967-972.
- Ballèvre, M., Martínez Catalán, J. R., López-Carmona, A., Pitra, P., Abati, J., Díez Fernández, R., . . . Sánchez Martínez, S. (2014). Correlation of the nappe stack in the Ibero-Armorican arc across the Bay of Biscay: a joint French-Spanish project. In K. Schulmann, J. R. Martínez Catalán, J.-M. Lardeaux, V. Janoušek, & G. Oggiano (Eds.), *The Variscan Orogeny: Extent, Timescale and the Formation of the European Crust*, Geological Society, London, Special Publications, 405, pp. 77-113. London: The Geological Society.
- Ballouard, C., Boulvais, P., Poujol, M., Gapais, D., Yamato, P., Tartèse, R., & Cuney, M. (2015). Tectonic record, magmatic history and hydrothermal alteration in the Hercynian Guérande leucogranite, Armorican Massif, France. *Lithos*, 220-223, 1-22. doi: 10.1016/j.lithos.2015.01.027
- Beckman, V., Möller, C., Söderlund, U., Corfu, F., Pallon, J., & Chamberlain, K. R. (2014). Metamorphic zircon formation at the transition from gabbro to eclogite in Trollheimen–Surnadalen, Norwegian Caledonides. In F. Corfu, D. Gasser, & D. M. Chew (Eds.), *New Perspectives on the Caledonides of Scandinavia and Related Areas*, 390, pp. 403-424. London: The Geological Society. doi: 10.1144/SP390.26
- Becq-Giraudon, J. F., & Van Den Driessche, J. (1994). Dépôts périglaciaires dans le Stéphano-Autunien du Massif Central : témoin de l'effondrement gravitaire d'un haut plateau hercynien. *Comptes rendus de l'Académie des Sciences Paris, série II*, 318, 675-682.

- Bingen, B., Austrheim, H., & Whitehouse, M. (2001). Ilmenite as a Source for Zirconium during High-grade Metamorphism? Textural Evidence from the Caledonides of Western Norway and Implications for Zircon Geochronology. *Journal of Petrology*, 42, 355-375.
- Bogdanoff, S., Donnot, M., & Ellenberger, F. (1984). *Notice explicative. Carte géologique de la France à 1/50 000, feuille Bédarieux (#988)*. Orléans: BRGM.
- Bosse, V., Féraud, G., Ruffet, G., Ballèvre, M., Peucat, J.-J., & De Jong, K. (2000). Late Devonian subduction and early-orogenic exhumation of eclogite-facies rocks from the Champtoceaux Complex (Variscan belt, France). *Geological Journal*, 35, 297-325. doi: 10.1002/gj.864
- Boynton, W. V. (1984). Chapter 3 - Cosmochemistry of the Rare Earth Elements: Meteorite Studies. In P. Henderson (Ed.), *Rare Earth Element Geochemistry*, Developments in Geochemistry, 2, pp. 63-114: Elsevier.
- Brun, J.-P., & Van Den Driessche, J. (1994). Extensional gneiss domes and detachment fault systems: structure and kinematics. *Bulletin de la Société Géologique de France*, 165(6), 519-530.
- Burg, J. P., & Matte, P. J. (1978). A Cross Section through the French Massif Central and the Scope of its Variscan Geodynamic Evolution. *Zeitschrift der deutschen geologischen Gesellschaft*, 129, 429-460.
- Burg, J.-P., Delor, C. P., Leyreloup, A. F., & Romney, F. (1989). Inverted metamorphic zonation and Variscan thrust tectonics in the Rouergue area (Massif Central, France): P-T-t record from mineral to regional scale. In J. S. Daly, R. A. Cliff, & B. W. D. Yardley (Eds.), *Evolution of Metamorphic Belts*, Geological Society Special Publication, 43, pp. 423-439. Oxford: Blackwell Scientific Publications.
- Burg, J.-P., Van Den Driessche, J., & Brun, J.-P. (1994). Syn- to post-thickening extension in the Variscan Belt of Western Europe: Modes and structural consequences. *Géologie de la France*, 3, 33-51.
- Carignan, J., Hild, P., Mevelle, G., Morel, J., & Yeghicheyan, D. (2001). Routine analyses of trace elements in geological samples using flow injection and low pressure on-line liquid chromatography coupled to ICP-MS: a study of geochemical reference materials BR, DR-N, UB-N, AN-G and GH. *Geostandards Newsletter*, 25, 187-198. doi: 10.1111/j.1751-908X.2001.tb00595.x
- Châteauneuf, J. J. (1989). Le Permien français dans le contexte géodynamique et paléogéographique du socle varisque européen *Synthèse géologique des bassins permien français*, Mémoires du B.R.G.M., pp. 273-278. Orléans: BRGM.
- Cherniak, D. J., Hanchar, J. M. & Watson, E. B. (1997). Rare-earth diffusion in zircon. *Chemical Geology*, 134, 289-301. doi: 10.1016/S0009-2541(96)00098-8
- Cherniak, D. J., & Watson, E. B. (2001). Pb diffusion in zircon. *Chemical Geology*, 172(1), 5-24. doi: 10.1016/S0009-2541(00)00233-3
- Cherniak, D. J., & Watson, E. B. (2003). Diffusion in Zircon. *Reviews in Mineralogy and Geochemistry*, 53(1), 113-143. doi: 10.2113/0530113
- Chu, X., Ague, J. J., Axler, J. A., & Tian, M. (2016). Taconian retrograde eclogite from northwest Connecticut, USA, and its petrotectonic implications. *Lithos*, 240, 276-294. doi: 10.1016/j.lithos.2015.10.011
- Coggon, R., & Holland, T. J. B. (2002). Mixing properties of phengitic micas and revised garnet-phengite thermobarometers. *Journal of Metamorphic Geology*, 20(7), 683-696. doi: 10.1046/j.1525-1314.2002.00395.x
- Corfu, F., Hanchar, J. M., Hoskin, P. W. O., & Kinny, P. (2003). Atlas of Zircon Textures. *Reviews in Mineralogy and Geochemistry*, 53(1), 469-500. doi: 10.2113/0530469
- de Capitani, C., & Petrakakis, K. (2010). The computation of equilibrium assemblage diagrams with Theriak/Domino software. *American Mineralogist*, 95(7), 1006-1016. doi: 10.2138/am.2010.3354
- Demange, M. (1985). The eclogite-facies rocks of the Montagne Noire, France. *Chemical Geology*, 50(1), 173-188. doi: 10.1016/0009-2541(85)90119-6
- Demange, M., Guérangé-Lozes, J., & Guérangé, B. (1996). *Feuille de Lacaune n° 987 : Carte géologique de la France au 1:50000, Notice explicative par Demange, M., Guérangé-Lozes, J., Guérangé, B. et coll.* Orléans, France: Bureau de Recherches Géologiques et Minières.
- Diener, J. F. A., & Powell, R. (2012). Revised activity-composition models for clinopyroxene and amphibole. *Journal of Metamorphic Geology*, 30(2), 131-142. doi: 10.1111/j.1525-1314.2011.00959.x
- Duguet, M., & Faure, M. (2004). Successive shearing tectonics during the Hercynian collisional evolution of the southwestern French Massif Central. *Bulletin de la Société Géologique de France*, 175(1), 49-59.
- Engel, W., Feist, R., & Franke, W. (1981). Le Carbonifère anté-stéphanien de la Montagne Noire : rapports entre mise en place des nappes et sédimentation. *Bulletin du B.R.G.M. (2^e série)*, 4, 341-389.
- Faure, M., Cocherie, A., Gaché, J., Esnault, C., Guerrot, C., Rossi, P., . . . Qiuli, L. (2014). Middle Carboniferous intracontinental subduction in the Outer Zone of the Variscan Belt (Montagne Noire Axial Zone, French Massif Central): multimethod geochronological approach of polyphase metamorphism. In K. Schulmann, J. R. Martínez Catalán, J.-M. Lardeaux, V. Janoušek, & G. Oggiano (Eds.), *The Variscan Orogeny: Extent, Timescale and the Formation of the European Crust*, Geological Society, London, Special Publications, 405, pp. 289-311. London: The Geological Society. doi: 10.1144/SP405.2
- Franke, W., Cocks, L. R. M., & Torsvik, T. H. (2017). The Palaeozoic Variscan oceans revisited. *Gondwana Research*, 48, 257-284. doi: 10.1016/j.gr.2017.03.005

- Franke, W., Doublier, M. P., Klama, K., Potel, S., & Wemmer, K. (2011). Hot metamorphic core complex in a cold foreland. *International Journal of Earth Sciences*, *100*(4), 753-785. doi:10.1007/s00531-010-0512-7
- Frei, D., Liebscher, A., Franz, G., & Dulski, P. (2004). Trace Element Geochemistry of Epidote Minerals. *Reviews in Mineralogy and Geochemistry*, *56*(1), 553-605. doi:10.2138/gsrmg.56.1.553
- Gardien, V., Lardeaux, J.-M., Ledru, P., Allemand, P., & Guillot, S. (1997). Metamorphism during late orogenic extension; insights from the French Variscan belt. *Bulletin de la Société Géologique de France*, *168*(3), 271-286.
- Hastie, A. R., Kerr, A. C., Pearce, J. A., & Mitchell, S. F. (2007). Classification of altered volcanic island arc rocks using immobile trace elements: development of the Th-Co discrimination diagram. *Journal of Petrology*, *48*, 2341-2357. doi: 10.1093/petrology/egm062
- Holland, T., Baker, J., & Powell, R. (1998). Mixing properties and activity-composition relationships of chlorites in the system MgO-FeO-Al₂O₃-SiO₂-H₂O. *European Journal of Mineralogy*, *10*, 395-406. doi: 10.1127/ejm/10/3/0395
- Holland, T. J. B., & Powell, R. (1998). An internally consistent thermodynamic data set for phases of petrological interest. *Journal of Metamorphic Geology*, *16*(3), 309-343. doi: 10.1111/j.1525-1314.1998.00140.x
- Holland, T., & Powell, R. (2003). Activity-composition relations for phases in petrological calculations: an asymmetric multicomponent formulation. *Contributions to Mineralogy and Petrology*, *145*, 492-501. doi: 10.1007/s00410-003-0464-z
- Horstwood, M. S. A., Foster, G. L., Parrish, R. R., Noble, S. R., & Nowell, G. M. (2003). Common-Pb corrected in situ U-Pb accessory mineral geochronology by LA-MC-ICP-MS. *Journal of Analytical Atomic Spectrometry*, *18*(8), 837-846. doi: 10.1039/B304365G
- Horstwood, M. S. A., Košler, J., Gehrels, G., Jackson, S. E., McLean, N. M., Paton, C., ... Schoene, B. (2016). Community-Derived Standards for LA-ICP-MS U-(Th)-Pb Geochronology – Uncertainty Propagation, Age Interpretation and Data Reporting. *Geostandards and Geoanalytical Research*, *40*(3), 311-332. doi: 10.1111/j.1751-908X.2016.00379.x
- Hoskin, P. W. O., & Black, L. P. (2000). Metamorphic zircon formation by solid-state recrystallization of protolith igneous zircon. *Journal of Metamorphic Geology*, *18*(4), 423-439. doi: 10.1046/j.1525-1314.2000.00266.x
- Hoskin, P. W. O., Kinny, P. D., Wyborn, D., & Chappell, B. W. (2000). Identifying accessory mineral saturation during differentiation in granitoid magmas: an integrated approach. *Journal of Petrology*, *41*, 1365-1396. doi: 10.1093/petrology/41.9.1365
- Hoskin, P. W. O., & Schaltegger, U. (2003). The composition of zircon and igneous and metamorphic petrogenesis. In J. M. Hancher & P. W. O. Hoskin (Eds.), *Zircon*, Reviews in Mineralogy and Geochemistry, *53*, pp. 27-62. Washington, DC: Mineralogical Society of America and Geochemical Society. doi: 10.2113/0530027
- Janoušek, V., Aichler, J., Hanžl, P., Gerdes, A., Erban, V., Žáček, V., ... Žáčková, E. (2014). Constraining genesis and geotectonic setting of metavolcanic complexes: a multidisciplinary study of the Devonian Vrbno Group (Hrubý Jeseník Mts., Czech Republic). *International Journal of Earth Sciences*, *103*(2), 455-483. doi: 10.1007/s00531-013-0975-4
- Kalt, A., Corfu, F., & Wijbrans, J. R. (2000). Time calibration of a P-T path from a Variscan high-temperature low-pressure metamorphic complex (Bayerische Wald, Germany), and the detection of inherited monazite. *Contributions to Mineralogy and Petrology*, *138*(2), 143-163. doi: 10.1007/s004100050014
- Katayama, I., Maruyama, S., Parkinson, C. D., Terada, K., & Sano, Y. (2001). Ion micro-probe U-Pb zircon geochronology of peak and retrograde stages of ultrahigh-pressure metamorphic rocks from the Kokchetav massif, northern Kazakhstan. *Earth and Planetary Science Letters*, *188*(1), 185-198. doi: 10.1016/S0012-821X(01)00319-3
- Kelly, N. M., Harley, S. L., & Möller, A. (2012). Complexity in the behavior and recrystallization of monazite during high-T metamorphism and fluid infiltration. *Chemical Geology*, *322-323*, 192-208. doi: 10.1016/j.chemgeo.2012.07.001
- Kelsey, D. E., Clark, C., & Hand, M. (2008). Thermobarometric modelling of zircon and monazite growth in melt-bearing systems: examples using model metapelitic and metapsammitic granulites. *Journal of Metamorphic Geology*, *26*(2), 199-212.
- Kelsey, D. E., & Powell, R. (2011). Progress in linking accessory mineral growth and breakdown to major mineral evolution in metamorphic rocks: a thermodynamic approach in the Na₂O-CaO-K₂O-FeO-MgO-Al₂O₃-SiO₂-H₂O-TiO₂-ZrO₂ system. *Journal of Metamorphic Geology*, *29*(1), 151-166.
- Kohn, M. J. (2016). Metamorphic chronology – tool for all ages: Past achievements and future prospects. *American Mineralogist*, *101*(1), 25-42. doi: 10.2138/am-2016-5146
- Kohn, M. J., Corrie, S. L., & Markley, C. (2015). The fall and rise of metamorphic zircon. *American Mineralogist*, *100*, 897-908. doi: 10.2138/am-2015-5064

- Kohn, M. J., & Kelly, N. M. (2018). Petrology and geochronology of metamorphic zircon. In D. E. Moser, F. Corfu, J. R. Darling, S. M. Reddy, & K. Tait (Eds.), *Microstructural Geochronology: Planetary Records Down to Atom Scale*, Geophysical Monograph, 232, pp.: 35-61. doi: 10.1002/9781119227250.ch2
- Kroner, U., & Romer, R. L. (2013). Two plates – Many subduction zones: The Variscan orogeny reconsidered. *Gondwana Research*, 24(1), 298-329. doi: 10.1016/j.gr.2013.03.001
- Kunz, B. E., Regis, D., & Engi, M. (2018). Zircon ages in granulite facies rocks: decoupling from geochemistry above 850 °C? *Contributions to Mineralogy and Petrology*, 173(3), 26. doi: 10.1007/s00410-018-1454-5
- Kusiak, M. A., Whitehouse, M. J., Wilde, S. A., Dunkley, D. J., Menneken, M., Nemchin, A. A., & Clark, C. (2013). Changes in zircon chemistry during Archean UHT metamorphism in the Napier Complex, Antarctica. *American Journal of Science*, 313(9), 933-967. doi: 10.2475/09.2013.05
- Lardeaux, J.-M. (2014). Deciphering orogeny: a metamorphic perspective. Examples from European Alpine and Variscan belts. Part II: Variscan metamorphism in the French Massif Central – A review. *Bulletin de la Société Géologique de France*, 185(5), 281-310. doi: 10.2113/gssgfbull.185.5.281
- Lee, J. K. W., Williams, I. S., & Ellis, D. J. (1997). Pb, U and Th diffusion in natural zircon. *Nature*, 390(6656), 159-162.
- Liati, A., & Seidel, E. (1996). Metamorphic evolution and geochemistry of kyanite eclogites in central Rhodope, northern Greece. *Contributions to Mineralogy and Petrology*, 123, 293-307. doi: 10.1007/s004100050157
- Lotout, C., Pitra, P., Pujol, M., Anczkiewicz, R., & Van Den Driessche, J. (2018). Timing and duration of Variscan high-pressure metamorphism in the French Massif Central: a multimethod geochronological study from the Najac Massif. *Lithos*, 308-309, 381-394. doi: 10.1016/j.lithos.2018.03.022
- Lotout, C., Pujol, M., Pitra, P., Anczkiewicz, R., & Van Den Driessche, J. (2020) From burial to exhumation: emplacement and metamorphism of mafic eclogitic terranes constrained through multimethod petrochronology, case study from the Lévézou massif (French Massif Central, Variscan belt). *Journal of Petrology*, in press.
- Ludwig, K. R. (1998). On the Treatment of Concordant Uranium-Lead Ages. *Geochimica et Cosmochimica Acta*, 62, 665-676. doi: 10.1016/S0016-7037(98)00059-3
- Manzotti, P., Bosse, V., Pitra, P., Robyr, M., Schiavi, F., & Ballèvre, M. (2018). Exhumation rates in the Gran Paradiso Massif (Western Alps) constrained by in situ U–Th–Pb dating of accessory phases (monazite, allanite and xenotime). *Contributions to Mineralogy and Petrology*, 173(3), 24. doi:10.1007/s00410-018-1452-7
- Matte, P. (1986). Tectonics and plate tectonics model for the Variscan belt of Europe. *Tectonophysics*, 126, 329-374.
- Matte, P. (2001). The Variscan collage and orogeny (480-290 Ma) and the tectonic definition of the Armorica microplate: a review. *Terra nova*, 13(2), 122-128.
- McDonough, W. F., & Sun, S. S. (1995). The composition of the Earth. *Chemical Geology*, 120(3), 223-253. doi: 10.1016/0009-2541(94)00140-4
- Murali, A. V., Parthasarathy, R., Mahadevan, T. M., & Das, M. S. (1983). Trace element characteristics, REE patterns and partition coefficients of zircons from different geological environments—a case study on Indian zircons. *Geochimica et Cosmochimica Acta*, 47, 2047-2052. doi: 10.1016/0016-7037(83)90220-X
- Nicollet, C. (1978). Pétrologie et tectonique des terrains cristallins anté-permiens du versant sud du dôme du Lévézou (Rouergue, Massif central). *Bulletin du B.R.G.M. (2e série)*, 1978(3), 225-263.
- Padel, M., Álvaro, J. J., Clausen, S., Guillot, F., Pujol, M., Chichorro, M., . . . Vizcaïno, D. (2017). U–Pb laser ablation ICP-MS zircon dating across the Ediacaran–Cambrian transition of the Montagne Noire, southern France. *Comptes Rendus Geoscience*, 349(8), 380-390. doi: 10.1016/j.crte.2016.11.002
- Palin, R. M., Weller, O. M., Waters, D. J., & Dyck, B. (2016). Quantifying geological uncertainty in metamorphic phase equilibria modelling; a Monte Carlo assessment and implications for tectonic interpretations. *Geoscience Frontiers*, 7(4), 591-607. doi: 10.1016/j.gsf.2015.08.005
- Paquette, J. L., Ballèvre, M., Peucat, J. J., & Cornen, G. (2017). From opening to subduction of an oceanic domain constrained by LA-ICP-MS U-Pb zircon dating (Variscan belt, Southern Armorican Massif, France). *Lithos*, 294-295, 418-437. doi: 10.1016/j.lithos.2017.10.005
- Parrish, R. R. (1990). U–Pb dating of monazite and its application to geological problems. *Canadian Journal of Earth Sciences*, 27(11), 1431-1450. doi: 10.1139/e90-152
- Paton, C., Woodhead, J. D., Hellstrom, J. C., Hergt, J. M., Greig, A., & Maas, R. (2010). Improved laser ablation U-Pb zircon geochronology through robust downhole fractionation correction. *Geochemistry, Geophysics, Geosystems*, 11(3). doi: 10.1029/2009GC002618
- Paton, C., Hellstrom, J., Paul, B., Woodhead, J., & Hergt, J. (2011). Iolite: Freeware for the visualisation and processing of mass spectrometric data. *Journal of Analytical Atomic Spectrometry*, 26(12), 2508-2518. doi: 10.1039/C1JA10172B
- Pearce, J. A. (1996). A User's Guide to Basalt Discrimination Diagrams. In D. A. Wyman (Ed.), *Trace Element Geochemistry of Volcanic Rocks: Applications for Massive Sulphide Exploration*, Geological Association of Canada Short Course Notes, 12, pp. 79–113.

- Pearce, J. A. (2008). Geochemical fingerprinting of oceanic basalts with applications to ophiolite classification and the search for Archean oceanic crust. *Lithos*, *100*(1), 14-48. doi: 10.1016/j.lithos.2007.06.016
- Pearce, J. A. (2014). Immobile element fingerprinting of ophiolites. *Elements*, *10*, 101–108. doi: 10.2113/gselements.10.2.101
- Pearce, T. H., Gorman, B. E. & Birkett, T. C. (1977). The relationship between major element chemistry and tectonic environment of basic and intermediate volcanic rocks. *Earth and Planetary Science Letters*, *36*, 121-132. doi: 10.1016/0012-821X(77)90193-5
- Peters, T. J., Ayers, J. C., Gao, S., & Liu, X.-M. (2013). The origin and response of zircon in eclogite to metamorphism during the multi-stage evolution of the Huwan Shear Zone, China: Insights from Lu–Hf and U–Pb isotopic and trace element geochemistry. *Gondwana Research*, *23*(2), 726-747. doi: 10.1016/j.gr.2012.05.008
- Pfeifer, L. S., Soreghan G. S., Pochat, S., Van Den Driessche, J. & Thomson, S. N. (2016). Permian exhumation of the Montagne Noire core complex recorded in the Graissessac-Lodeve Basin, France. *Basin Research*, *30*, 1-14. doi: 10.1111/bre.12197
- Pin, C. (1990). Variscan oceans: Ages, origins and geodynamic implications inferred from geochemical and radiometric data. *Tectonophysics*, *177*, 215-227.
- Pitra, P., Ballèvre, M., & Ruffet, G. (2010). Inverted metamorphic field gradient towards a Variscan suture zone (Champtoceaux Complex, Armorican Massif, France). *Journal of Metamorphic Geology*, *28*(2), 183-208. doi: 10.1111/j.1525-1314.2009.00862.x
- Pitra, P., Boulvais, P., Antonoff, V., & Diot, H. (2008). Wagnerite in a cordierite-gedrite gneiss: Witness of long-term fluid-rock interaction in the continental crust (Ile d'Yeu, Armorican Massif, France). *American Mineralogist*, *93*, 315-326. doi: 10.2138/am.2008.2597
- Poilvet, J.-C., Poujol, M., Pitra, P., Van Den Driessche, J., & Paquette, J.-L. (2011). The Montalet granite, Montagne Noire, France: An Early Permian syn-extensional pluton as evidenced by new U-Th-Pb data on zircon and monazite. *Comptes Rendus Geoscience*, *343*(7), 454-461. doi: 10.1016/j.crte.2011.06.002
- Poujol, M., Pitra, P., Van Den Driessche, J., Tartèse, R., Ruffet, G., Paquette, J.-L., & Poilvet, J.-C. (2017). Two-stage partial melting during the Variscan extensional tectonics (Montagne Noire, France). *International Journal of Earth Sciences*, *106*, 477-500. doi: 10.1007/s00531-016-1369-1
- Powell, R., & Holland, T. J. B. (1988). An internally consistent dataset with uncertainties and correlations: 3. Applications to geobarometry, worked examples and a computer program. *Journal of Metamorphic Geology*, *6*, 173-204. doi: 10.1111/j.1525-1314.1988.tb00415.x
- Powell, R., & Holland, T. J. B. (2008). On thermobarometry. *Journal of Metamorphic Geology*, *26*(2), 155-179.
- Powell, R., Holland, T., & Worley, B. (1998). Calculating phase diagrams involving solid solutions via non-linear equations, with examples using THERMOCALC. *Journal of Metamorphic Geology*, *16*(4), 577-588. doi: 10.1111/j.1525-1314.1998.00157.x
- Roger, F., Teyssier, C., Respaut, J.-P., Rey, P. F., Jolivet, M., Whitney, D. L., . . . Brunel, M. (2015). Timing of formation and exhumation of the Montagne Noire double dome, French Massif Central. *Tectonophysics*, *640-641*, 53-69. doi: 10.1016/j.tecto.2014.12.002
- Roger, F., Teyssier, C., Whitney, D. L., Respaut, J.-P., Paquette, J.-L., & Rey, P. F. (2020). Age of metamorphism and deformation in the Montagne Noire dome (French Massif Central): Tapping into the memory of fine-grained gneisses using monazite U-Th-Pb geochronology. *Tectonophysics*, *776*, 228316. doi: 10.1016/j.tecto.2019.228316
- Rubatto, D. (2002). Zircon trace element geochemistry: partitioning with garnet and the link between U–Pb ages and metamorphism. *Chemical Geology*, *184*, 123–138. doi: 10.1016/S0009-2541(01)00355-2
- Rubatto, D. (2017). Zircon: The Metamorphic Mineral. In M. J. Kohn, M. Engi, & P. Lanari (Eds.), *Petrochronology: Methods and Applications*, Reviews in Mineralogy and Geochemistry, *83*, pp. 261-295. Washington, DC: Mineralogical Society of America and Geochemical Society. doi: 10.2138/rmg.2017.83.9
- Rubatto, D., & Hermann, J. (2007). Experimental zircon/melt and zircon/garnet trace element partitioning and implications for the geochronology of crustal rocks. *Chemical Geology*, *241*(1-2), 38-61. doi: 10.1016/j.chemgeo.2007.01.027
- Rubatto, D., Regis, D., Hermann, J., Boston, K., Engi, M., Beltrando, M., & McAlpine, S. R. B. (2011). Yo-yo subduction recorded by accessory minerals in the Italian Western Alps. *Nature Geoscience*, *4*(5), 338-342.
- Schmädicke, E., Will, T. M., Ling, X., Li, X.-H., & Li, Q.-L. (2018). Rare peak and ubiquitous post-peak zircon in eclogite: Constraints for the timing of UHP and HP metamorphism in Erzgebirge, Germany. *Lithos*, *322*, 250-267. doi: 10.1016/j.lithos.2018.10.017
- Snyder, G. A., Taylor, L. A., & Crozaz, G. (1993). Rare earth element selenochemistry of immiscible liquids and zircon at Apollo 14: an ion probe study of evolved rocks on the Moon. *Geochimica et Cosmochimica Acta*, *57*, 1143-1149. doi: 10.1016/0016-7037(93)90046-Y
- Spear, F. S., & Pyle, J. M. (2002). Apatite, Monazite, and Xenotime in Metamorphic Rocks. In M. J. Kohn, J. Rakovan, & J. M. Hughes (Eds.), *Phosphates: geochemical, geobiological, and materials importance*, Reviews in Mineralogy and Geochemistry, *48*, pp. 293-335. Washington, DC: Mineralogical Society of America and Geochemical Society. doi: 10.2138/rmg.2002.48.7

- Stampfli, G. M., Hochard, C., V  rard, C., Wilhem, C., & von Raumer, J. (2013). The formation of Pangea. *Tectonophysics*, 593, 1-19.
-   t  psk , P., Powell, R., Hacker, B. R., Holder, R., & Kylander-Clark, A. R. C. (2016). Uncoupled U/Pb and REE response in zircon during the transformation of eclogite to mafic and intermediate granulite (Blansk y les, Bohemian Massif). *Journal of Metamorphic Geology*, 34(6), 551-572. doi: 10.1111/jmg.12193
- Sun, S. S., & McDonough, W. F. (1989). Chemical and isotopic systematics of oceanic basalts: implications for mantle composition and processes. In A. D. Saunders & M. Norry (Eds.), *Magmatism in Ocean Basins*, Geological Society of London Special Publications, 42, pp. 313-345.
- Tart  se, R., Ruffet, G., Poujol, M., Boulvais, P., & Ireland, T. R. (2011). Simultaneous resetting of the muscovite K-Ar and monazite U-Pb geochronometers: a story of fluids. *Terra nova*, 23(6), 390-398. doi: 10.1111/j.1365-3121.2011.01024.x
- Taylor, R. J. M., Harley, S. L., Hinton, R. W., Elphick, S., Clark, C., & Kelly, N. M. (2015). Experimental determination of REE partition coefficients between zircon, garnet and melt: a key to understanding high-T crustal processes. *Journal of Metamorphic Geology*, 33(3), 231-248. doi:10.1111/jmg.12118
- Taylor, R. J. M., Clark, C., Harley, S. L., Kylander-Clark, A. R. C., Hacker, B. R., & Kinny, P. D. (2017). Interpreting granulite facies events through rare earth element partitioning arrays. *Journal of Metamorphic Geology*, 35(7), 759-775. doi: 10.1111/jmg.12254
- Tomkins, H. S., Powell, R., & Ellis, D. J. (2007). The pressure dependence of the zirconium-in-rutile thermometer. *Journal of Metamorphic Geology*, 25(6), 703-713. doi: 10.1111/j.1525-1314.2007.00724.x
- Tracy, R. J. (1982). Compositional zoning and inclusions in metamorphic minerals. In J. M. Ferry (Ed.), *Characterization of metamorphism through mineral equilibria*, Reviews in Mineralogy, 10, pp. 355-397: Mineralogical Society of America.
- Trap, P., Roger, F., Cenko-Tok, B., & Paquette, J.-L. (2017). Timing and duration of partial melting and magmatism in the Variscan Montagne Noire gneiss dome (French Massif Central). *International Journal of Earth Sciences*, 106(2), 453-476. doi: 10.1007/s00531-016-1417-x
- Vachard, D., Izart, A., & C  zar, P. (2017). Mississippian (middle Tournaisian-late Serpukhovian) lithostratigraphic and tectonosedimentary units of the southeastern Montagne Noire (H  rault, France). *G  ologie de la France*, 2017, 47-88.
- Van Den Driessche, J., & Brun, J.-P. (1992). Tectonic evolution of the Montagne Noire (french Massif Central): a model of extensional gneiss dome. *Geodinamica Acta*, 5(1-2), 85-99. doi: 10.1080/09853111.1992.11105221
- Vermeesch, P. (2018). IsoplotR: A free and open toolbox for geochronology. *Geoscience Frontiers*, 9, 1479-1493. doi: 10.1016/j.gsf.2018.04.001
- Watson, E., Wark, D., & Thomas, J. (2006). Crystallization thermometers for zircon and rutile. *Contributions to Mineralogy and Petrology*, 151(4), 413-433. doi: 10.1007/s00410-006-0068-5
- White, R. W., Powell, R., & Clarke, G. L. (2002). The interpretation of reaction textures in Fe-rich metapelitic granulites of the Musgrave Block, central Australia: constraints from mineral equilibria calculations in the system K₂O-FeO-MgO-Al₂O₃-SiO₂-H₂O-TiO₂-Fe₂O₃. *Journal of Metamorphic Geology*, 20(1), 41-55. doi: 10.1046/j.0263-4929.2001.00349.x
- White, R. W., Powell, R., & Holland, T. J. B. (2007). Progress relating to calculation of partial melting equilibria for metapelites. *Journal of Metamorphic Geology*, 25(5), 511-527. doi: 10.1111/j.1525-1314.2007.00711.x
- White, R. W., Powell, R., Holland, T. J. B., & Worley, B. A. (2000). The effect of TiO₂ and Fe₂O₃ on metapelitic assemblages at greenschist and amphibolite facies conditions: mineral equilibria calculations in the system K₂O-FeO-MgO-Al₂O₃-SiO₂-H₂O-TiO₂-Fe₂O₃. *Journal of Metamorphic Geology*, 18(5), 497-511. doi: 10.1046/j.1525-1314.2000.00269.x
- Whitehouse, M. J., & Platt, J. P. (2003). Dating high-grade metamorphism - constraints from rare-earth elements in zircon and garnet. *Contributions to Mineralogy and Petrology*, 145(1), 61-74. doi: 10.1007/s00410-002-0432-z
- Whitehouse, M. J., Ravindra Kumar, G. R., & Rim  sa, A. (2014). Behaviour of radiogenic Pb in zircon during ultrahigh-temperature metamorphism: an ion imaging and ion tomography case study from the Kerala Khondalite Belt, southern India. *Contributions to Mineralogy and Petrology*, 168(2), 1042. doi: 10.1007/s00410-014-1042-2
- Whitney, D. L., Roger, F., Teyssier, C., Rey, P. F., & Respaut, J. P. (2015). Syn-collapse eclogite metamorphism and exhumation of deep crust in a migmatite dome: The P-T-t record of the youngest Variscan eclogite (Montagne Noire, French Massif Central). *Earth and Planetary Science Letters*, 430, 224-234. doi: 10.1016/j.epsl.2015.08.026
- Whitney, D. L., Hamelin, C., Teyssier, C., Raia, N. H., Korchinski, M. S., Seaton, N. C. A., ... Rey, P. F. (2020). Deep crustal source of gneiss dome revealed by eclogite in migmatite (Montagne Noire, French Massif Central). *Journal of Metamorphic Geology*, 38(3), 297-327. doi: 10.1111/jmg.12523
- Worley, B., & Powell, R. (2000). High-precision relative thermobarometry: theory and a worked example. *Journal of Metamorphic Geology*, 18(1), 91-101.

- Yakymchuk, C., & Brown, M. (2014). Behaviour of zircon and monazite during crustal melting. *Journal of the Geological Society*, 171, 465-479. doi: 10.1144/jgs2013-115
- Yakymchuk, C., Kirkland, C. L., & Clark, C. (2018). Th/U ratios in metamorphic zircon. *Journal of Metamorphic Geology*, 36(6), 715–737. doi:10.1111/jmg.12307

SUPPORTING INFORMATION

Additional supporting information may be found online in the Supporting Information section at the end of the article.

Figure S1. Eclogite EP1 – scan (unpolarized light), X-ray maps and a BSE image of the analysed thin section.

Figure S2. BSE and CL images of zircon analysed in-context in the thin section of the fresh eclogite EP1.

Figure S3. Th/U ratios plotted against $^{206}\text{Pb}/^{238}\text{U}$ dates in the eclogite samples EP1 (a) and MN12-3 (b).

Figure S4. BSE images of monazite analysed in-context in the thin section of the retrogressed eclogite MN12-03.

Figure S5. Concordia diagrams for the monazite data in the retrogressed eclogite MN12-03.

Figure S6. Zircon (Gd/Lu)_N ratios plotted against $^{206}\text{Pb}/^{238}\text{U}$ dates.

Figure S7. Chemical profiles of selected trace elements and corresponding chondrite-normalized REE spectra in garnet.

Figure S8. Chondrite-normalized REE spectra of amphibole, omphacite and plagioclase.

Figure S9. REE partitioning between garnet and zircon displayed on traditional REE plots and on array plots.

Figure S10. *P–T* pseudosection and isopleths of the anorthite proportion in plagioclase at low pressures for the eclogite EP1.

Figure S11. Ti-in-zircon temperatures from eclogites as a function of $^{206}\text{Pb}/^{238}\text{U}$ dates.

Tables S1-S3. Operating conditions for the LA-ICP-MS equipment (U-Pb dating and trace elements analyses).

Table S4. Representative microprobe analyses.

Table S5. Whole-rock chemical compositions.

MN-Dataset.xlsx

Table S6. U-Pb dating analyses on zircon in the fresh eclogite EP1.

Table S7. REE analyses on zircon in the fresh eclogite EP1.

Table S8. U-Pb dating analyses on zircon in the retrogressed eclogite MN12-03.

Table S9. REE analyses on zircon in the retrogressed eclogite MN12-03.

Table S10. U-Th-Pb dating analyses on monazite in the retrogressed eclogite MN12-03.

Table S11. U-Pb dating analyses on zircon in the embedding migmatite EP5.

Table S12. REE analyses of garnet from the eclogites.

Table S13. REE analyses of omphacite, amphibole and plagioclase from the eclogites.

SUPPORTING INFORMATION

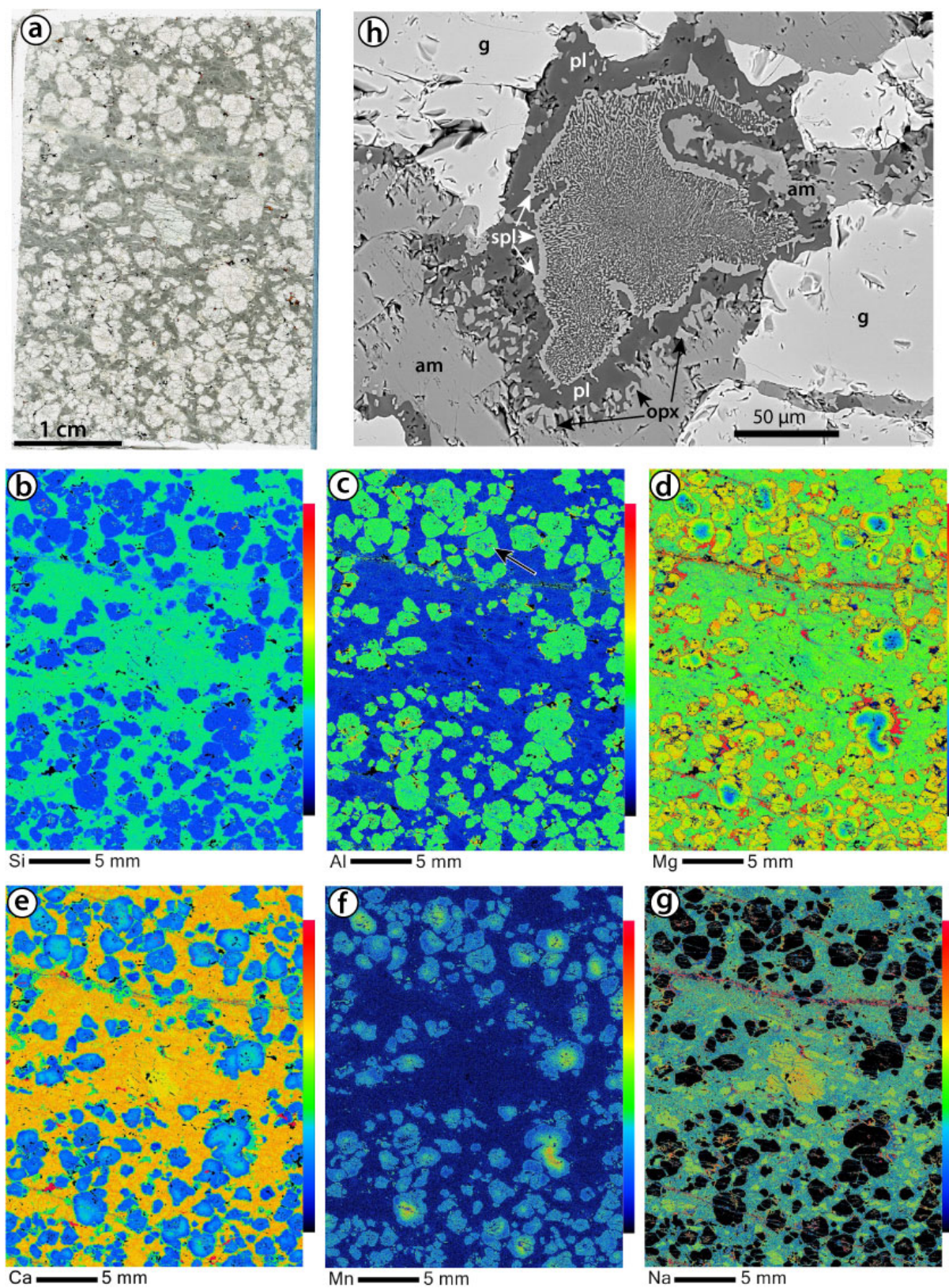


Figure S1. a) Scan (unpolarized light) of the analyzed thin section of sample EP1. Dark green domains correspond to the secondary amphibole + plagioclase-dominated symplectites. b-g) Thin section-scale X-ray

maps. Red spots in the Si map (b) indicate the location of quartz crystals. Red spots in the Al map (c; arrow) correspond to symplectitic pseudomorphs after kyanite. Note the well preserved garnet zoning in Mg, Ca, Mn (d-f). Na-rich patches in (g) correspond to the location of preserved omphacite crystals. h) Back-scattered electron image of the spinel-plagioclase pseudomorph after kyanite (located by an arrow in c), included in garnet. Note also the presence of orthopyroxene at the rim of primary amphibole.

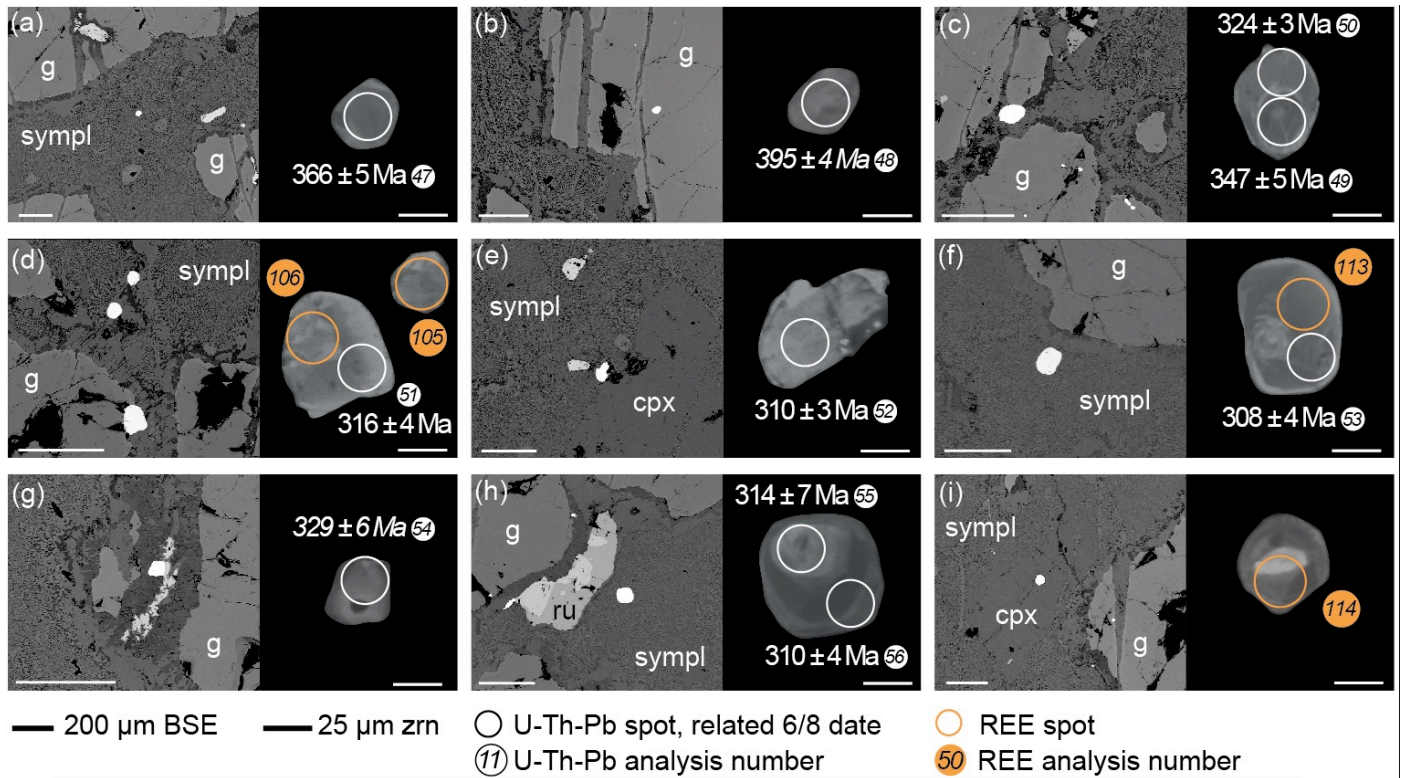


Figure S2. BSE (left) and CL (right) images of zircon analysed in-context in the thin section of the fresh eclogite EP1. BSE images show the location of the zircon crystals (brightest spots) with respect to the other minerals or symplectites. The locations of laser spots (white and orange circles for U-Pb and REE analyses, respectively) are indicated along with the spot number (Tables S6 and S7). The corresponding $^{206}\text{Pb}/^{238}\text{U}$ dates are quoted with $\pm 2\sigma$ uncertainty. All displayed analyses are concordant at $>95\%$ (except those in italic).

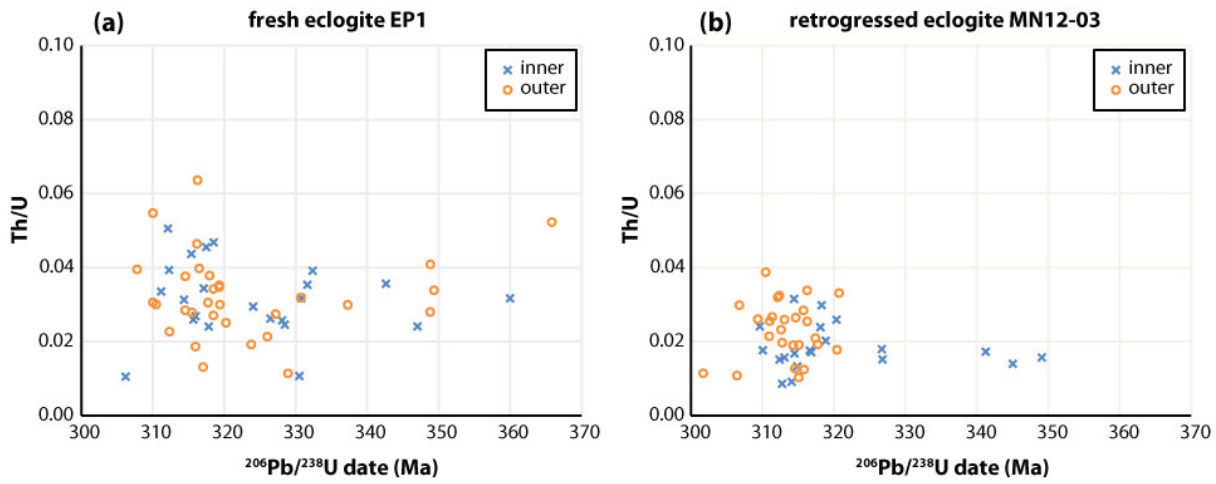


Figure S3. Th/U ratios plotted against $^{206}\text{Pb}/^{238}\text{U}$ dates in the samples EP1 (a) and MN12-3 (b). The data are colour-coded by position of analytical spot in zircon (inner vs. outer domains).

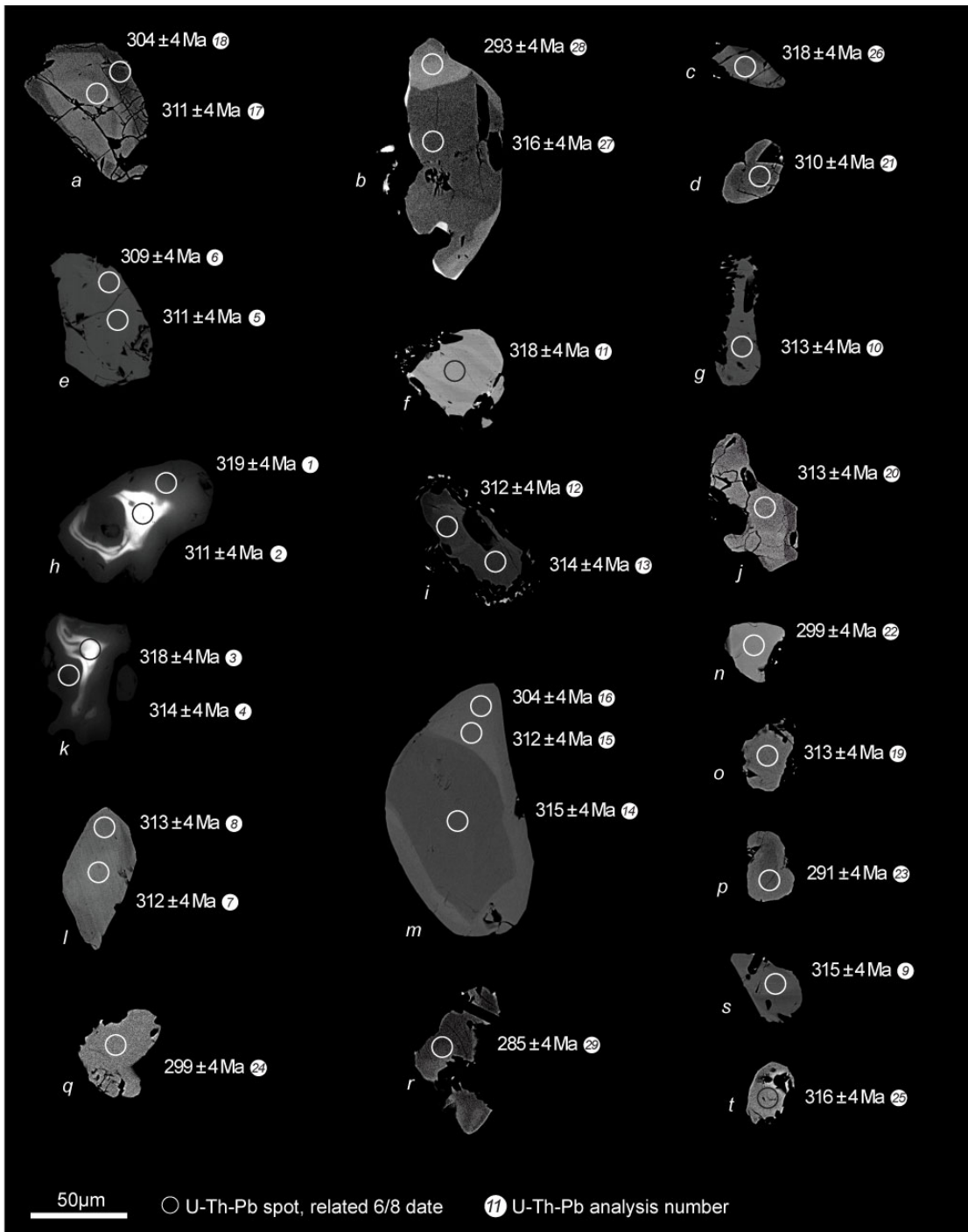


Figure S4. BSE images of monazite analysed in-context in the thin section of the retrogressed eclogite MN12-03. The locations of laser spots for U-Th-Pb analyses is indicated along with the spot number (Table S10). The corresponding $^{206}\text{Pb}/^{238}\text{U}$ dates are quoted with $\pm 2\sigma$ uncertainty.

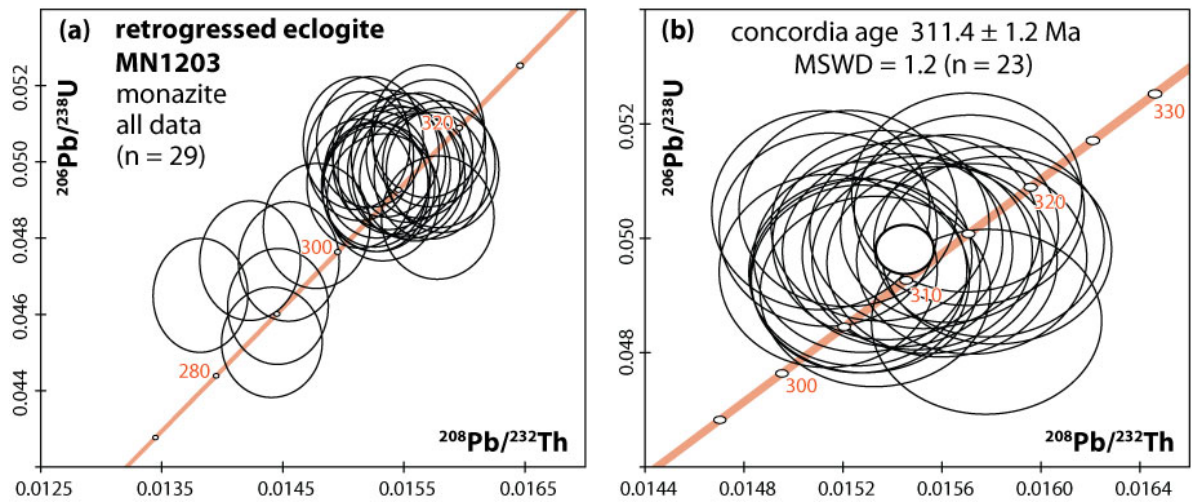


Figure S5. Concordia diagrams for the monazite data in the retrogressed eclogite MN12-03. (a) overview of all data, (b) close-up on the major cluster of concordant data.

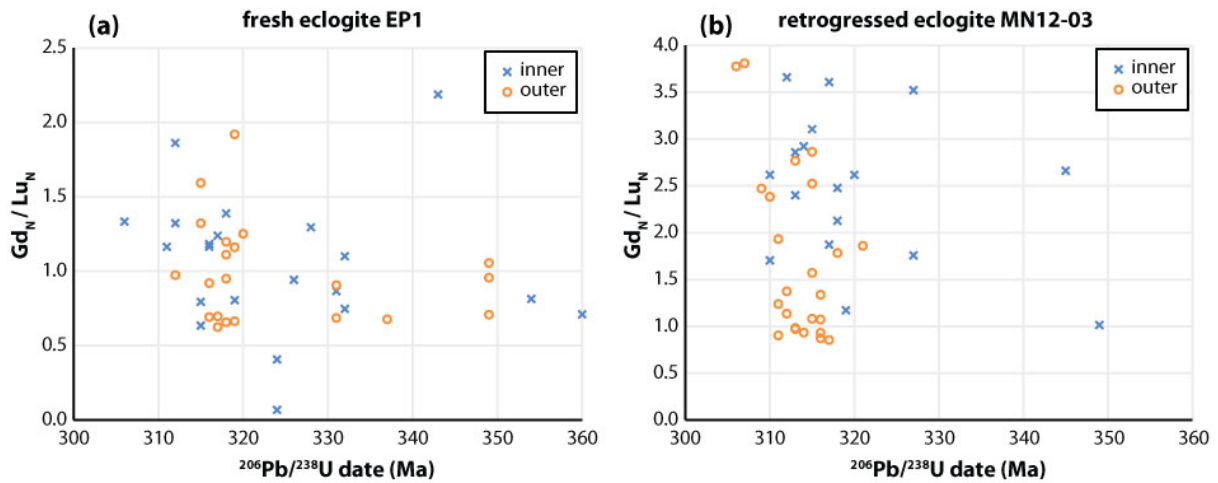


Figure S6. $(Gd/Lu)_N$ ratios plotted against $^{206}Pb/^{238}U$ dates in the fresh eclogite EP1 (a) and the retrogressed eclogite MN12-03 (b); the data are colour-coded by position (inner / outer domain) of analytical spot in zircon.

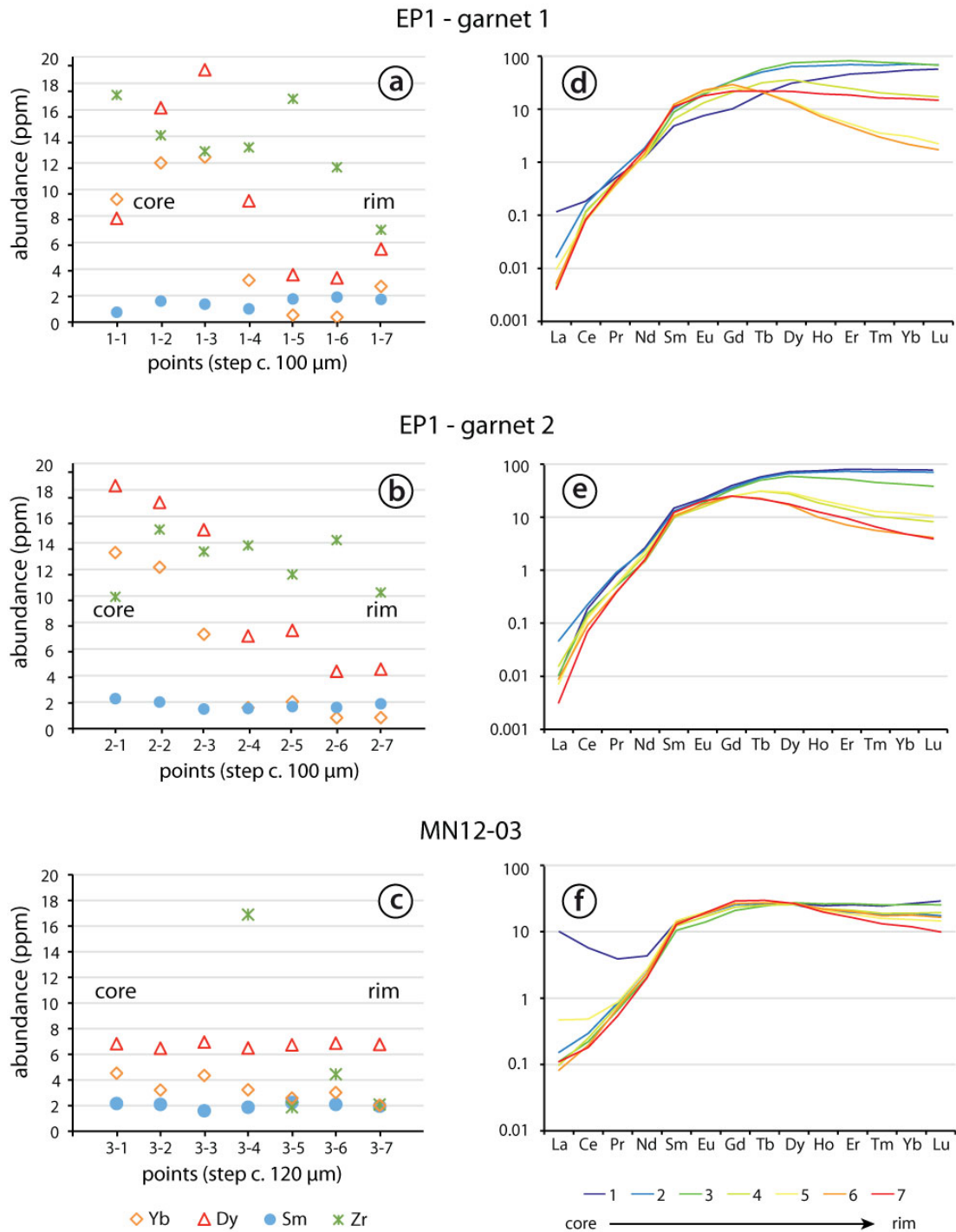


Figure S7. Chemical profiles of selected trace elements (a-c) and corresponding chondrite-normalized REE spectra (d-f) of two garnet crystals from EP1 and one from sample MN12-03. Data and location of analytical spots in Table S12. The profile in a) corresponds to the left half of the profile from Fig. 2 (see also Figure S21), the profile in c) to the upper half of the profile from Fig. 3. Zirconium contents of analyses 1, 2 and 3 in c) (1110, 26 and 58 ppm respectively) are not represented. “Core” and “rim” are inferred qualitatively from the the major element zoning (Fig. 2). Chondrite values of McDonough and Sun (1995).

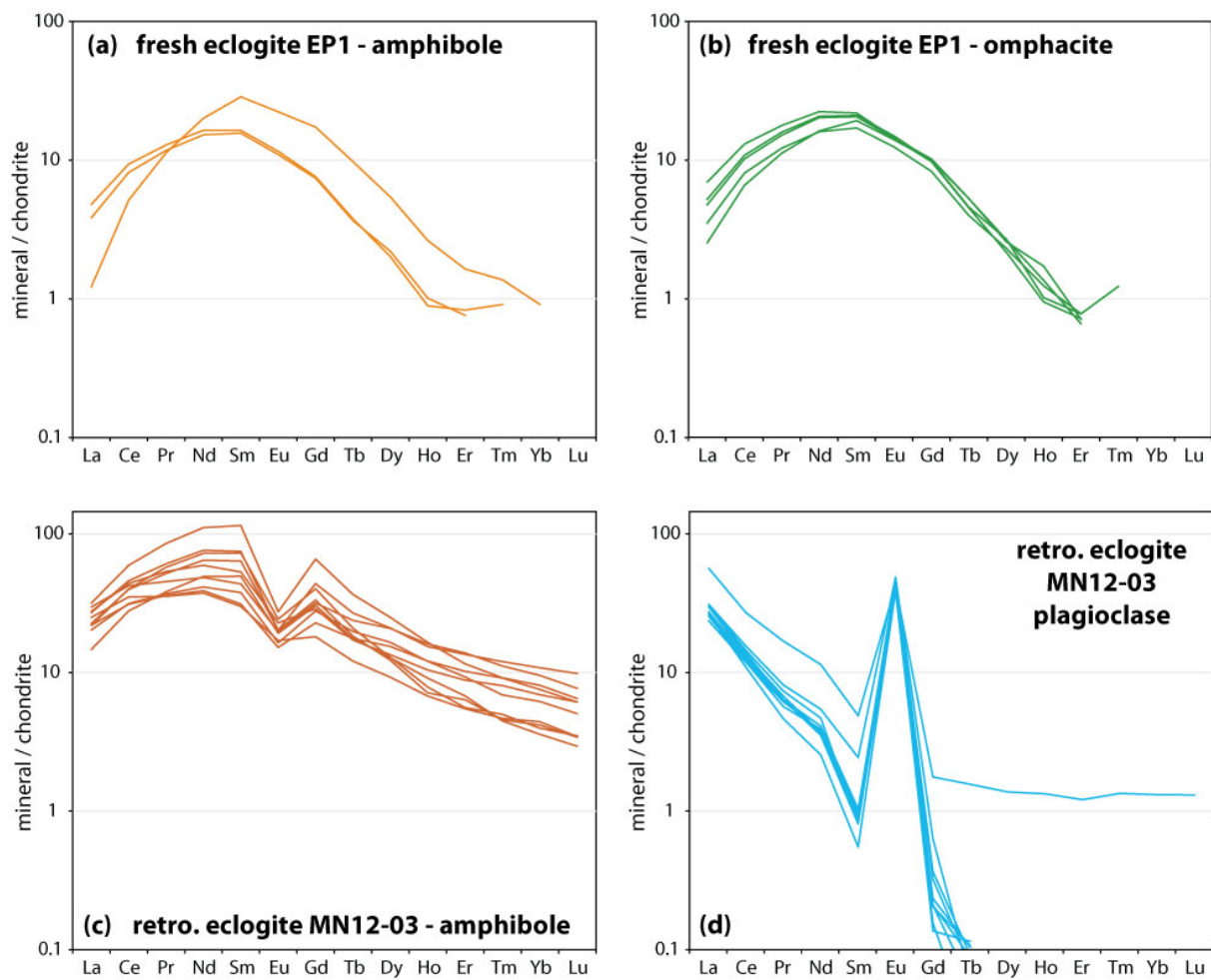


Figure S8. Chondrite-normalized REE spectra of amphibole (a) and omphacite (b) from EP1 and amphibole (c) and plagioclase (d) from MN12-03. Chondrite values of McDonough and Sun (1995).

fresh eclogite EP1

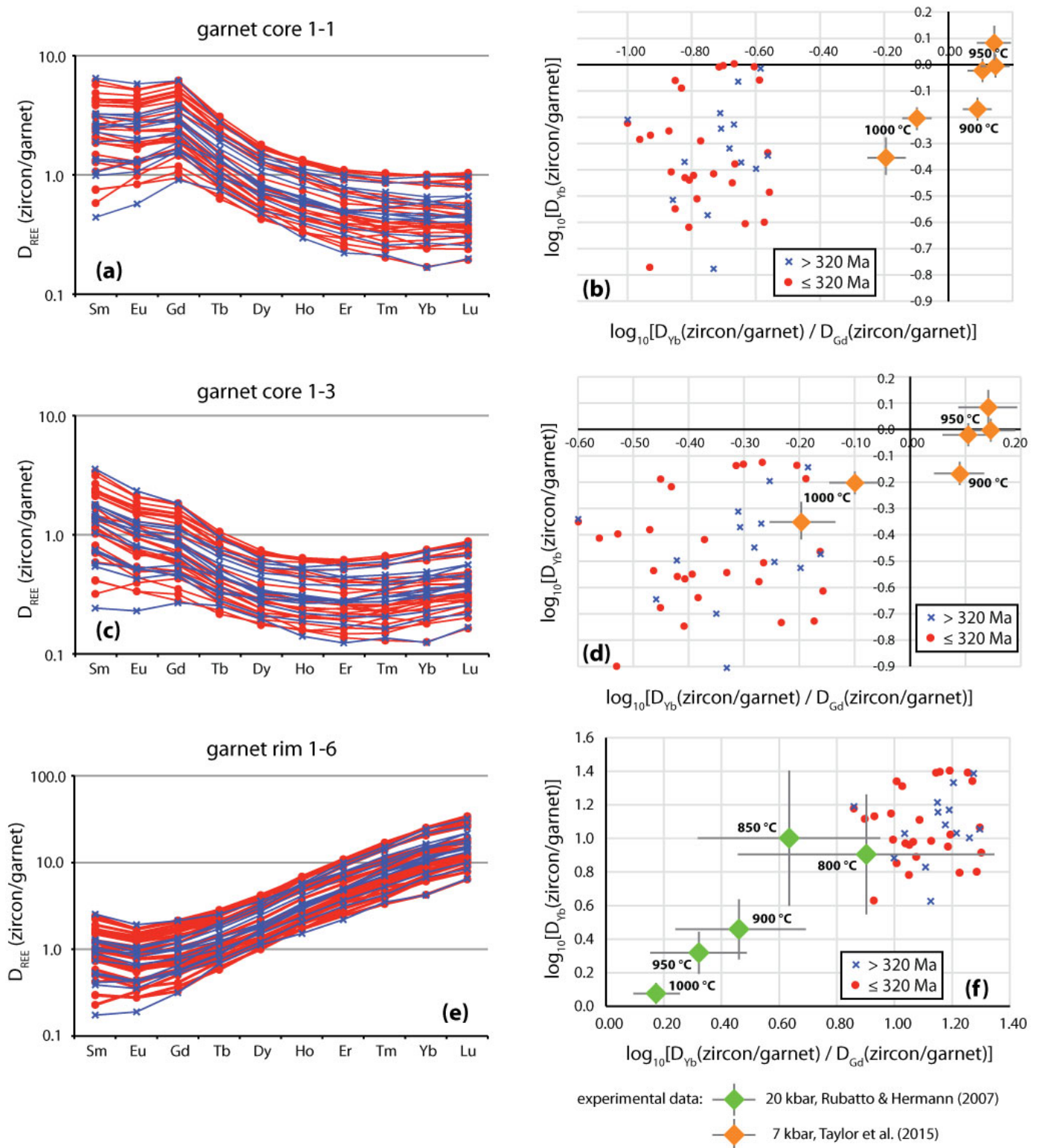


Figure S9. REE partitioning between garnet and zircon, $D_{\text{REE}}(\text{zircon/garnet})$, displayed on a traditional REE plot (a, c, e) and on an array plot together with the experimental data (as of Taylor et al., 2017) (b, d, f) for the eclogite EP1. The garnet composition (Table S10) is that of the garnet core (a-b: analysis 1-1, c-d: analysis 1-3) and rim (c-d: analysis 1-6).

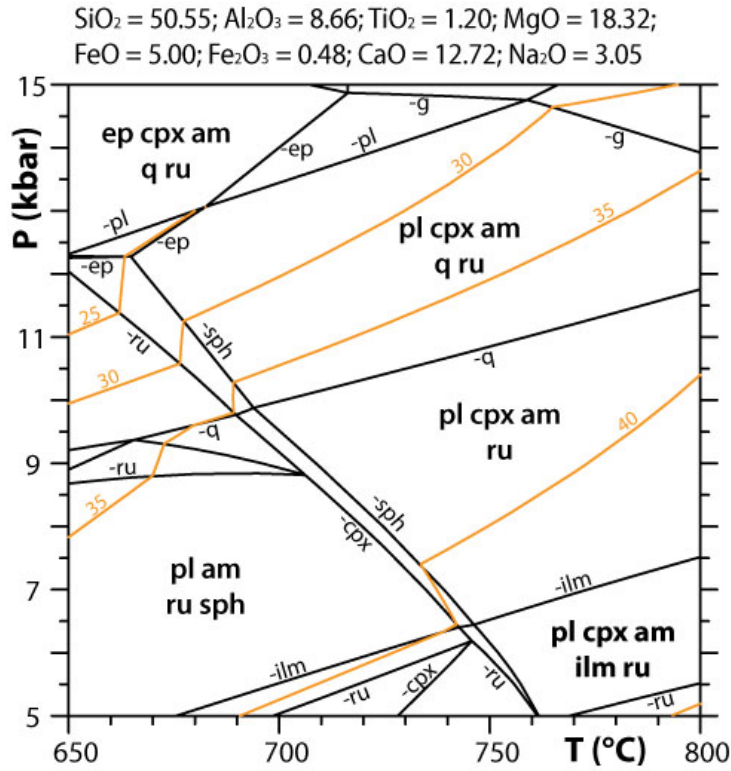


Figure S10. P – T pseudosection and isopleths of the anorthite proportion in plagioclase (orange lines) for the fresh eclogite EP1, calculated for the composition that results from the removal of the garnet cores from the analysed composition (as in Fig. 12b). H₂O is in excess. Only main fields are labelled.

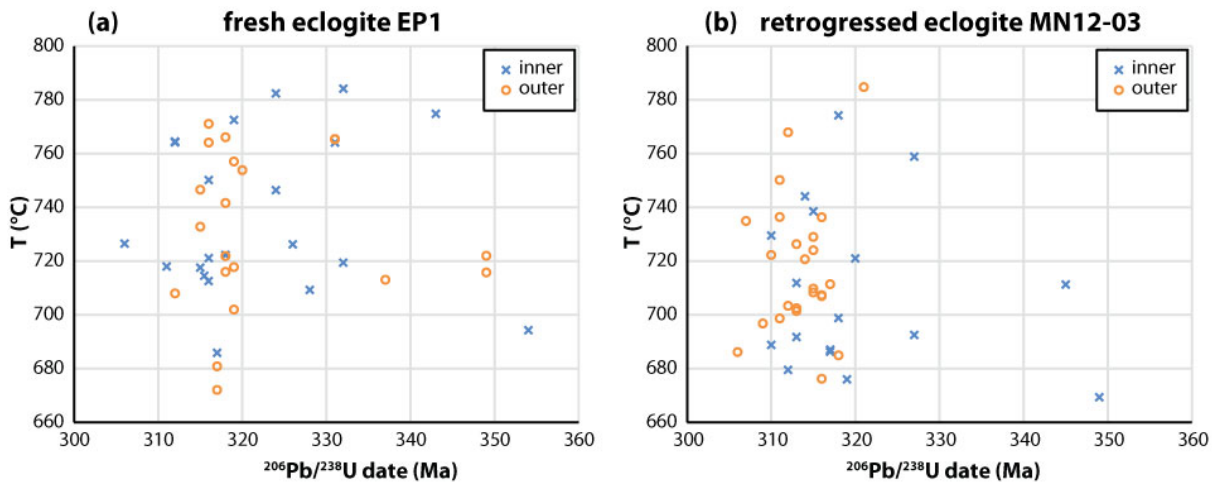


Figure S11. Ti-in-zircon (Watson et al., 2006) temperatures as a function of the ²⁰⁶Pb/²³⁸U date of the corresponding domain, and the position of the analysis (inner or outer zircon zone) for the samples EP1 (a) and MN12-03 (b).

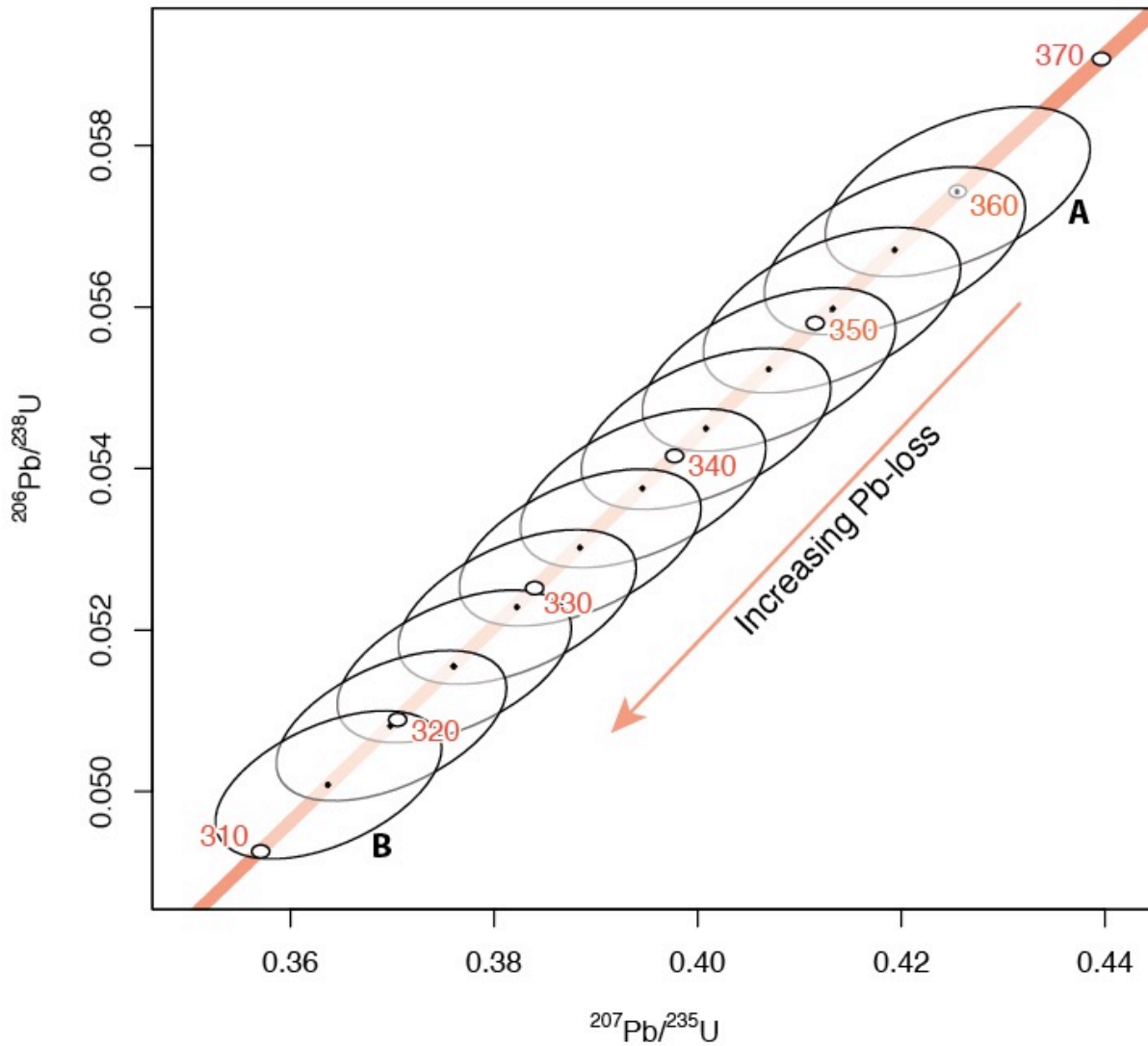


Figure S12. Theoretical position of zircon analyses considering grains that crystallized 360 Ma ago and consecutively underwent Pb-loss due to a HT-LP metamorphic event 315 Ma ago. Ellipse A corresponds to a 0% Pb-loss, ellipse B to a 100% (full-reset) Pb-loss. Every other ellipse was generated with a 10% Pb-loss increment. Errors are 2.5% for the $^{207}\text{Pb}/^{235}\text{U}$ ratios and 1.5% for the $^{206}\text{Pb}/^{238}\text{U}$ ratios. The Rho value was set at 0.5. Black dots correspond the centres of the ellipses.

TABLES

Table S1. Operating conditions for the LA-ICP-MS equipment (U-Pb dating)

Laboratory & Sample Preparation	
Laboratory name	GeOHeLiS Analytical Platform, Géosciences Rennes/OSUR, Univ. Rennes
Sample type/mineral	Zircon (Zrn) and Monazite (Mnz)
Sample preparation	Conventional mineral separation, 1-inch resin mount, 1 μm polish to finish and thin sections
Imaging	CL: RELION CL instrument, Olympus Microscope BX51WI, Leica Color Camera DFC 420C
Laser ablation system	
Make, Model & type	ESI NWR193UC, Excimer
Ablation cell	ESI NWR TwoVol2
Laser wavelength	193 nm
Pulse width	< 5 ns
Fluence	6.7 J/cm ² (Mnz) or 8 J/cm ² (Zrn)
Repetition rate	3 Hz
Spot size	10 μm (Mnz) or 25-30 μm (Zrn)
Sampling mode / pattern	Single spot
Carrier gas	100% He, Ar make-up gas and N ₂ (3 ml/mn) combined using in-house smoothing device
Background collection	20 seconds
Ablation duration	60 seconds
Wash-out delay	15 seconds
Cell carrier gas flow (He)	0.75 l/min
ICP-MS Instrument	
Make, Model & type	Agilent 7700x, Q-ICP-MS
Sample introduction	Via conventional tubing
RF power	1350 W
Sampler, skimmer cones	Ni
Extraction lenses	X type
Make-up gas flow (Ar)	0.85 l/min
Detection system	Single collector secondary electron multiplier
Data acquisition protocol	Time-resolved analysis
Scanning mode	Peak hopping, one point per peak
Detector mode	Pulse counting, dead time correction applied, and analog mode when signal intensity > ~ 10 ⁶ cps
Masses measured	²⁰⁴ (Hg + Pb), ²⁰⁶ Pb, ²⁰⁷ Pb, ²⁰⁸ Pb, ²³² Th, ²³⁸ U
Integration time per peak	10-30 ms
Sensitivity / Efficiency	28000 cps/ppm Pb (50 μm , 10 Hz)

Data Processing	
Gas blank	20 seconds on-peak
Calibration strategy	GJ1 zircon and Moacir monazite standards used as primary reference materials, Plešovice zircon and Managoutry monazite used as secondary reference materials (quality control)
Reference Material info	GJ1 (Jackson et al., 2004) Moacir (Gasquet et al., 2010) Plešovice (Sláma et al., 2008) Manangoutry (Paquette and Tiepolo, 2007)
Data processing package used	Iolite (Paton et al., 2010; 2011)
Mass discrimination	Standard-sample bracketing with $^{207}\text{Pb}/^{206}\text{Pb}$ and $^{206}\text{Pb}/^{238}\text{U}$ ($^{208}\text{Pb}/^{232}\text{Th}$ for Mnz) normalized to reference material GJ1 and Moacir
Common Pb correction	No common Pb correction
Uncertainty level and propagation	Ages are quoted at 2 sigma absolute, propagation is by quadratic addition according to Horstwood et al. (2003). Reproducibility and age uncertainty of reference material are propagated.
Quality control / Validation	Plešovice: 338.1 ± 1.9 Ma (N=18; MSWD=1.00) Manangoutry : 558.7 ± 4.1 Ma (N=6, MSWD=0.65)

Table S2. Operating conditions for the LA-ICP-MS equipment (Trace elements analyses, Magma et Volcans laboratory, Université Clermont-Ferrand, France)

Laboratory & Sample Preparation	
Laboratory name	Laboratoire Magmas & Volcans, Clermont-Ferrand, France
Sample type/mineral	Zircon, amphibole, clinopyroxene
Sample preparation	Conventional mineral separation, 1 inch resin mount, 1 μm polish to finish and thin sections
Imaging	CL, Jeol JSM-5910 LV, 15 kV, 19 mm working distance
Laser ablation system	
Make, Model & type	Resonetics/M-50E 193nm, Excimer
Ablation cell & volume	Laurin Cell ® two volumes cell, Laurin Technic Ltd., volume ca. 1-2 cm^3
Laser wavelength	193 nm
Pulse width	< 4 ns
Fluence	4 J/cm^2 (zircon), 6 J/cm^2 (amphibole, pyroxene)
Repetition rate	3 Hz (zircon), 5 Hz (amphibole, pyroxene)
Spot size	27 μm (zircon), 47 μm (amphibole, pyroxene)
Sampling mode / pattern	Single spot
Carrier gas	100% He, Ar make-up gas and N_2 combined using the Squid® device from RESOLUTION Instruments.
Background collection	30 secs
Ablation duration	60 secs
Wash-out delay	30 secs
Cell carrier gas flow	0.75 l/min
ICP-MS Instrument	
Make, Model & type	Agilent 7500cs, Q-ICP-MS
Sample introduction	Via conventional tubing
RF power	1350 W
Make-up gas flow	0.87 l/min Ar
Detection system	Single collector secondary electron multiplier
Masses measured	^{29}Si (Zrn), ^{44}Ca (Amp, Cpx), ^{49}Ti , ^{89}Y , ^{90}Zr , ^{93}Nb , ^{139}La , ^{140}Ce , ^{141}Pr , ^{146}Nd , ^{147}Sm , ^{153}Eu , ^{157}Gd , ^{159}Tb , ^{163}Dy , ^{165}Ho , ^{166}Er , ^{169}Tm , ^{172}Yb , ^{175}Lu , ^{178}Hf , ^{181}Ta , ^{208}Pb , ^{232}Th , ^{238}U .
Integration time per peak	10 ms
Total integration time per reading	130 ms
Sensitivity / Efficiency	20000 cps/ppm Pb (44 μm , 10 Hz)
Dead time	35 ns
Data Processing	
Gas blank	30 second on-peak
Calibration strategy	Zrn: NIST 612 as external standard and ^{29}Si as internal standard (Si concentration used is 33.6061 wt%). ^{29}Si in unknowns was considered at 14.76 wt%. Amp and Cpx: NIST 612 as external standard and ^{44}Ca as internal standard. (Ca concentration used is 8.5002 wt%) ^{44}Ca values for unknowns are from microprobe measurements
Reference Material info	NIST 612 (GeoRem Database)
Data processing package used / Correction for LIEF	GLITTER ® (van Achterbergh et al., 2001)

Table S3. Operating conditions for the LA-ICP-MS equipment (Trace elements analyses, Géosciences Rennes)

Laboratory & Sample Preparation	
Laboratory name	GeOHeLiS Analytical Platform, Géosciences Rennes/OSUR, Univ. Rennes
Sample type/mineral	Garnet, amphibole, plagioclase, pyroxene
Sample preparation	Thin sections
Laser ablation system	
Make, Model & type	ESI NWR193UC, Excimer
Ablation cell	ESI NWR TwoVol2
Laser wavelength	193 nm
Pulse width	< 5 ns
Fluence	6 J/cm ²
Repetition rate	5 Hz
Spot size	50 µm (garnet); 25 µm (amphibole, pyroxene, plagioclase)
Sampling mode / pattern	Single spot
Carrier gas	100% He, Ar make-up gas and N ₂ (3 ml/mn) combined using in-house smoothing device
Background collection	15 seconds
Ablation duration	45 seconds
Wash-out delay	15 seconds
Cell carrier gas flow (He)	0.75 l/min
ICP-MS Instrument	
Make, Model & type	Agilent 7700x, Q-ICP-MS
Sample introduction	Via conventional tubing
RF power	1350 W
Sampler, skimmer cones	Ni
Extraction lenses	X type
Make-up gas flow (Ar)	0.85 l/min
Detection system	Single collector secondary electron multiplier
Data acquisition protocol	Time-resolved analysis
Scanning mode	Peak hopping, one point per peak
Detector mode	Pulse counting, dead time correction applied, and analog mode when signal intensity > ~ 10 ⁶ cps
Masses measured	²⁷ Al, ⁴³ Ca, ⁸⁹ Y, ⁹⁰ Zr, ¹³⁹ La, ¹⁴⁰ Ce, ¹⁴¹ Pr, ¹⁴⁶ Nd, ¹⁴⁷ Sm, ¹⁵³ Eu, ¹⁵⁷ Gd, ¹⁵⁹ Tb, ¹⁶³ Dy, ¹⁶⁵ Ho, ¹⁶⁶ Er, ¹⁶⁹ Tm, ¹⁷² Yb, ¹⁷⁵ Lu
Integration time per peak	30 ms
Data Processing	
Calibration strategy	NIST 612 as external standard and ²⁷ Al as internal standard (Al concentration used is 1.1167 wt%). ²⁷ Al values of unknowns are from microprobe measurements
Reference Material info	GeoRem database
Data processing package used	IOLITE software using “Trace_elements_IS” data reduction scheme (Paton et al., 2011)

Table S4. Representative microprobe analyses. The amount of ferric iron was calculated from stoichiometric constraints using the Tim Holland's programme AX (<https://filedn.com/IU1GlyFhv3UuXg5E9dbnWFF/TJBHpages/ax.html>). For amphibole, the Fe³⁺ content corresponds to the average from minimum and maximum constraints (Holland & Blundy, 1994). c – core, r – rim, mx – matrix, incl – inclusion, sympl – symplectite.

Sample Min anal. # position	g map53 c	g map04 r	cpx 2802	cpx 2805	EP1 am 301 incl g	am 3503 sympl	pl 1007 sympl	pl 3509 sympl	ilm 3005 mx
SiO2	38.95	40.82	55.69	55.40	44.59	42.92	64.66	53.56	0.04
TiO2	0.10	0.10	0.16	0.18	0.39	0.63	0.04	0.00	57.19
Al2O3	22.29	22.95	10.84	9.66	13.82	18.66	22.33	29.64	0.02
Cr2O3	0.00	0.00	0.00	0.00	0.00	0.00	0.00	0.00	0.00
Fe2O3	1.11	1.10	0.00	0.00	5.05	0.12	0.25	0.25	0.00
FeO	20.00	16.78	2.89	2.30	4.65	3.80	0.00	0.00	33.03
MnO	0.75	0.28	0.00	0.01	0.06	0.00	0.01	0.00	0.33
MgO	8.38	14.39	9.79	11.13	17.15	15.60	0.14	0.01	9.86
CaO	8.54	4.82	14.62	16.11	8.64	11.64	3.18	11.90	0.00
Na2O	0.00	0.00	5.55	4.84	3.38	3.82	9.75	4.72	0.00
K2O	0.00	0.01	0.00	0.00	0.36	0.07	0.03	0.01	0.00
Total	100.12	101.25	99.54	99.63	98.08	97.26	100.39	100.09	100.47
Oxygens	12	12	6	6	23	23	8	8	3
Si	2.963	2.978	1.979	1.971	6.324	6.073	2.838	2.418	0.001
Ti	0.005	0.006	0.004	0.005	0.041	0.067	0.001	0.000	1.002
Al	2.000	1.974	0.454	0.405	2.311	3.112	1.156	1.578	0.001
Cr	0.000	0.000	0.000	0.000	0.000	0.000	0.000	0.000	0.000
Fe3	0.063	0.060	0.000	0.000	0.539	0.012	0.008	0.009	0.000
Fe2	1.273	1.024	0.086	0.068	0.552	0.450	0.000	0.000	0.644
Mn	0.048	0.017	0.000	0.000	0.007	0.000	0.000	0.000	0.007
Mg	0.951	1.564	0.518	0.590	3.625	3.289	0.009	0.001	0.342
Ca	0.696	0.377	0.557	0.614	1.312	1.764	0.149	0.576	0.000
Na	0.000	0.000	0.382	0.334	0.929	1.048	0.830	0.413	0.000
K	0.000	0.001	0.000	0.000	0.066	0.013	0.002	0.000	0.000
Sum	8.000	8.000	3.981	3.989	15.893	15.832	4.994	4.995	1.997
XMg / An	0.43	0.60	0.86	0.90	0.87	0.88	0.15	0.58	0.35
XNa			0.41	0.35			0.85	0.42	
Alm	0.43	0.34							
Prp	0.32	0.52							
Grs	0.23	0.13							
Sps	0.02	0.01							

Table S4. (continued)

Sample Min anal. # position	MN12-03									EP5					
	g p26	g p49	am 912	am 113	am 302	am 303	pl 405	pl 408	bi 308	g P0116	g P0125	bi 708	kfs 706	pl 705	pl 709
	c	r	incl g	mx	sympl	sympl	c	r	mx	c	r			r	c
SiO2	39.67	38.43	43.30	46.90	50.96	54.03	59.81	48.07	36.98	36.64	36.73	34.41	65.06	64.69	63.04
TiO2	0.05	0.07	0.37	0.85	0.56	0.08	0.00	0.00	3.67	0.02	0.04	2.44	0.00	0.03	0.01
Al2O3	22.54	21.68	18.02	10.28	5.16	0.56	25.09	32.81	15.41	20.75	21.25	20.12	18.44	22.11	22.88
Cr2O3	0.00	0.00	0.00	0.00	0.00	0.00	0.00	0.00	0.00	0.00	0.00	0.00	0.00	0.00	0.00
Fe2O3	0.75	0.71	4.51	3.85	2.00	0.00	0.16	0.27	0.00	1.48	0.58	0.00	0.00	0.01	0.00
FeO	22.46	26.56	6.57	9.37	9.91	20.94	0.00	0.00	14.95	34.47	31.17	23.17	0.00	0.00	0.00
MnO	1.71	3.68	0.16	0.42	0.42	1.10	0.00	0.06	0.10	4.21	9.25	0.33	0.00	0.00	0.00
MgO	9.88	5.33	13.11	13.78	15.36	17.81	0.00	0.02	14.22	2.29	1.33	5.46	0.01	0.03	0.00
CaO	4.43	4.86	10.28	11.38	11.21	1.19	7.19	16.85	0.05	0.77	0.76	0.04	0.00	2.68	3.87
Na2O	0.00	0.00	2.72	1.39	0.69	0.06	7.66	2.22	0.38	0.00	0.00	0.16	1.74	9.77	8.91
K2O	0.00	0.00	0.29	0.31	0.18	0.00	0.09	0.04	8.62	0.01	0.03	9.64	15.07	0.34	0.28
Total	101.50	101.30	99.33	98.51	96.45	95.77	99.99	100.34	94.39	100.63	101.13	95.78	100.31	99.67	98.99
Oxygens	12	12	23	23	23	23	8	8	11	12	12	11	8	8	8
Si	2.978	2.983	6.105	6.740	7.396	7.992	2.668	2.200	2.778	2.965	2.969	2.661	2.991	2.857	2.809
Ti	0.003	0.004	0.039	0.092	0.061	0.009	0.000	0.000	0.207	0.001	0.003	0.142	0.000	0.001	0.000
Al	1.995	1.984	2.995	1.741	0.883	0.098	1.319	1.770	1.365	1.980	2.024	1.835	0.999	1.151	1.202
Cr	0.000	0.000	0.000	0.000	0.000	0.000	0.000	0.000	0.000	0.000	0.000	0.000	0.000	0.000	0.000
Fe3	0.042	0.041	0.478	0.416	0.219	0.000	0.005	0.009	0.000	0.090	0.035	0.000	0.000	0.000	0.000
Fe2	1.410	1.725	0.775	1.126	1.203	2.590	0.000	0.000	0.939	2.332	2.107	1.499	0.000	0.000	0.000
Mn	0.109	0.242	0.019	0.051	0.052	0.137	0.000	0.002	0.007	0.288	0.633	0.022	0.000	0.000	0.000
Mg	1.105	0.616	2.755	2.951	3.322	3.927	0.000	0.001	1.592	0.276	0.160	0.630	0.000	0.002	0.000
Ca	0.356	0.404	1.553	1.752	1.742	0.189	0.343	0.827	0.004	0.067	0.066	0.003	0.000	0.127	0.185
Na	0.000	0.000	0.743	0.386	0.194	0.017	0.662	0.197	0.056	0.001	0.000	0.024	0.155	0.837	0.770
K	0.000	0.000	0.053	0.057	0.034	0.000	0.005	0.002	0.826	0.001	0.003	0.951	0.884	0.019	0.016
Sum	8.000	8.000	15.679	15.451	15.178	14.959	5.003	5.009	7.774	8.000	8.000	7.768	5.030	4.995	4.983
XMg / An	0.44	0.26	0.78	0.72	0.73	0.60	0.34	0.81	0.63	0.11	0.07	0.30		0.13	0.19
XNa							0.66	0.19					0.15	0.85	0.79
Alm	0.47	0.58								0.79	0.71				
Prp	0.37	0.21								0.09	0.05				
Grs	0.12	0.14								0.02	0.02				
Sps	0.04	0.08								0.10	0.21				

Table S5. Whole-rock chemical composition of eclogite samples from the Terme de Fourcaric locality, Montagne Noire (major – wt.% and trace elements – ppm). Fe₂O₃(tot) - total Fe; FeO* - determined by wet titration; ‘-’ = Not determined; bdl = below detection limit.

Sample	EP1	EP4	MN12-03
SiO ₂	47.10	46.37	44.80
Al ₂ O ₃	15.85	16.24	16.15
Fe ₂ O ₃ (tot)	10.50	11.20	16.20
FeO*	8.40	9.26	13.42
MnO	0.16	0.17	0.64
MgO	11.49	11.24	8.87
CaO	11.05	10.57	9.09
Na ₂ O	2.45	1.83	1.25
K ₂ O	bdl	0.11	0.30
TiO ₂	1.25	1.38	1.70
P ₂ O ₅	0.18	0.18	0.48
LOI	0.00	0.32	0.68
Total	100.02	99.61	100.14

Sample	EP1	EP4	MN12-03
Rb	0.6	5.3	12.3
Cs	0.2	1.4	3.4
Ba	bdl	15.7	90.9
Be	1.0	0.9	1.3
Sr	107.2	109.2	224.2
Th	0.5	0.7	1.2
U	0.3	0.3	0.7
Zr	113.5	117.9	136.7
Hf	2.9	3.1	3.4
Nb	5.9	7.2	47.8
Ta	0.5	0.6	3.9
Sc	33.9	36.8	–
Cr	715.4	699.6	659.1
Ni	303.3	243.3	298.8
Co	48.8	47.8	56.9
V	181.3	188.6	265.7
Mo	0.7	0.6	0.8
W	2.5	2.2	3.1
Ge	1.5	1.5	1.9
Sn	1.6	1.9	3.6
Pb	1.2	1.2	3.3
Ga	15.4	15.2	18.0
In	0.1	0.1	0.1
Zn	81.4	84.2	132.8
Cu	68.9	71.6	71.7
As	3.8	4.8	21.8
Sb	0.1	0.1	0.2
Bi	bdl	bdl	0.1
Cd	0.1	0.1	0.2
Y	24.2	27.5	30.2
La	7.3	7.7	19.7
Ce	18.4	18.9	44.8
Pr	2.6	2.6	5.9
Nd	12.3	12.1	25.5
Sm	3.5	3.5	6.4
Eu	1.2	1.2	1.9
Gd	3.9	4.3	6.4
Tb	0.7	0.8	1.0
Dy	4.3	5.0	5.8
Ho	0.9	1.1	1.1
Er	2.5	2.9	2.7
Tm	0.4	0.4	0.3
Yb	2.4	2.7	2.2
Lu	0.4	0.4	0.3
∑REE	60.7	63.5	124.2
LaN/LuN	2.18	2.01	6.56
Eu/Eu*	0.98	0.96	0.93

Table S6. U-Pb dating analyses on zircon in the fresh eclogite EP1.

Table S7. REE analyses on zircon in the fresh eclogite EP1.

Table S8. U-Pb dating analyses on zircon in the retrogressed eclogite MN12-03.

Table S9. REE analyses on zircon in the retrogressed eclogite MN12-03.

Table S10. U-Th-Pb dating analyses on monazite in the retrogressed eclogite MN12-03.

Table S11. U-Pb dating analyses on zircon in the embedding migmatite EP5.

Table S12. REE analyses of garnet from the eclogites.

Table S13. REE analyses of omphacite, amphibole and plagioclase from the eclogites.

References

- Gasquet, D., Bertrand, J.M., Paquette, J.L., Lehmann, J., Ratzov, G., De Ascenção Guedes, R., ... Nomade, S. (2010). Miocene to Messinian deformation and hydrothermal activity in a pre-Alpine basement massif of the French western Alps: new U-Th-Pb and argon ages from the Lauzière massif. *Bulletin de la Société Géologique de France*, 181(3), 227-241.
- Holland, T. J. B., & Blundy, J. D. (1994). Non-ideal interactions in calcic amphiboles and their bearing on amphibole-plagioclase thermometry. *Contributions to Mineralogy and Petrology*, 116, 433-447.
- Horstwood, M. S. A., Foster, G. L., Parrish, R. R., Noble, S. R., & Nowell, G. M. (2003). Common-Pb corrected in situ U-Pb accessory mineral geochronology by LA-MC-ICP-MS. *Journal of Analytical Atomic Spectrometry*, 18(8), 837-846. doi: 10.1039/B304365G
- Jackson, S.E., Pearson, N.J., Griffin, W.L. & Belousova, E.A. (2004). The application of laser ablation-inductively coupled plasma-mass spectrometry to in situ U-Pb zircon geochronology. *Chemical Geology*, 211(1-2), 47-69.
- McDonough, W. F., & Sun, S. S. (1995). The composition of the Earth. *Chemical Geology*, 120(3), 223-253. doi: 10.1016/0009-2541(94)00140-4
- Paquette, J.L. and Tiepolo, M. (2007). High resolution (5 µm) U-Th-Pb isotope dating of monazite with excimer laser ablation (ELA)-ICPMS. *Chemical Geology*, 240(3-4), 222-237.
- Paton, C., Hellstrom, J., Paul, B., Woodhead, J., & Hergt, J. (2011). Iolite: Freeware for the visualisation and processing of mass spectrometric data. *Journal of Analytical Atomic Spectrometry*, 26, 2508, doi: 10.1039/c1ja10172b.
- Rubatto, D., & Hermann, J. (2007). Experimental zircon/melt and zircon/garnet trace element partitioning and implications for the geochronology of crustal rocks. *Chemical Geology*, 241(1-2), 38-61.
- Sláma, J., Košler, J., Condon, D.J., Crowley, J.L., Gerdes, A., Hanchar, J.M., ... Schaltegger, U. (2008). Plešovice zircon—a new natural reference material for U-Pb and Hf isotopic microanalysis. *Chemical Geology*, 249(1-2), 1-35.
- Taylor, R. J. M., Harley, S. L., Hinton, R. W., Elphick, S., Clark, C., & Kelly, N. M. (2015). Experimental determination of REE partition coefficients between zircon, garnet and melt: a key to understanding high-T crustal processes. *Journal of Metamorphic Geology*, 33(3), 231-248. doi: 10.1111/jmg.12118
- Taylor, R. J. M., Clark, C., Harley, S. L., Kylander-Clark, A. R. C., Hacker, B. R., & Kinny, P. D. (2017). Interpreting granulite facies events through rare earth element partitioning arrays. *Journal of Metamorphic Geology*, 35(7), 759-775. doi: 10.1111/jmg.12254
- van Achterbergh, E., Ryan, C. G., Jackson, S. E., & Griffin, W. L. (2001). Data reduction software for LA-ICP-MS: appendix. In P. J. Sylvester (Ed.), *Laser Ablation - ICP - mass spectrometry in the earth sciences: principles and applications*, Mineralogical Association of Canada (MAC) Short Course Series, pp. 239–243. Ottawa.
- Watson, E., Wark, D., & Thomas, J. (2006). Crystallization thermometers for zircon and rutile. *Contributions to Mineralogy and Petrology*, 151(4), 413-433.